**Investigation of Signal Shape Effects on the Gas Film in Spark-Assisted Chemical Engraving**

by

Marwan S Eldiasty

A Thesis submitted to the School of Graduate and Postdoctoral Studies in partial fulfillment of the requirements for the degree of

Master of Science in Mechanical Engineering

Department of Mechanical and Manufacturing Engineering
Faculty of Engineering and Applied Sciences
Ontario Tech University

# Thesis Examination Information

Submitted by: **Marwan S. Eldiasty**

**Master of Applied Science in Mechanical Engineering**

Thesis title:

**Investigation of Signal Shape Effects on the Gas Film in Spark-Assisted Chemical Engraving**

An oral defense of this thesis took place on December 5th, 2023 in front of the following examining committee:

**Examining Committee**

| | |
|---|---|
| Chair of Examining Committee | Dr. Amirkianoosh Kiani |
| Research Supervisor | Dr. Jana Abou-Ziki |
| Examining Committee Member | Dr. Martin Agelin-Chaab |
| Thesis Examiner | Dr. Sayyed Ali Hosseini |

The above committee determined that the thesis is acceptable in form and content and that a satisfactory knowledge of the field covered by the thesis was demonstrated by the candidate during an oral examination. A signed copy of the Certificate of Approval is available from the School of Graduate and Postdoctoral Studies.

# Abstract

Spark-Assisted Chemical Engraving (SACE) is a promising method for machining glass micro-parts and devices. However, intricate control requirements linked to the gas film surrounding the tool present a significant challenge in SACE. While several studies have explored the influence of SACE parameters on the gas film, there exists a literature gap regarding the impact of voltage signal shapes on this film. The thesis fills this void by investigating diverse voltage signal shapes designed to enhance the gas film stability. A robust methodology was established linking gas film properties to investigate the effects of signal shapes on the gas film. The research applied these findings to machining applications, establishing correlations between signal shapes and machining outcomes. Key contributions include a refined methodology for gas film evaluation, advancements in understanding signal shapes' impact on the process, identification of optimal parameters, and potential improvements in machining through a custom signal shape design.

**Keywords:** SACE; Glass; Gas film; Micromachining; ECDM

# Author's Declaration

I hereby declare that this thesis consists of original work of which I have authored. This is a true copy of the thesis, including any required final revisions, as accepted by my examiners. I authorize the University of Ontario Institute of Technology (Ontario Tech University) to lend this thesis to other institutions or individuals for the purpose of scholarly research. I further authorize University of Ontario Institute of Technology (Ontario Tech University) to reproduce this thesis by photocopying or by other means, in total or in part, at the request of other institutions or individuals for the purpose of scholarly research. I understand that my thesis will be made electronically available to the public.

<div align="right">MARWAN SHERIF ELDIASTY</div>

# Statement of Contributions

I preformed the idea synthesis, methodology, investigation, analysis, original drafting, review and editing. The artificial neural network is part of Seyed-Mahmoud Seyedi-Sahebari's PhD work. The SACE machining setup was developed by Zahraa Bassyouni. Jana Abou-Ziki preformed the conceptualization, review, editing, supervision, and provision of resources.

**Parts of Chapter 1:**

*Hamed, Hazem; Eldiasty, Marwan; Seyedi-Sahebari, Seyed-Mahmoud; Abou-Ziki, Jana. "Applications, materials, and fabrication of micro glass parts and devices: An overview." Materials Today, 66 (2023) 194-220. https://doi.org/10.1016/j.mattod.2023.03.005. (Published).*

**Parts of the work described in Chapter 3:**

*Seyedi-Sahebari, Seyed-Mahmoud; Eldiasty, Marwan; Abou-Ziki, Jana. " Investigating SACE Gas Film Anatomy via Comprehensive Analysis of Current Signal and Video Recording" Manufacturing Letter, November 2023. (Submitted).*

**Parts of the work described in Chapter 3 and 4:**

*Eldiasty, Marwan; Seyedi-Sahebari, Seyed-Mahmoud Abou-Ziki, Jana. (2023) " Experimental Investigation and Characterization of the Gas Film Stability in the SACE Process." Proceedings of the Canadian Society for Mechanical Engineering (CSME) Annual Conference, Université de Sherbooke, May 2023. (In Press).*

**Parts of the work described in Chapter 4:**

*Eldiasty, Marwan; Seyedi-Sahebari, Seyed-Mahmoud; Abou-Ziki, Jana. " The Effect of Applying Sinusoidal-shaped Signals on the gas film around the SACE Machine Tool" Manufacturing Letter, August 2023. (Under Review).*

Chapters 4, and 5 of this thesis are currently being prepared for the submission of an article to a respected journal in the field.

# Acknowledgements

Bryant, a relentless spirit, and an enduring inspiration. His dedication, perseverance, and commitment to excellence have deeply impacted me, serving as a reminder to approach life with passion and unwavering determination. Thank you, Kobe.

# Table of Contents

# List of Tables

# List of Figures

# Abbreviations

**ANOVA** Analysis Of Variance.

**CMC** Critical Micelle Concentration.

**CSV** Comma Separated Values.

**CTAB** Cetyltrimethylammonium Bromide.

**DAC** Digital To Analog Converter.

**DC** Duty Cycle.

**DX-13** Design Expert Software.

**FPS** Frames Per Second.

**GRBL** Gcode Reference Block Library.

**HAZ** Heat Affected Zone.

**KOH** Potassium Hydroxide.

**LED** Light Emitting Diodes.

**LUT** Look UP Tables.

**MRR** Material Removal Rate.

**NaOH** Sodium Hydorxide.

**NEMA** National Electrical Manufacturers Association.

**PFV4** Photron Fastcam Viewer.

**SACE** Spark-Assisted Chemical Engraving.

**SDS** Sodium Dodecyl Sulfate.

**UGS** Universal Gcode Sender.

# Chapter 1

# Introduction

## 1.1  Background

Over the last few decades, the concept of miniaturization has captured the intrest of both the academic and industrial worlds. Miniaturization offers promising solutions in various fields that allow for high resource utilization, tightly controlled microenvironments, multifunctional platforms, and automation [1]. Mechanical [2], optical [3], and electrical [4] devices that are on a micro-scale are becoming more prominent as the drive toward miniaturization continues. The devices' form, size, and material must be addressed for the devices to be properly integrated and packaged in a successful industrial product that can match consumer expectations for intelligence and multifunctionality. Glass is a candidate material for fabricating micro parts and devices as it possesses notable characteristics required in a wide range of applications [5]. These characteristics include thermal resistivity, bio-compatibility, optical clarity, chemical inertness, and renewability, to name a few [6].

Fabricating such material on a micro-scale requires specific micromachining capabilities. Although glass offers a unique combination of characteristics and properties, it is a hard and brittle material that cannot be conveniently fabricated on a micro-level [7]. Long machining times, high machining costs, and poor surface quality make manufacturing smooth, high-aspect-ratio structures challenging [8]. However, the advancements in the micromanufacturing field have allowed for complex machining

conditions, and geometries [9].

The Spark-Assisted Chemical Engraving process (SACE) stands out as a glass microfabrication method with distinct trade-offs in terms of the necessary attributes within this field, especially when compared to other well-established processes. This cost-effective process is capable of fabricating features with aspect ratios exceeding 10 while maintaining a surface roughness of less than 0.5 $\mu m$ at a relatively high machining speed (up to 100 $\mu m/min$) [10]. SACE relies on thermally accelerated etching, initiated by applying voltage between a tool electrode and a counter electrode immersed in an electrolyte. Upon reaching a critical voltage, hydrogen gas bubbles form a gas film around the tool electrode. The gas film effectively insulates the tool, leading to a subsequent voltage drop. This drop induces a high electric field, resulting in sparking arc discharges across the tool's surface.

## 1.2   Research Gap

SACE has shown promising results and stands as a viable choice for machining glass microparts and devices. Yet, the gas film surrounding the tool electrode poses a significant challenge in SACE applications due to its intricate control requirements. The gas film experiences rapid recurring formation and breakdown cycles, occurring within milliseconds, significantly influencing the local electrolyte flow dynamics around the tool and consequently affecting surface quality. Despite SACE's potential, its full comprehension remains limited, primarily due to the lack of a well-defined correlation between gas film properties and machining performance. In literature, several studies have explored the impact of SACE parameters on the gas film. However, there remains a gap in the literature concerning the influence of signal shapes on the gas film. The need for a stable gas film becomes pivotal to ensure consistent machining outcomes.

## 1.3 Motivation and challenges

Literature acknowledges a strategy to enhance gas film stability by deliberately controlling its thickness through controlled gas film generation and breakdown using a pulsed voltage signal shape. This approach has demonstrated enhanced machining quality. Nevertheless, further improvement can be realized by leveraging the hysteresis effect. Described initially by Kellogg in 1950, this effect allows for slight voltage reduction (1-2 volts below the critical threshold) while preserving the gas film's presence around the tool. Wüthrich et al. [11] outlined this hysteresis phenomenon, primarily attributed to the dynamics of bubble formation on the tool. However, this approach hasn't been practically employed until now.

This thesis aimed to explore various voltage signal shapes, following Kellogg's strategy. Given the absence of a defined correlation between gas film properties and machining performance, a study was carried out to measure the gas film's physical and dynamic properties. Signal processing helped analyze gas film patterns using current-time plots. Critical dynamic parameters, including average lifetime, gas film formation duration, and discharge current standard deviation and frequency, were investigated. Physical parameters such as thickness, dimensions, and visual gas film behavior were assessed using a high-speed camera. Once a robust methodology correlating the gas film's physical and dynamic properties was established, this work explored how different signal shapes affect gas film behavior and their interaction with other pivotal SACE parameters. The subsequent phase aimed to apply these findings to a machining application to establish correlations between signal shapes and machining outcomes. Finally, the thesis evaluated the proposed signal shapes and explored avenues for further enhancement.

# Chapter 2

# Literature Review

The following literature review delves into the studies of Spark Assisted Chemical Engraving (SACE) and its aspects within the field of precision engineering. It commences with a comprehensive survey of SACE. Following this, the focus turns to the machining characteristics intrinsic to SACE. This includes an in-depth exploration of the operational principles that govern SACE, encompassing a detailed analysis of its machining mechanism, as well as the pivotal parameters that underpin its efficiency. Furthermore, this review extends its study to the gas film phenomenon. It explains the mechanisms responsible for gas film formation and offers insights into the factors influencing the stability of the gas film. A profound understanding of gas film behavior is crucial, as it directly impacts the precision and effectiveness of SACE.

## 2.1   Spark Assisted Chemical Engraving (SACE)

In 1968, Karafuji and Suda conducted the pioneering investigation of SACE, introducing the concept of electrochemical discharge phenomena and reporting the successful etching of micro-holes in glass [12]. Subsequently, various names have been used to refer to this process, including 'Discharge Machining of Nonconductors' by Cook et al. [13], 'Electrochemical Arc Machining' by Kubota [14], 'Electrochemical Discharge Machining' by Ghosh et al. [15], 'Micro Electro-chemical Discharge Machining' by Fascio et al. [16], 'Electro-Chemical Spark Machining' by Jain et al. [17], and 'Spark

Assisted Chemical Engraving' by Langen et al. [18]. The existence of various names for the process highlights its complexity and the different theories put forth to explain the nature of electrical discharges. For the sake of clarity and to avoid confusion with similar processes, this study will exclusively refer to the process as SACE. A timeline showcasing the most significant developments in SACE is illustrated in Fig. 2.1 Since 2014, research in SACE has branched out into various disciplines, such as process parameter optimization, gas film stability enhancement, discharge mechanism analysis, material removal improvement, and exploration of different process variants. Each of these areas will be covered in its respective following section.
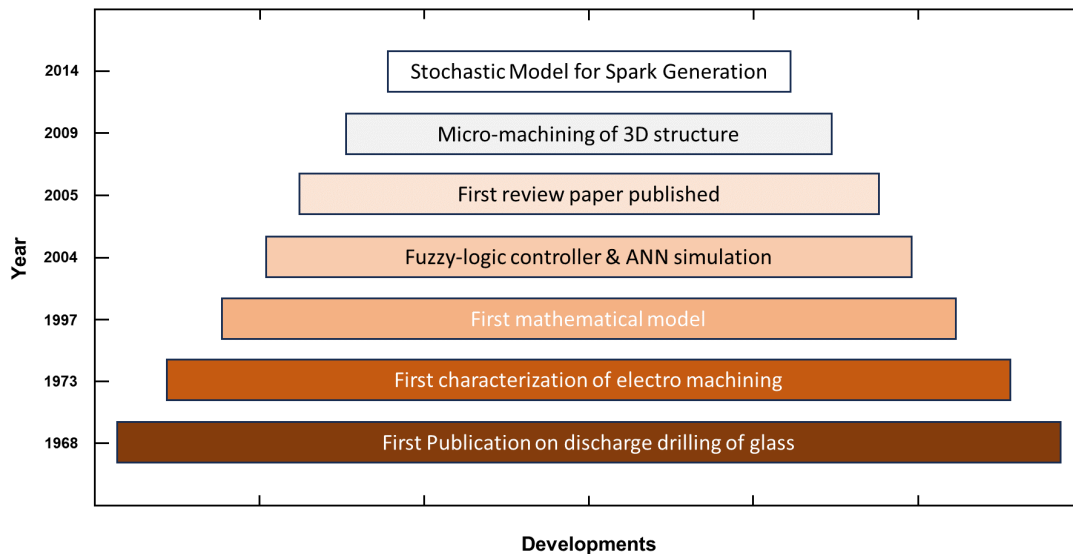


Figure 2.1: Notable developments in SACE.

SACE is a versatile non-conventional process for micro-level machining. Its distinct advantage lies in its ability to machine both conductive materials, such as stainless steel [19], and non-conductive materials, such as glass [20] and ceramics [21]. This versatility enables its application in machining a wide range of hard and brittle materials [22]. SACE is known for its cost-effectiveness and straightforward setup, allowing for the fabrication of features ranging from 1D to 2.5D. It also has the capacity to drill holes with aspect ratios (*Diameter to length*) exceeding 10. In addition to main-

taining an acceptable resolution with surface roughness of less than 0.5 microns at a relatively high machining speed (100 µm/min) with a minimal need for additional support systems and consumables [10]. These attributes position the SACE process as an ideal choice for rapid prototyping of glass micro-parts and devices, such as microfluidic chips and biomedical devices [23].

Unlike other micromachining processes, SACE has the capability to eliminate intermediate steps in the production of microfluidic devices by allowing direct glass-to-glass bonding [24]. In addition, it has the potential to control surface composition and texture during machining in a single step, setting it apart from most other micromachining methods. Moreover, it provides an acceptable trade-off between surface roughness and aspect ratio compared to other prominent micromachining processes, as shown in Fig. 2.2.
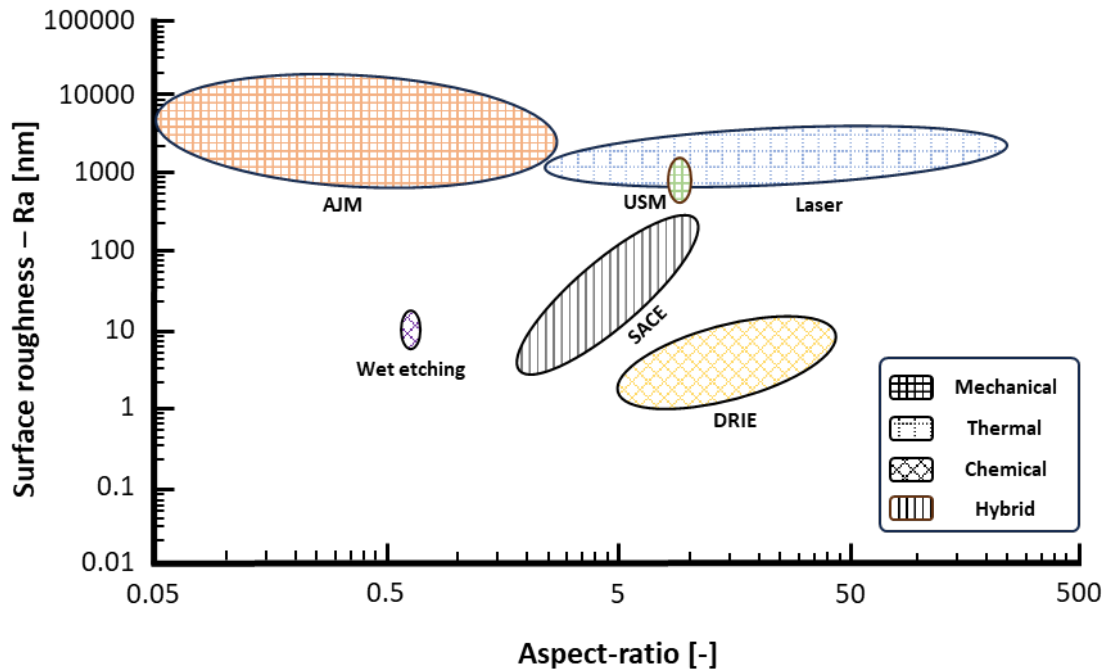


Figure 2.2: Surface roughness - $R_a$ (nm) vs aspect ratio for micromachining technologies. Adapted from [25]

Furthermore, SACE offers reasonable machining speeds, as illustrated in Fig. 2.3, which shows a graph comparing speed and aspect ratio for various micromachining processes.
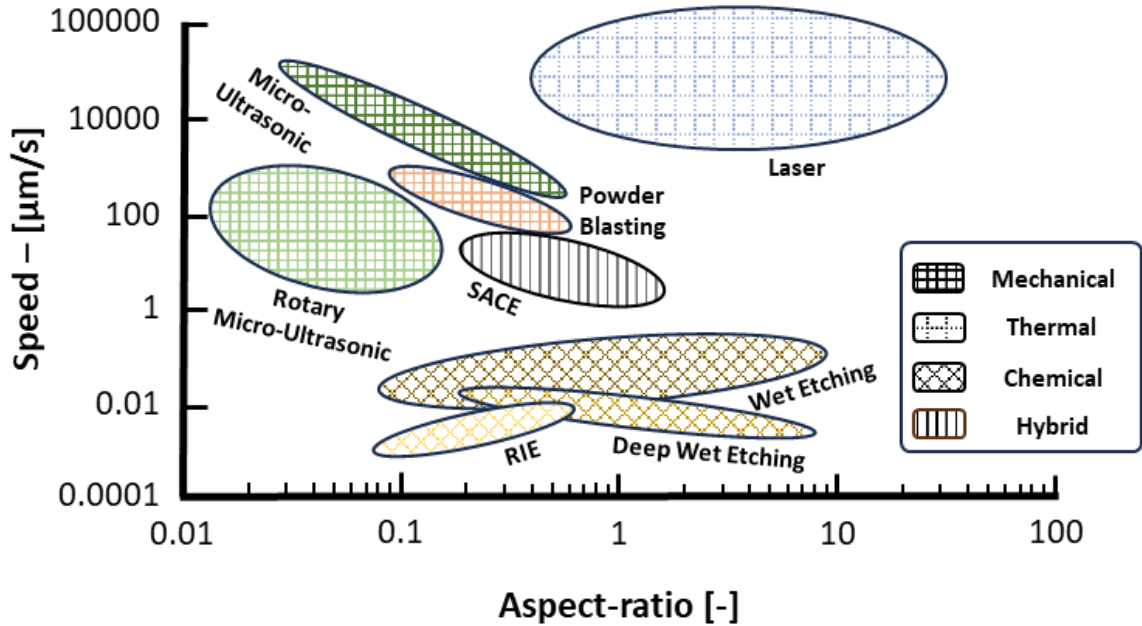


Figure 2.3: Speed ($\mu$m/s) vs aspect ratio for micromachining technologies. Adapted from [25]

## 2.2 Process Characteristics

This section of the literature review focuses on the machining characteristics of SACE. It includes an overview of the machining mechanism and the key process parameters, namely, the choice of electrolyte, tools, and electric parameters. Understanding these machining aspects is essential for comprehending the precision and efficiency of SACE. This section lays the groundwork for the subsequent analysis in this master's thesis, bridging the theoretical framework of SACE with its practical application.

## 2.2.1 Machining Mechanism

A basic SACE operation commences with the tool electrode approaching the workpiece immersed in the electrolyte at a distance typically around 25 µm. The power supply delivers the voltage used to apply potential across both the tool (Cathode) and the counter-electrode (Anode). Electrolysis occurs, leading to the formation of gas bubbles, which creates an electrochemical cell. This process is driven by the potential difference between the two electrodes, resulting in the generation of hydrogen and oxygen gas bubbles at the tool electrode and the auxiliary electrode, respectively. When the applied voltage surpasses the critical voltage ($U_{crit}$), hydrogen gas bubbles are generated near the tool electrode at a higher rate than those on the electrolyte surface. Consequently, the hydrogen gas bubbles tend to accumulate around the tool electrode, where they coalesce into a larger single gas bubble, forming a hydrogen gas film [26].

The gas film functions as an insulator, effectively isolating the tool electrode from the electrolyte and causing current breakdown, resulting in a voltage drop. Furthermore, the isolation of the tool electrode results in a sufficiently high electric field across the dielectric film, leading to the occurrence of arc discharge (sparks) [27]. Sparks originate at the sharp edges of the tool electrode due to the high current density at these regions [28]. During the discharge period, a substantial number of electrons bombard the workpiece surface near the tool electrode. This electron bombardment elevates the work material's temperature and results in material melting. In addition, the process is assisted by chemical etching, leading to the erosion of the workpiece and material removal [29]. The process mechanism can be summarized in four primary stages: (i) electrolysis, (ii) generation and accumulation of hydrogen gas bubbles, (iii) bubble coalescence and gas film formation, and (iv) sparking, as illustrated in Fig. 2.4.
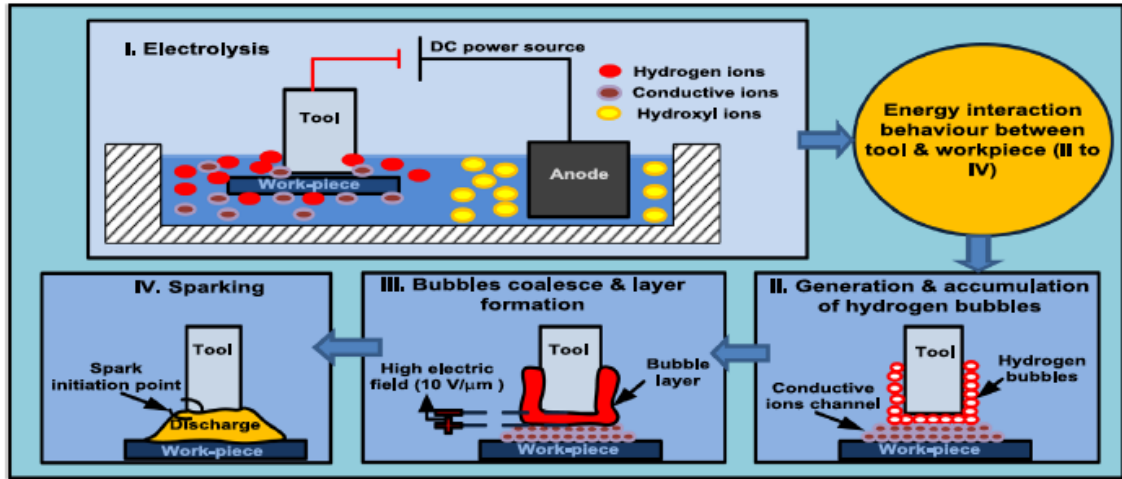
Figure 2.4: Process mechanism of SACE. Referenced from [30]

## 2.2.2 Process Parameters

SACE, as explained earlier, features a straightforward setup and well-defined procedures. However, the literature indicates that multiple process parameters simultaneously and directly influence the process performance.
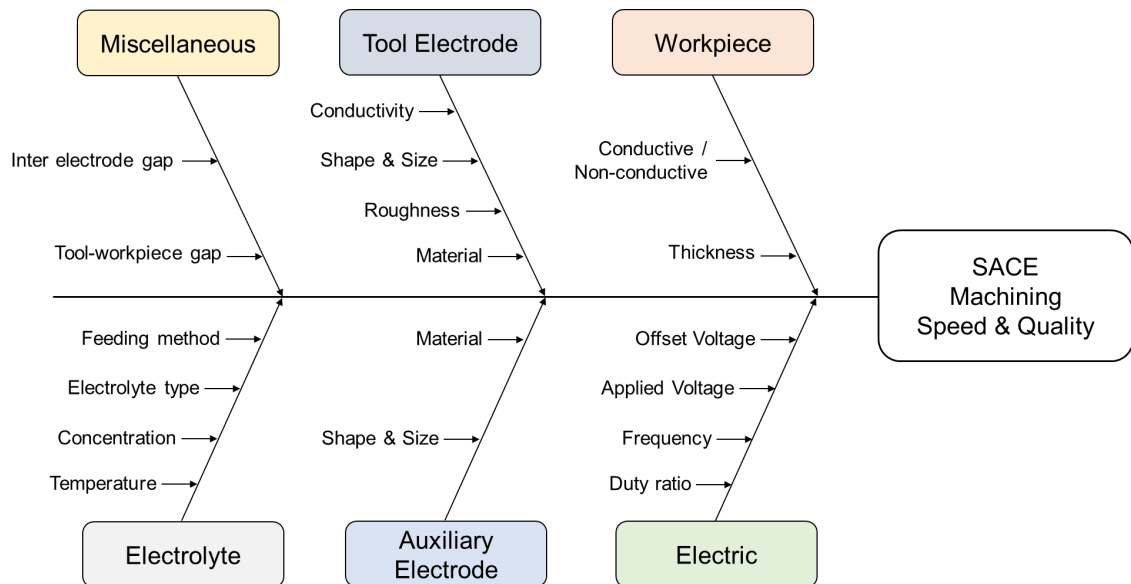


Figure 2.5: Cause and effect diagram showing SACE parameters.

Fig. 2.5 illustrates these parameters, classified into six categories: tool electrode, workpiece, electrolyte, auxiliary electrode, power source, and the presence of gaps between the two electrodes and the tool-workpiece.The following section will discuss the major process parameters and their impact on the process.

*Electrolyte*

The selection of electrolyte plays a critical role in the machining process, as it has a significant impact on the etching rate, surface quality, and hole overcut [31]. A summary of the electrolyte effects is shown in Fig. 2.6.
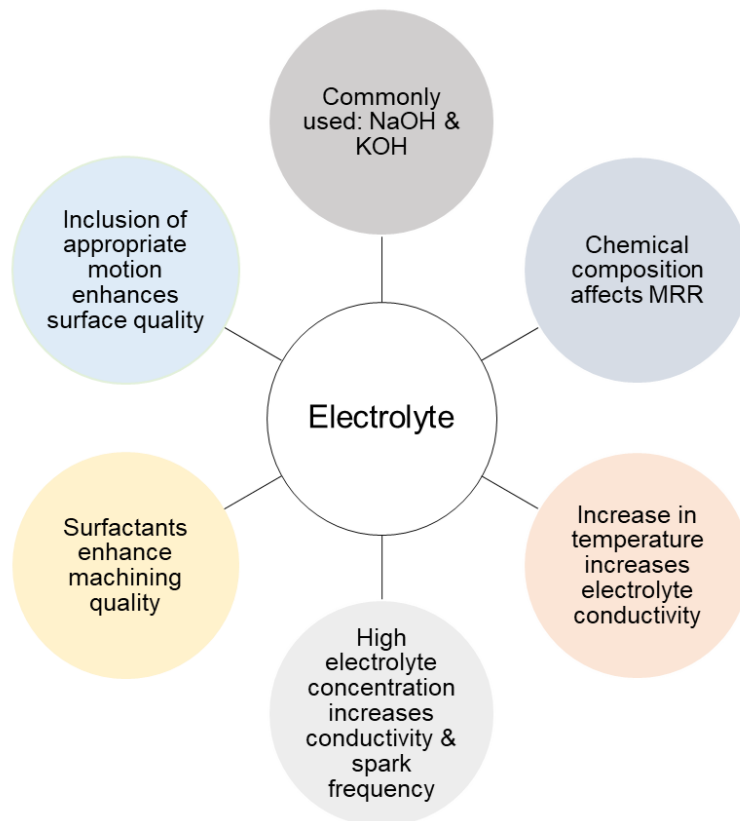


Figure 2.6: Summary of the electrolyte effect on SACE.

In literature, Sodium Hydroxide (NaOH) and Potassium Hydroxide (KOH) are the two most commonly used electrolytes, with NaOH known for its high viscosity, and KOH distinguished by its high conductivity. Additionally, other electrolytes

such as Sodium chloride (NaCl), Sodium Nitrate (NaNO$_3$), Hydrochloric acid (HCl), Sulfuric acid (H$_2$SO$_4$) have been used [32]. Generally, alkaline solutions show better performance compared to acidic ones, as acids tend to increase surface roughness. In a SACE drilling experiment on soda lime glass, Harugadi et al. [33] compared KOH, a base solution, and H$_2$SO$_4$, a sulfuric acid solution. The results showed that bubble generation in the acidic solution was nearly negligible, leading to a poor material removal rate (MRR). Gupta et al. [34] conducted an experimental comparison of the MRR and overcut using three different electrolytes (NaCl, NaOH, and KOH) at the same concentration of 25 wt% during glass drilling.

The results showed that NaOH exhibited a significantly higher MRR compared to KOH and NaCl, with values being 3.8 and 9.7 times higher, respectively. On the other hand, KOH resulted in a smaller overcut compared to NaOH and NaCl, with values being 1.26 and 3.26 times less, respectively. Furthermore, Rajput et al. [35] investigated the impact of different electrolytes (NaOH, KOH, NaCl) and their concentrations on the MRR during machining. The findings revealed that NaOH outperformed the other electrolytes, achieving the highest MRR. Additionally, as the electrolyte concentration increased, the material removal rate improved. The high MRR with NaOH was attributed to the presence of OH- ions, which play a crucial role in the etching action.

The levels of electrolyte concentration, in addition to the electrolyte composition, have an impact on the MRR and surface quality. Kolhekar & Sundaram [36] explored different concentrations of NaOH electrolyte and found that higher concentrations promoted thermal mechanism, while lower concentrations enhanced chemical etching. Conversely, Mallick et al. [37] investigated glass machining with NaOH electrolyte and observed that increasing the electrolyte concentration resulted in higher MRR due to a greater frequency of sparking. Madhavi et al. [38] and Bellubi et al. [39] both also confirmed that higher electrolyte concentration leads to increased MRR.

The electrolyte temperature affects the SACE process. Jain et al. [40] discovered that higher electrolyte temperatures enhance conductivity, thereby accelerating the electrolysis process. This accelerated electrolysis leads to an increased formation of hydrogen gas bubbles at the cathode, resulting in more frequent sparking and a higher MRR. The study showed that as the electrolyte temperature rises from 35°C to 80°C, the conductivity of the electrolyte increases from 345 to 650 mS/cm. This increase in conductivity leads to improved ionic mobility, thus facilitating the chemical etching process.

The addition of surfactants to the electrolyte enhances surface quality in SACE. Laio et al. [41] investigated the impact of adding 0.2% Sodium Dodecyl Sulfate Surfactant (SDS) to a KOH electrolyte during quartz glass machining, leading to increased current density and improved machining, thus achieving a 27% enhancement in etching capability. Similarly, Wüthrich et al. [42] added 20 mL of soap to 200 mL of NaOH electrolyte, resulting in a 25% decrease in critical voltage. In another study, Sabahi et al. [43] conducted research on the effects of adding (SDS) and cetyltrimethylammonium bromide (CTAB), to the electrolyte. These surfactants were introduced to 25wt% NaOH and KOH solutions, resulting in the creation of microchannels with enhanced MRRs and improved surface quality, as shown in Fig. 2.7.
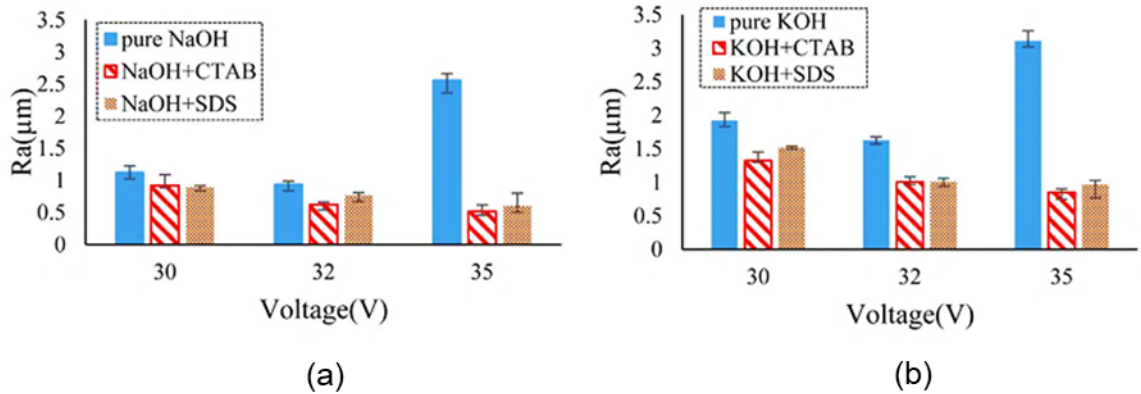


Figure 2.7: Surface roughness using surfactants (SDS and CTAB) (a) NaOH 25%wt (b) KOH 25%wt [43].

*Tool Electrode*

The tool electrode plays a pivotal role in the SACE process, with its material, geometry size, wettability, feed rate, and rotation impacting the surface quality of the machined parts. An overview of the effects of the tool parameters is illustrated in Fig. 2.8.
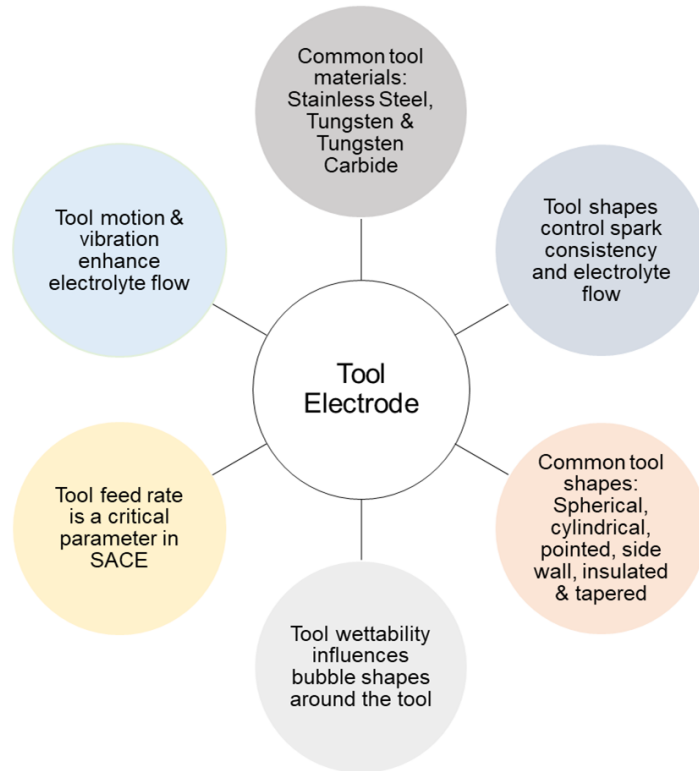


Figure 2.8: Summary of the tool effect on SACE.

Yang et al. [44] conducted a comparative study on the impact of three different tool materials: tungsten, tungsten carbide, and 304 stainless steel. Notably, tungsten carbide exhibited the smallest hole diameters and the least amount of tool wear. Abou Ziki et al. [45] and Zhan et al. [46] did similar studies using three distinct tool electrodes: tungsten, steel, and 316L stainless steel. Remarkably, 316L stainless steel demonstrated minimal tool wear due to its highest thermal expansion. Furthermore, Jawalkar et al. [47] established that stainless steel outperformed copper in terms of tool wear. The effectiveness of textured stainless-steel tools was showcased in

[48], where MRR and machining depth saw enhancements of 19.27% and 64.81%, respectively. These experiments also yielded notable reductions in width overcut by 122.26% and surface roughness by 26.96%. Fig. 2.9 outlines the materials researched in SACE literature.
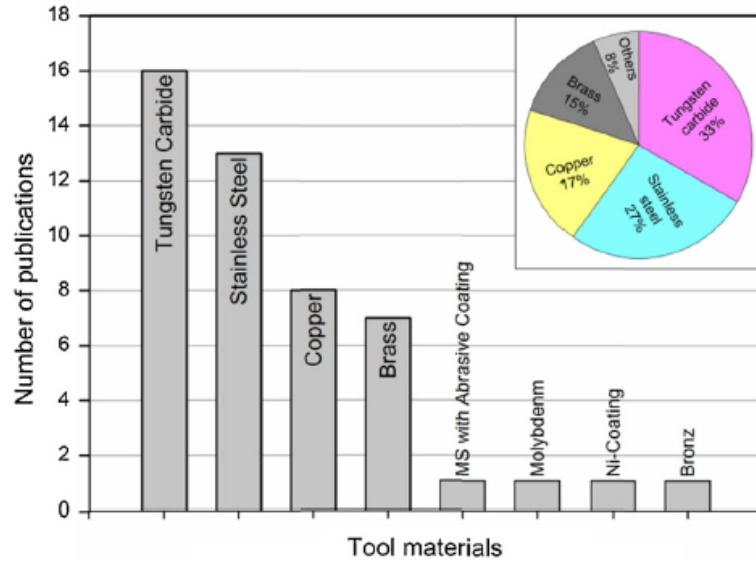


Figure 2.9: Tool materials researched in SACE. Referenced from [49].

The geometry of the tool electrode significantly influences spark consistency, resulting in a range of machining effects as indicated in multiple studies [50–53]. The literature has examined various tool shapes like flat side walls [54], side-insulated designs [55], spherical tools [50], and needle-shaped configurations [56]. These different shapes have shown enhancements in electrolyte flow and surface quality. An overview of the influences of tool shapes is depicted in Fig. 2.10.
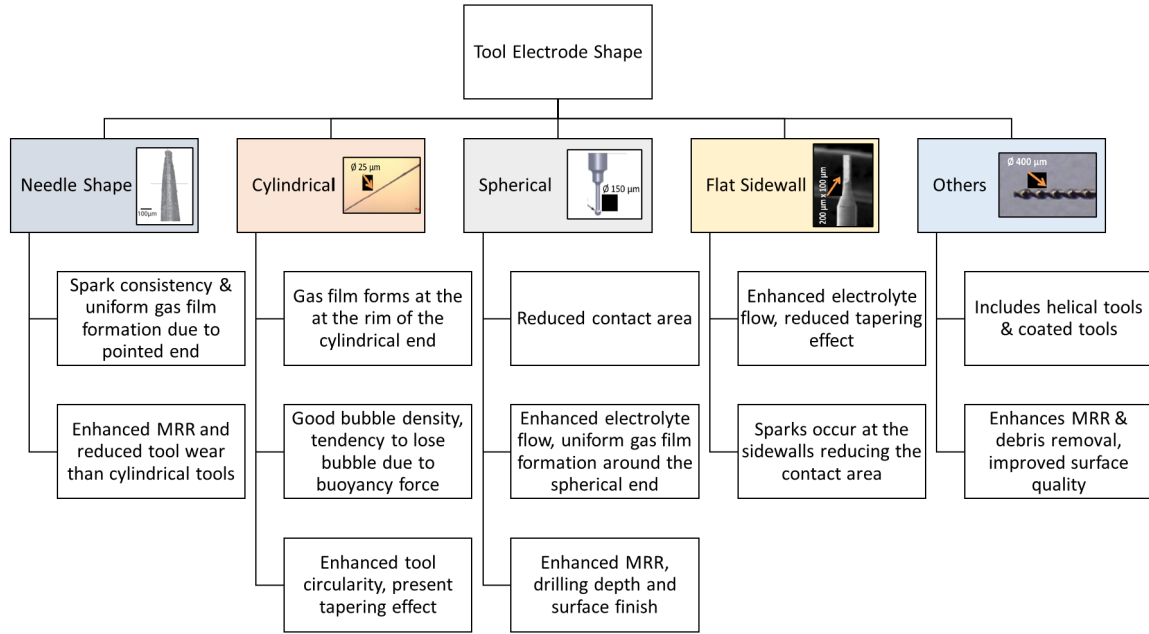
Figure 2.10: Summary of different tool shapes effects on the SACE process.

*Applied Voltage*

Voltage parameters, including magnitude, frequency, and signals-shape, have a significant impact on gas film formation and sparking frequency within the SACE process, consequently influencing both the MRR and machining quality. An overview of the effects of applied voltage is presented in Fig. 2.11.Sarkar et al. [57] conducted a mathematical modeling investigation and found that the applied voltage has a predominant influence over key parameters such as MRR, overcut, and heat affected zones (HAZ), surpassing the effects of electrolyte concentration and inter-electrode gap. Subsequent researchers have also highlighted the significance of applied voltage on the MRR [58–60]. Increasing the applied voltage magnitude results in a higher MRR due to the increased generation of hydrogen bubbles, concluding in amplified discharge energy within the sparking zone [61]. Moreover, the increase of applied voltage correlates with a corresponding increase in machining depth because the field emission law suggests that machining speed is an approximate function of applied

15

voltage [62]. Lizo et al. [63], investigated the impact of varied voltage levels (35V, 40V, 45V) on MRR. The findings showed that the MRR increases as the voltage is incrementally raised from 35V to 45V, a phenomenon attributed to the rate of sparking. Nonetheless, excessively elevated voltage levels showed the emergence of thermal cracks, a trend confirmed by the work of Cao et al. [64]. In addition, Jawalkar [65] reported a decrease in MRR due to the accumulation of debris within the spark gap, thereby impeding the removal of entrapped debris by the electrolyte.
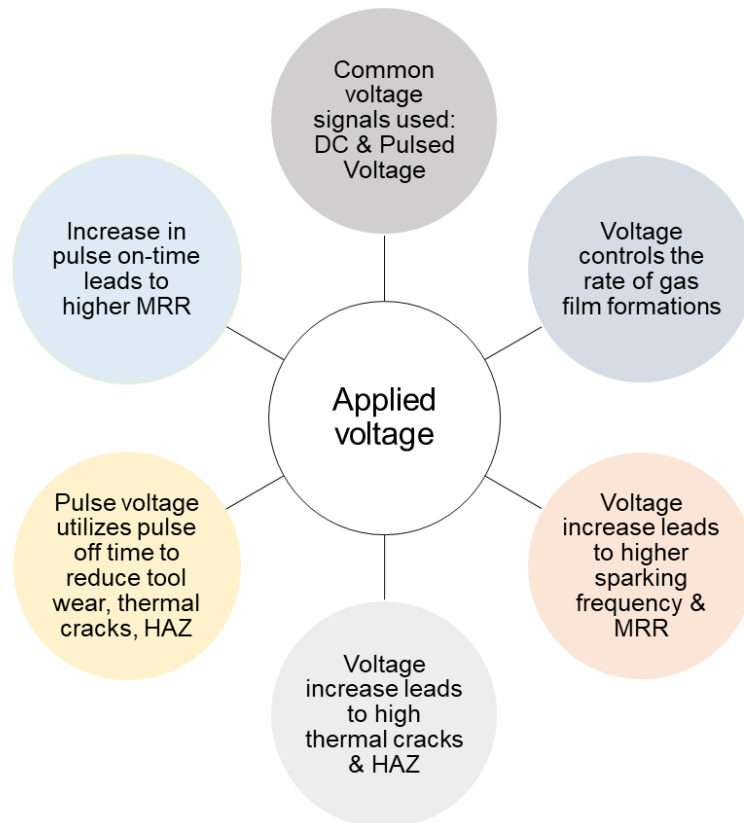


Figure 2.11: Summary of electric parameters effect on the SACE process.

The conventional method in SACE machining involved employing a rectified DC voltage; however, this approach was associated with the drawback of inducing overcut and thermal cracks due to the continuous discharge of thermal energy. Over the last two decades, the adoption of pulsed voltage in SACE machining has gained popularity to address these shortcomings. One significant benefit of utilizing pulsed voltage is its ability to effectively prevent overcut. This capability is attributed to the cooling effect

16

that occurs during the pulse's off time. This phenomenon is visually demonstrated in the machined profiles illustrated in Fig. 2.12.
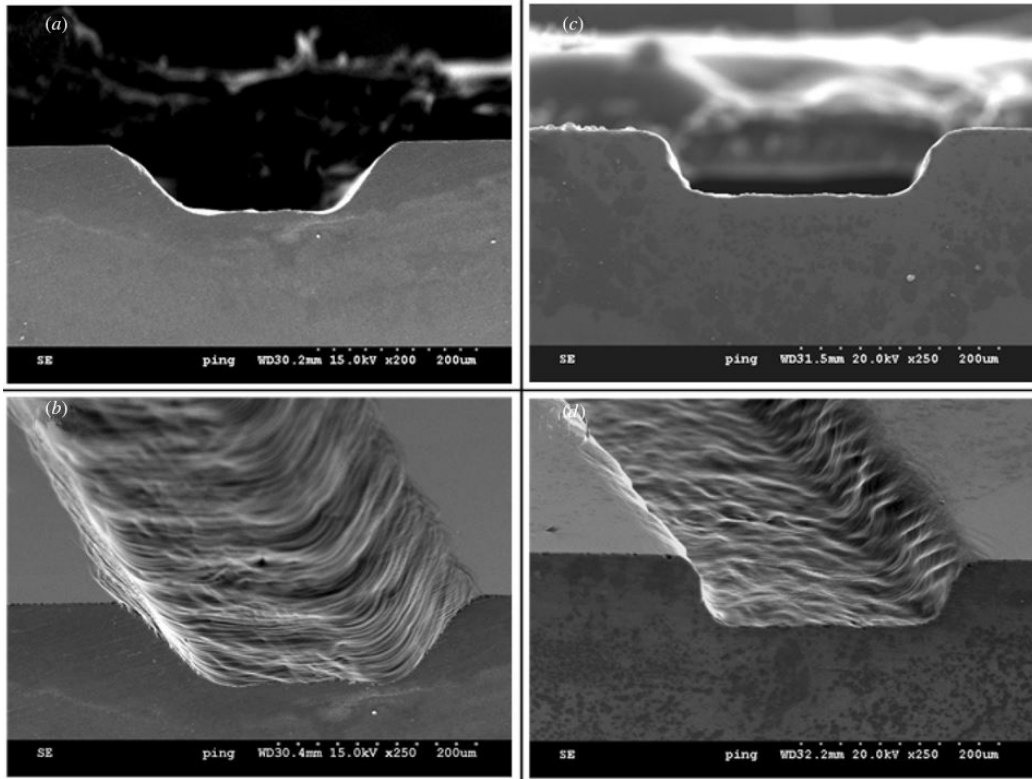


Figure 2.12: Micro machining with different applied voltage. (a), (b): DC supply Voltage 40 V, (c), (d): Pulse supply Voltage 40 V. Referenced from [66]

Furthermore, Kim et al. [67] adopted a pulsed voltage approach, varying frequencies, and duty ratios, to mitigate the impacts of thermal damage. The findings unveiled that an increase in frequency and a decrease in duty ratio correlated with a reduction in the extent of the HAZ. Zheng et al. [68] confirmed these observations by noting a decrease in the time required for gas film formation. In their experimental setup, a pulse on time of 2 ms was chosen for conducting tests with pulsed voltage, while the pulse-off time underwent adjustments. Noteworthy is the significant reduction in entrance diameter from 570 $\mu$m, when using a rectified DC voltage, to 340 $\mu$m was applied without any instances of crack formation. However, this approach resulted in an increase of machining time from 40s to 160s. This phenomenon was attributed to the constrained discharge energy per unit and the considerable energy

consumption for electrolyte heating. Moreover, Zhang et al. [69] observed a decrease in the gas film formation time to approximately 0.05 ms as the amplitude of the applied pulses increased to 25 V. Employing a frequency of 500 Hz and a 50% duty cycle, it was noted that with a lower magnitude (19 V), the overcut was smaller, and fewer micro-cracks were detected compared to the conditions at 25 V. However, this reduction in voltage led to a significant increase in machining time, extending from 48 s at 25 V to 130 s at 19 V. While the pulsed method proves effective in improving machining quality, it introduces the challenge of diminished machining efficiency.

## 2.3 Gas film

The gas film surrounding the tool electrode represents a significant challenge in SACE applications, primarily attributed to its inherent complexity in terms of control. The shape of the gas film directly influences discharge activity, that results in impacting the machining quality of the process. Furthermore, the gas film undergoes continuous cycles of formation and breakdown throughout the machining process, occurring at intervals of mere milliseconds. This continuous process substantially affects the local dynamics of electrolyte flow around the tool, thus affecting the process quality and efficiency. The achievement of a stable gas film becomes a critical requirement to ensure consistent machining outcomes. The instability of the gas film has overshadowed the appeal of SACE for industrial applications. In this section, an overview of the gas film formation mechanism and strategies investigated for enhancing its stability are discussed.

### 2.3.1 Gas film formation

The gas film primarily forms from the coalescence of bubbles formed electrochemically on the electrode surface and the localized electrolyte evaporation driven by Joule heating. The generation of hydrogen gas stems from the electrochemical reaction taking place on the cathode, while oxygen gas generation is induced by the electrochemical

reaction on the anode electrode. The reactions are outlined as follows:

$$2H_2O + 2e^- \rightarrow 2(OH)^- + H_2 \; (On \; Cathode)$$

$$4(OH)^- \rightarrow 2H_2O + O_2 + 4e^- \; (On \; Anode)$$
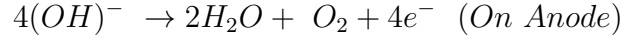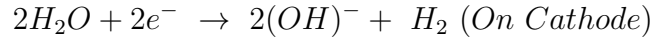
The increase in current density leads to higher bubble density and larger mean bubble radius. The layer of bubbles around the tool electrode is divided into three primary regions: the adherence region, the bubble diffusion region, and the bulk region. Within the adherence region, bubbles adhere to the electrode surface and undergo growth. During this phase, bubbles mechanically merge. As the bubbles reach the departure stage, they spread into the bubble diffusion region. In the third region, gas nears super-saturation close to the bulk electrolyte level, preventing further bubble expansion [70].

When the applied voltage reaches a critical threshold, the formation of the gas film begins through the coalescence of bubbles. The detachment of bubbles occurs due to the interaction between buoyancy force and surface tension. While the buoyancy force propels the bubbles upward, surface tension counteracts this motion. Based on the current-voltage characteristics in literature [71], the gas film formation cycle, shown in Fig. 2.13, was divided into five phases as follows:

- *(OA):* The Thermodynamic Phase: This phase is at lower voltages (below 2 V), preventing the flow of current and thus electrolysis does not occur.

- *(AB)*: The Ohmic Phase: During this phase, the current exhibits a linear relationship with terminal voltage, leading to the formation of a dense bubble layer around the tool electrode (Electrolysis).

- *(BC):* The Limiting Current Phase: Within this stage, the average current

reaches a saturation point, achieving a maximum value ($I_{crit}$), and bubbles coalesce.

- *(CD):* The Transition Phase: A gas film forms around the tool electrode as the mean current rapidly decreases. Typically, a current density of approximately 1 A/mm² is needed for gas film development. At this stage, the process's status could align with either the similar limiting current phase or the arc region, where machining becomes possible.

- *(DE):* The Arc Phase: In this phase, the presence of a gas film around the tool electrode is confirmed, and the tool electrode becomes fully isolated from the electrolyte. Current is transported through micro-level arc discharges.
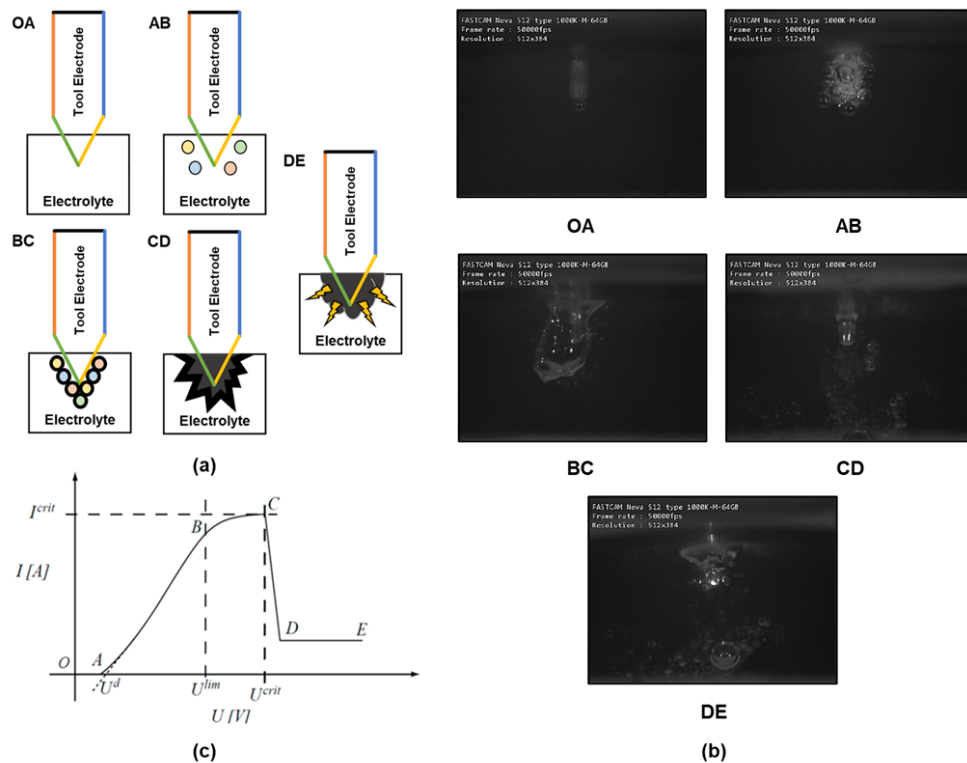


Figure 2.13: (a) Schematic of the gas film formation process. (b) High speed images corresponding to the 5 distinct regions of gas film formation. (c) The I–U characteristic curve during SACE.

### 2.3.2 Gas film characterization

The gas film is characterized by its physical and dynamic attributes. Its physical parameters include the thickness, dimensions, and visual behavior of the gas film, which can be determined through visual assessment using high-speed cameras. However, visual observation is challenging due to the turbulent nature of gas film formation. A sample of high-speed camera footage of gas film formation is shown in Fig. 2.14.
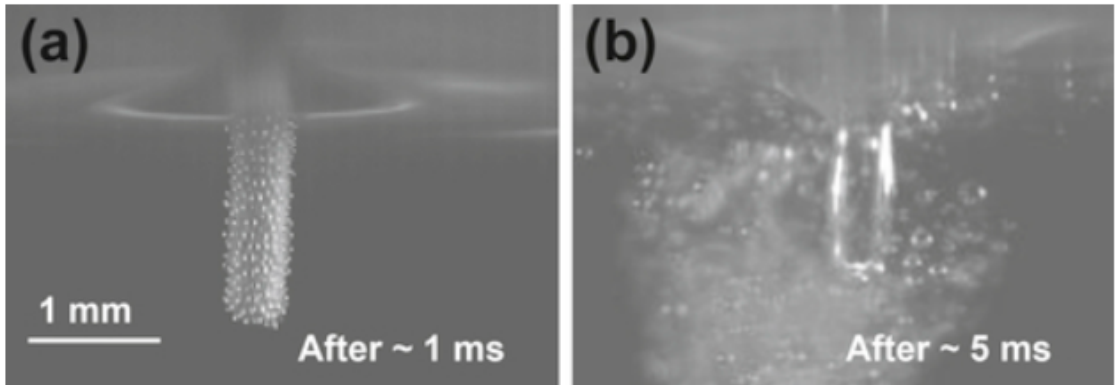


Figure 2.14: Formation of the gas film by coalescence. Image taken with a high-speed camera (Phantom V 9.1) in 35 wt% KOH. (a) Formation of a monolayer of bubbles. (b) After 5 ms, a thin gas film is formed. Refenced from [72].

The dynamic attributes of the gas film can be investigated using signal processing, which involves analyzing the signal patterns of the gas film using current-time plots [73]. Essential dynamic parameters include the average lifetime, mean formation duration of the gas film as well as the standard deviation and frequency of discharge current. Fig. 2.15 shows an experimental visual illustrating the current-time plot for a bubble to attain a size that permits coalescence.
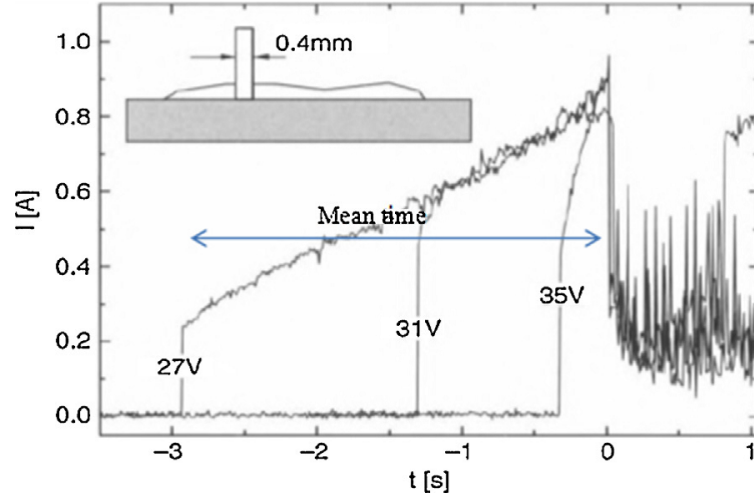
Figure 2.15: Current-time plot graph depicting the impact of different voltages on gas film formation. Referenced from [62].

### 2.3.3 Gas film stability

Improved stability is achieved when the gas film exhibits uniformity, reduced thickness, and consistent lifetime. Additionally, minimal fluctuations in the current signal, as evidenced by a low standard deviation of discharge current, contribute to this enhanced stability. The stability of the gas film depends on various parameters, including the impact of factors like buoyancy force and surface tension attributed to the temperature gradient between the tool electrode and electrolyte, the electrostatic force between the bubble and electrode, the wettability of the electrode surface with nucleation sites, the current density, electrolyte resistivity, tool radius, and the depth of tool immersion. These parameters are summarized in Fig. 2.16.
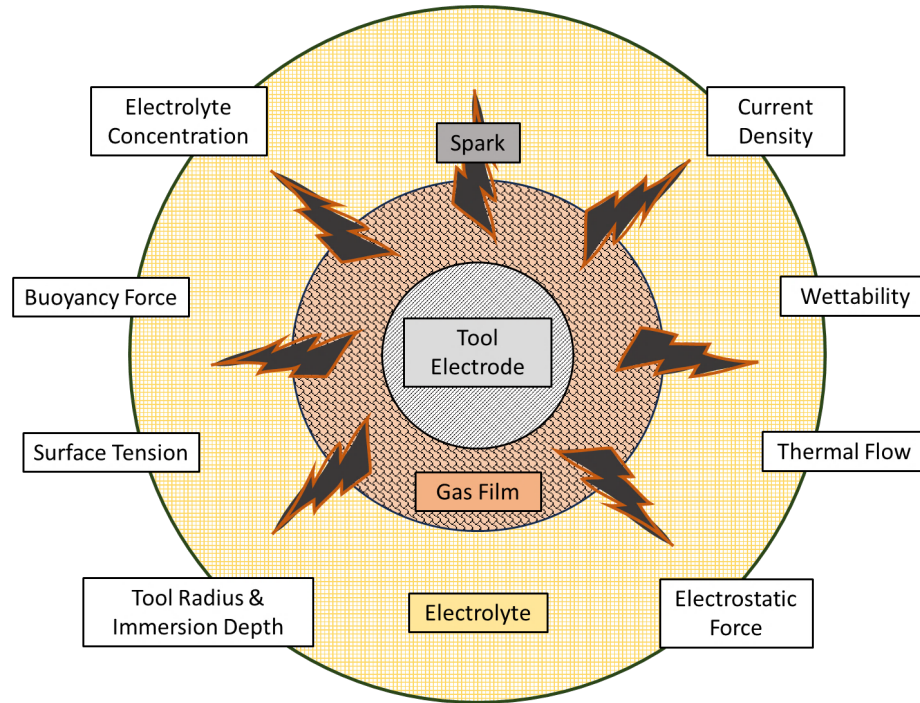
Figure 2.16: Parameters affecting the gas film.

Three strategies were recognized in literature to enhance gas film stability through reducing its thickness:

(i) *The utilization of hydrodynamic fluxes*

This strategy can be achieved by adopting either tool rotation or electrolyte rotation. Tool rotation introduces hydrodynamic effects that efficiently reduce the gas film thickness. Gautam and Jain [74] conducted a study to explore the potential of different tool kinematics. They observed enhanced gas film stability when utilizing a rotational tool with controlled feed. Furthermore, they noted a significant improvement in the maximum achievable machining depth when employing a tool with rotational motion.

(ii) *Controlling density of bubble nucleation sites*

Enhancing the density of nucleation sites for bubble formation involves control-

ling the spacing between active nucleation sites. This strategy can be achieved by increasing tool wettability, which can be done by applying surfactants [42]. Laio et al. [41] found that the introduction of the sodium dodecyl sulfate (SDS) surfactant into the electrolyte led to an increase in current density. This resulted in increased bubble release, brighter sparks, and a more stable current during the machining process.Moreover, Jiang et al. [75] pointed out that both surface tension and electrolyte density influence bubble development and film evolution. The square root of surface tension and electrolyte density demonstrates a linear correlation with the thickness of the gas film.

To mitigate overcutting during machining, the introduction of a surfactant to the electrolyte, which reduces surface tension, provides a method for reducing gas film thickness. This approach leads to lowered voltage and current requirements for material removal. An alternative strategy for enhancing bubble nucleation involves increasing the electrolyte concentration, thereby accelerating the electrolysis rate. This heightened electrolysis results in a greater quantity of $(OH^-)$ ions, leading to a reduction in surface tension. This reduction contributes to a thinner gas film and ultimately improves machining accuracy [76].

(iii) *Applying pulsed voltage*

The third strategy involves achieving gas film stability by intentionally generating and destroying the gas film in a controlled manner through the use of a pulsed voltage supply. The regulated cycle of building and destroying the gas film contributes to reduced fluctuations and enhanced machining reproducibility by reducing the thickness of the gas film. Experimental investigations confirm that the adoption of pulsed voltage enhances gas film stability, thus leading to a reduction in thermal damage during micro-drilled hole fabrication [77] and an improvement of over-cut in micro-groove machining [66].

Another strategy for achieving gas film establishment at lower voltages capitalizes on the hysteresis effect. As initially described by Kellogg in 1950 [78], once a gas film forms at a terminal voltage U exceeding $U_{crit}$, it becomes possible to slightly lower the voltage by 1-2 V below the critical threshold without losing the presence of the gas film around the tool. This hysteresis phenomenon occurs due to the dynamics of bubble formation on the tool, as outlined by Wüthrich et al. [11]. However, this method has never been used in practical applications until now.

# Chapter 3

# Methodology

In this section, an explanation of the methodologies employed to execute the experimental work outlined in the thesis is provided. A detailed account of the experimental setups, the strategies implemented for experiment control, the design of experiments, and the analysis methods employed to evaluate the gas film stability in this study are presented.

## 3.1   Gas film setup

The following section outlines the experimental setup employed to investigate gas film behavior, which was derived from the configuration employed in [79], as illustrated in Fig. 3.1. In this arrangement, machining operations were not conducted.
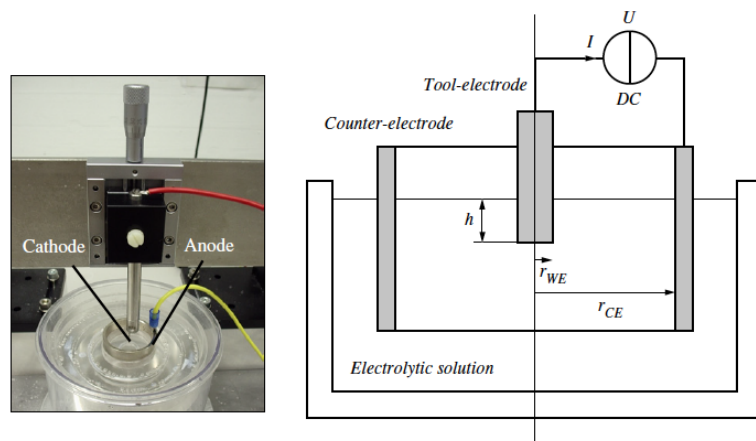


Figure 3.1: A typical gas film setup employed in the experiments done by Wuthrich et al. Referenced from [79]

The setup employed in this work is shown in Fig. 3.2. The processing cell was mounted on a stationary acrylic stage, restricting movement along the x-axis and y-axis. The machine tool head facilitated motion in the z-axis with a resolution of 0.1 mm/step controlled by an external Arduino board connected to a NEMA 17 stepper motor. The Arduino board received its commands from a Universal Gcode sender (UGS) platform, where calibration, speed adjustments, and movement commands were executed through a GRBL firmware. A cylindrical stainless-steel tool with a diameter of 500 $\mu$m and a steel circular-shaped ring served as the cathode and anode, respectively. The electrodes were connected to a Kepco BOP 4000 W DC power amplifier. A Tektronix AFG 1022 signal generator was used to determine the applied voltage, waveform, duty cycle, and frequency. Subsequently, the power was amplified through the Kepco amplifier. The processes current was measured through a Tektronix TCP 0020 current probe and collected using a Tektronix TBS 2000 oscilloscope. The data obtained from the oscilloscope was saved in CSV format and used to generate signal plots in MATLAB for signal processing.
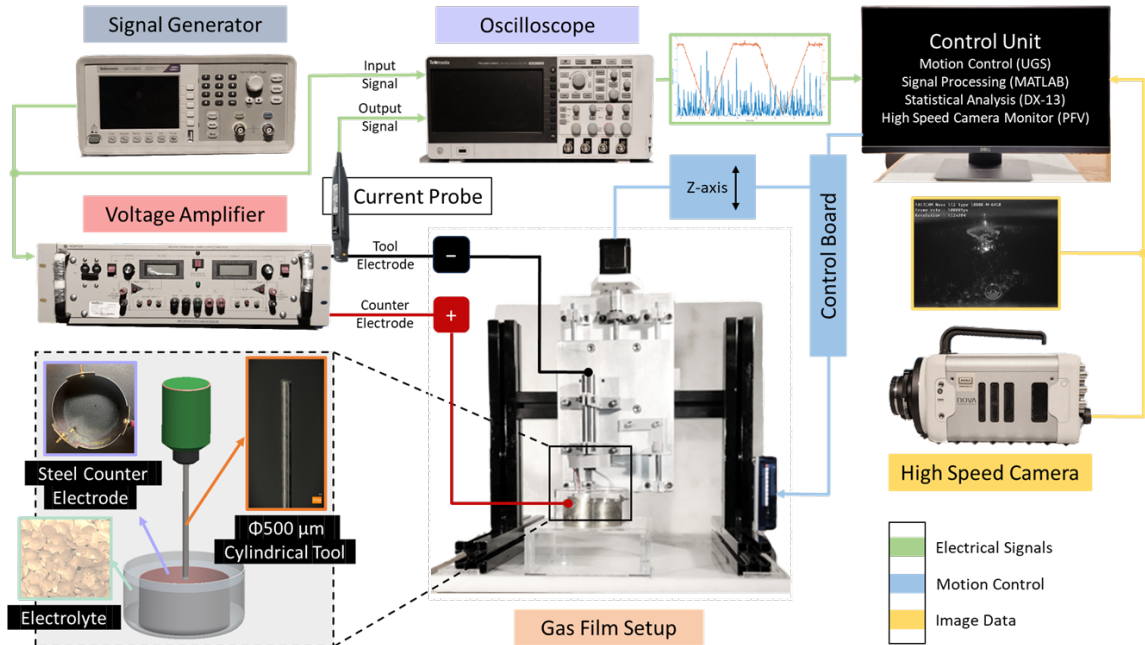


Figure 3.2: Gas film setup employed in the characterization experiments.

## 3.2 High-Speed Camera Insights

In this section, the role of the high-speed camera in capturing and analyzing the dynamic behavior of the gas film surrounding the tool is explored. This visual exploration encountered three significant challenges, each of which was addressed to achieve the necessary visual quality for proper footage analysis.

### 3.2.1 Gas Film Visualization

The first challenge was related to the rapidity of gas film formation and breakage, a process occurring within mere milliseconds. In order to visualize the gas film with adequate speed and detail, the frames per second (fps) parameter was investigated. Frame rates spanning from 2000 to 100,000 fps were recorded to determine optimal visual quality. A comparison of images acquired at different frame rates is depicted in Fig. 3.3.
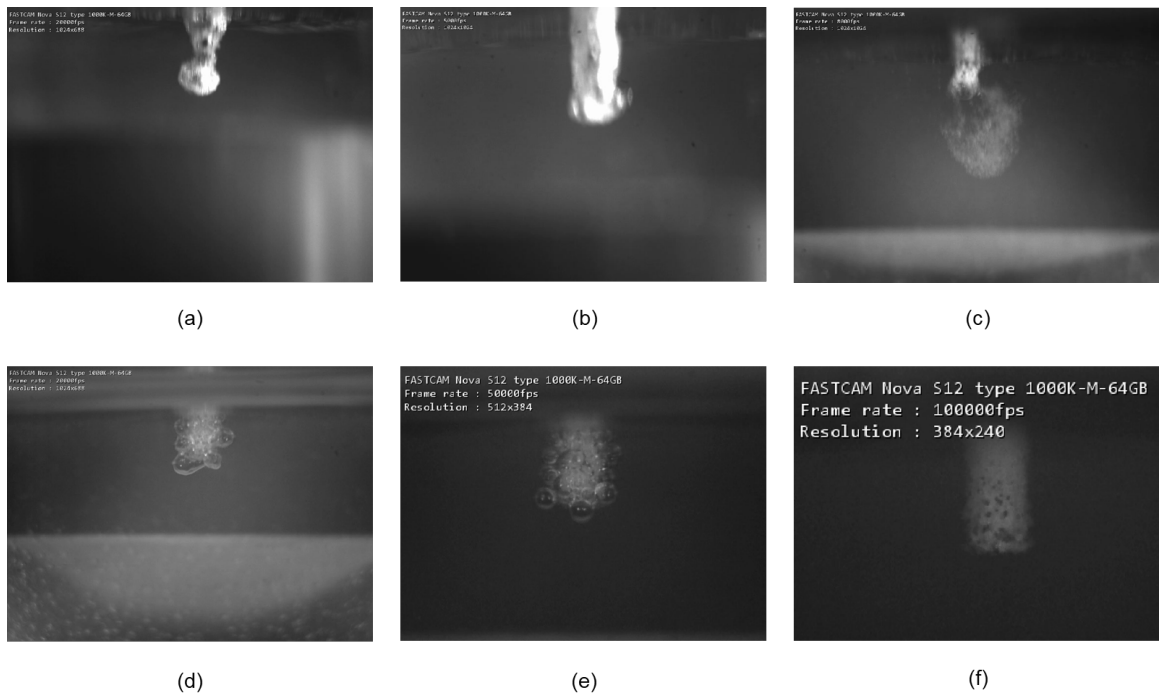


Figure 3.3: Bubble formation around the SACE tool at various frames per second: (a) 2000 fps (b) 5000 fps (c) 10000 fps (d) 20000 fps (e) 50000 fps (f) 100,000 fps.

The increase in fps allowed for the capturing of the gas film with greater detail, as the videos were subsequently slowed down to 30 fps during post-processing to generate videos. However, this increase posed significant hurdles, as the high fps shortened the amount of light that was hitting the camera sensor and creating the image. As a result, the image became much darker. To counteract this, three strategies were implemented. The first approach involved opening the camera aperture, or in other words, adjusting the lens diaphragm to allow more light. Although the allowance of more light improved the lighting conditions, it came at the expense of the quality of focus. Therefore, it was carefully controlled to allow as much light as possible without significantly degrading the image quality during recording.

The second strategy involved the utilization of dedicated camera software, the Photron Fastcam Viewer (PFV4), to enhance the image using look-up tables (LUT). LUT allowed color grading of the images, thus improving image brightness. This was done with the assistance of an experienced professional photographer. The third strategy involved increasing the light sources on the subject. Light-emitting diodes (LED) light sources were the cheapest and easiest way to add more light to the subject; however, the camera was able to capture the light flickering of the LED light. Therefore, halogen light sources were employed to tackle this issue.

Adequate illumination was attained by positioning two Lowel Omni-Light 500W Focus Flood Lights, each equipped with an illuminance of 475 footcandles, at a 45-degree angle with respect to the subject. The trajectory of the light could be characterized as upward and inward, intersecting at the subject to produce overlapping regions of illumination. The angle at which the light sources were positioned had a significant impact on the lighting outcome. When the light sources were placed at an angle, the resulting shadows were more pronounced. Conversely, if the light sources were directly positioned in front of the subject, the shadows were less noticeable. The choice of a 45-degree angle was chosen to create a dynamically balanced lighting effect that enhanced the visibility of the gas film with reduced shadows.

### 3.2.2 Application of Macrophotography

The second challenge stemmed from the subject's small size. With a tool diameter of 500 $\mu$m , focusing on it presented a challenge for normal lenses. To address this concern, an exploration into macrophotography or close-up photography was undertaken. Macrophotography involves capturing extreme close-up images, often of miniature subjects and living organisms like insects, where the subject's size in the photograph surpasses life size. While the usual parameters used in macrophotography, such as shutter speed and resolution, were adjusted in accordance with the field's practices, the camera lens in possession (AF-S DX NIKKOR 18-55mm f/3.5-5.6G VR) was deemed inadequate for this specific photography genre.



(a) (b)
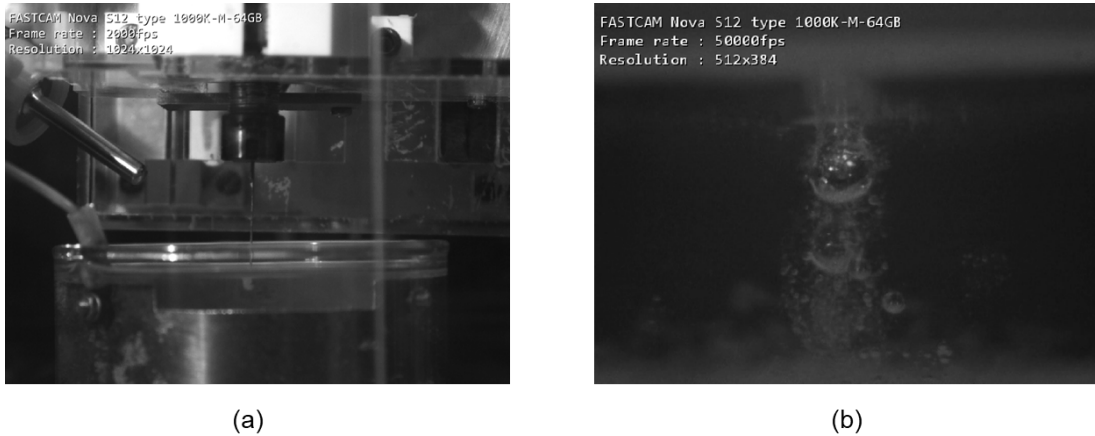
Figure 3.4: Gas film visualization around the SACE machine tool before (a) and after (b) applying macrophotography practices.

Consequently, three extension tubes of varying lengths (12 mm, 20 mm, and 36 mm) were fixed to the camera lens. Extension tubes extend the distance between the lens and the camera's digital sensor, thus bringing the lens closer to the subject and enhancing magnification. The lens's focal length was elongated to 121 mm after the addition of the tubes, and manual focus was employed to fine-tune the focus on the subject. Macrophotography comes with the drawback of an exceptionally narrow depth of field. However, this limitation was addressed by making physical

adjustments to the gas film setup, allowing the lens to be safely positioned as closely as possible to the subject, thus addressing the challenge of depth of field. The effect of the macrophotography practices can be seen in Fig. 3.4.

### 3.2.3    Recording Procedures and Camera Settings

To start recording, the Nova S12 Fast Cam was securely mounted on a tripod positioned just a few centimeters ($<15\ cm$) away from the the tool positioned at the center of the processing cell. The camera was manually adjusted to focus on both the tool and forming gas bubbles. During the recording phase, the camera was programmed to record durations lasting 0.5 seconds. An overview of the camera configurations selected in this study to obtain high quality visuals while effectively matching the process rapidity is presented in Table 3.1 and a schematic of the setup is shown in Fig. 3.5.

The utilization of a high-speed camera for this analysis facilitated the visualization of the gas film under various conditions, effectively providing valuable insights that could be aligned with the corresponding recorded current signal data. The third challenge encountered in employing the high-speed camera related to synchronizing the captured footage with the current signal plots recorded on the oscilloscope. This challenge was met by implementing a MATLAB algorithm to synchronize the footage and signal plots.

Table 3.1 High speed camera settings.

| Settings | Values |
| --- | --- |
| Frame rate per second | 50,000 fps |
| Shutter speed | 1/100000 sec |
| Resolution | 512 x 384 |
| Frame count | 25,000 |
| Duration | 0.5 sec |
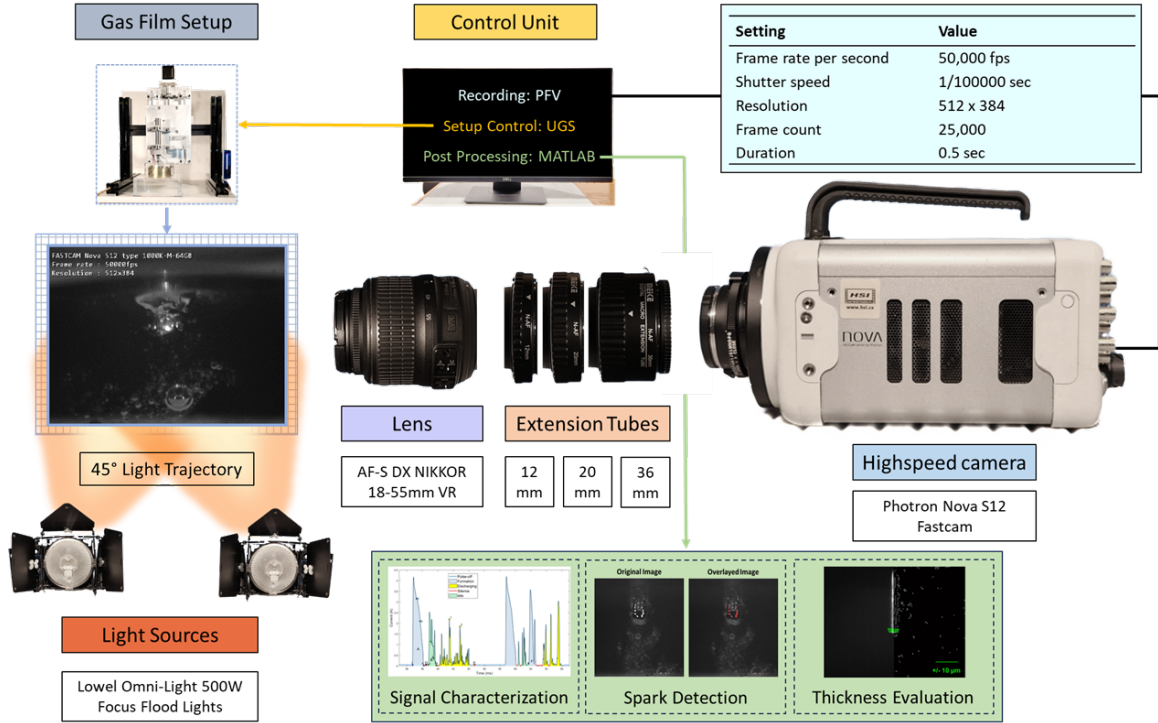
Figure 3.5: High speed camera set-up for visual analysis of the gas film around the SACE machine tool.

## 3.3 Control methods

In the attempt of achieving precise and reproducible results in the following experimental framework, various aspects are considered in preparation and execution of the experiments. Control variables, including properties of the electrolyte, as well as temperature monitoring, are examined.

### 3.3.1 Electrolyte

Accurate monitoring of the electrolytes used in the experiments was crucial to ensure the repeatability of the results and mitigate any potential external influence of the electrolyte on the process. The following section discusses the methodologies employed in preparing the electrolyte to meet specified criteria such as concentration, density, viscosity, and conductivity.

*Electrolyte concentration*

The chemicals utilized in this study consisted of KOH and NaOH pellets. The chemical pellets were weighted with high accuracy using a balance with a precision of 0.0001 grams. Subsequently, the chemicals were mixed with deionized (DI) water in a beaker to achieve the required total weight, corresponding to the desired concentration. To attain the necessary concentration of the electrolyte, a conversion based on Equation (3.1) was applied. It should be noted that the chemicals, upon mixing with water, release potentially harmful gases and elevate the water temperature, resulting in water evaporation. To address the issue of emitted gases, the mixing process was conducted within a vacuum box. To control water evaporation, thick foil sheets were employed to cover the beaker. Furthermore, the electrolyte was reweighed after a 24-hour period, and any decrease in total weight was rectified by adding water as necessary.

$$Weight\ precentage\ (Wt\%) = \frac{Pellets\ weight\ (g)}{Pellets\ weight\ (g) + DI\ Water\ weight\,(g)} \quad (3.1)$$

Throughout the experiments, the concentration of the electrolyte was monitored by assessing the electrolyte density using a micropipette and a microscale for measurements. To assess the accuracy of the density measurements, the instruments were calibrated using both water and a known-density acetic acid solution at various volumes (Ranging from 700 to 900 µL). The determined error was within the range of $+/-$ 0.04 g/ml. The data collected was then compared with the densities provided in the CRC Handbook of Chemistry and Physics, 95th edition [80]. A graph showing density change throughout 200 minutes of experiments is shown in Fig. 3.6.
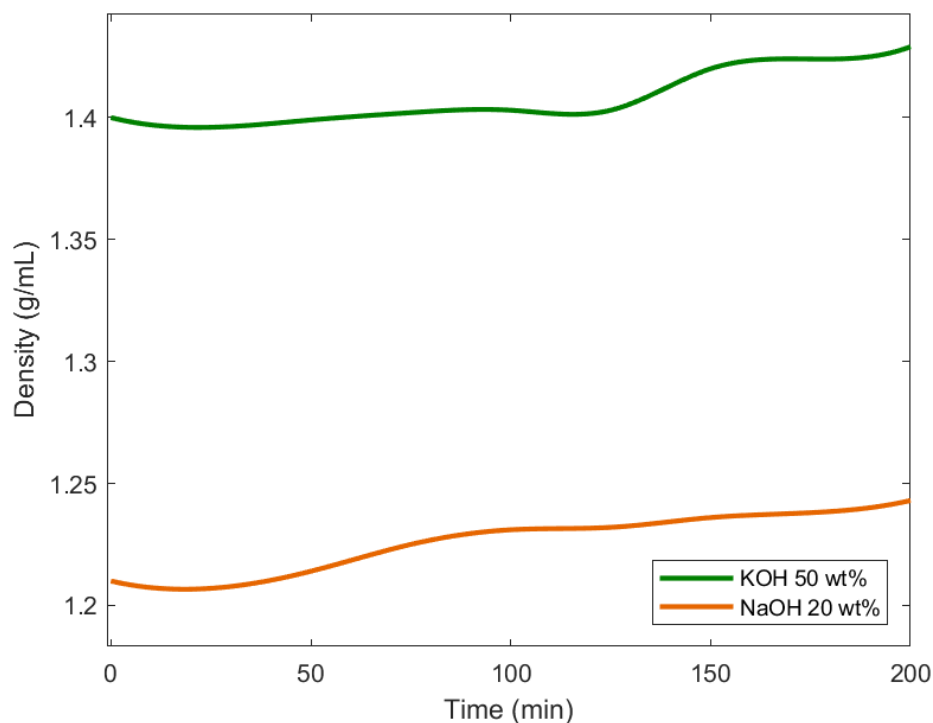
Figure 3.6: Density changes throughout 200 minutes of experimentation.

It is worth noting that an alternative method for monitoring the electrolytes in the experiments involves measuring the pH level of the studied electrolytes and comparing it to the theoretical values. However, this approach was not further investigated due to the unavailability of the necessary equipment.

*Electrolyte viscosity*

In this study, the electrolyte's viscosity was assessed through experimental means and subsequently compared with the theoretical values obtained from the OxyChem caustic soda and caustic potash handbooks. The experimental determination of viscosities involved the following procedures:

1. Initial preparation of solutions in small quantities, targeting viscosities that were theoretically close.

2. Acquiring reference values for DI water, including literature-based viscosity

($n_1$), density ($d_1$), and runoff time ($t_1$), where runoff time represents the duration for a fluid to flow through a viscometer under the influence of gravity.

3. Determining the density ($d_2$) and runoff time ($t_2$) of the electrolyte solution under examination using an Ostwald viscometer.

4. Applying the conversion (Equation 3.2) to calculate viscosity:

$$n_2 = n_1 \left( \frac{d_2 t_2}{d_1 t_1} \right) \tag{3.2}$$

The measurements were done with three repetitions and their average was the value used in this study. To engineer solutions to the required viscosities the following Equations 3.3 and 3.4 were used to change the electrolyte concentration:

$$Increase\ viscosity: \quad m_1 = 0 \ ; \ m_2 = \frac{m(x_2 - x_1)}{(1 - x_2)} \tag{3.3}$$

$$Decrease\ viscosity: \quad m_1 = \frac{m(x_1 - x_2)}{x_2} \ ; \ m_2 = 0 \tag{3.4}$$

Where,

$m =$ Original solution mass (g)

$x_1 =$ Original concentration

$x_2 =$ Required concentration

$m_2 =$ DI water (g)

$m_2 =$ Chemical pellets (g)

*Electrolyte conductivity*

The conductivity of the electrolytes under study were evaluated using a conductivity meter. Subsequently, a comparison was drawn between the experimental conductivity values and the theoretical conductivity of the corresponding electrolytes, which

was calculated employing Equations 3.5 and 3.6 [81, 82]. The specific correlation parameters $(K1 - K8)$ used are listed in Table 3.2.

$$\sigma_{KOH} = K_1.\,(100.\omega_{KOH}) + K_2.T + K_3.T^2 + K_4.T.\,(100.\omega_{KOH})$$
$$+ K_5.\,T^2.\,(100.\omega_{KOH})^{k_6} + K_7.\frac{T}{(100.\omega_{KOH})} + K_8.\frac{(100.\omega_{KOH})}{T} \tag{3.5}$$

$$\sigma_{NaOH} = K_1 + K_2.\theta + K_3.\omega^3_{NaOH} + K_4.\omega^2_{NaOH} + K_5.\omega_{NaOH} \tag{3.6}$$

Where,

$T$ = Electrolyte temperature $(K)$

$\omega_{KOH}$ = KOH mass fraction $(Wt\%)$

$\theta$ = Electrolyte temperature $(°C)$

$\omega_{NaOH}$ = NaOH mass fraction $(Wt\%)$

Table 3.2 Parameters for calculating the specific electrolyte conductivity of KOH and NaOH electrolytes by Equations 3.5 and 3.6.

| Parameter | Equation (3.5) [56] | Unit | Equation (3.6) [51] | Unit |
|---|---|---|---|---|
| $K_1$ | 27.9844803 | S m$^{-1}$ | $-45.7$ | S m$^{-1}$ |
| $K_2$ | $-0.924129482$ | S m$^{-1}$ K$^{-1}$ | 1.02 | S m$^{-1}$ °C$^{-1}$ |
| $K_3$ | $-0.0149660371$ | S m$^{-1}$ K$^{-2}$ | 3200 | S m$^{-1}$ |
| $K_4$ | $-0.0905209551$ | S m$^{-1}$ K$^{-1}$ | $-2990$ | S m$^{-1}$ |
| $K_5$ | $0.0114933252$ | S m$^{-1}$ K$^{-2}$ | 784 | S m$^{-1}$ |
| $K_6$ | 0.1765 | $-$ | $-$ | $-$ |
| $K_7$ | 6.96648518 | S m$^{-1}$ K$^{-1}$ | $-$ | $-$ |
| $K_8$ | $-2898.15658$ | S K m$^{-1}$ | $-$ | $-$ |

A summary of the calculated specific conductivities for the NaOH and KOH electrolytes employed in this study at temperatures of 25°C (Room temperature) and 50°C is shown in Fig. 3.7.
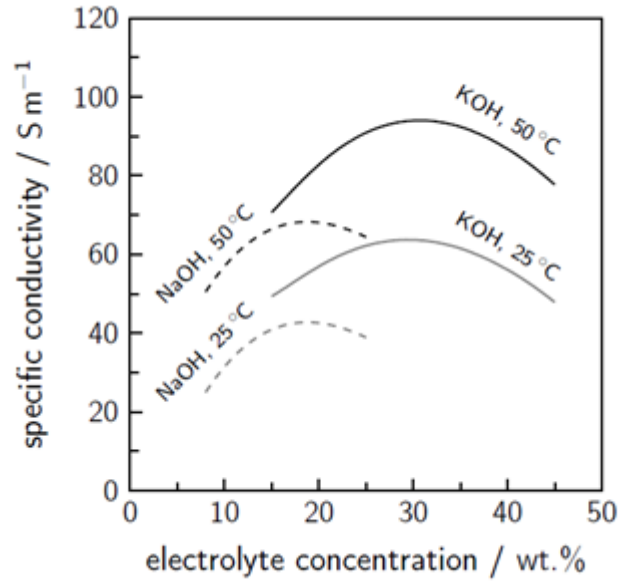
Figure 3.7: Calculated specific electrolyte conductivity for different NaOH and KOH electrolyte concentrations used in the study at different temperatures.

## 3.3.2 Temperature monitor

An effort was made to monitor the temperature within the tool-gas film region in order to track temperature change during the experiments. Four different approaches were employed to monitor the temperature, each accompanied by its own limitations.

1. *Thermal Camera Approach:* This approach involved using a thermal camera to generate a thermal map of the designated areas. Fluke Canada provided a demonstration thermal camera and a thermometer, detailed in the following approach, for testing purposes. However, the thermal camera faced challenges in accurately measuring temperatures below the surface due to infrared wavelength obstruction caused by the electrolyte.

2. *Infrared Thermometer with Laser Focus:* This method utilized an infrared thermometer equipped with a high-focus laser to measure the temperature around the tool. Despite efforts to enhance its precision by adding a high-resolution lens, the presence of the electrolyte posed significant difficulties. Focusing on

the small tool ($\Phi$ 500$\mu$m) proved to be a challenge due to the obstructive nature of the electrolyte, impacting the thermometer's effectiveness.

3. *Thermocouple Implementation:* This approach involved implementing a thermocouple positioned in proximity to the tool beneath the electrolyte. However, this method was heavily influenced by the ion mobility within the electrolyte during the experiments. The thermocouple readings were observed to be impacted by the SACE process, as illustrated by the mirrored signals between the thermocouple and the SACE process recorded current signals (Fig. 3.8).

4. *Mercury-in-Glass Thermometer Placement:* A traditional mercury-in-glass thermometer was placed at a distance of 5 mm from the tool. This method allowed for the tracking of temperature variations. However, the low sampling rate of the conventional thermometer limited its ability to provide real-time and accurate temperature measurements.
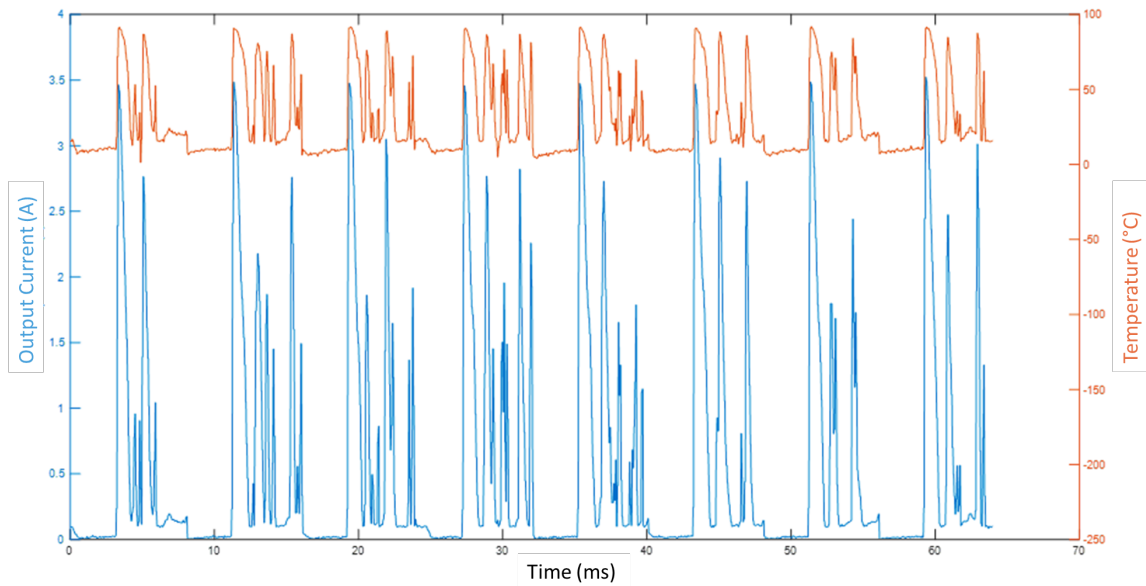


Figure 3.8: The SACE process effect on the application of a thermocouple to monitor the temperature change around the tool electrode. Orange: Thermocouple recorded signals; Blue: SACE process recorded current signals.

Consequently, the temperature monitoring approach was modified to focus solely on bulk temperature readings for data collection purposes, conducted at a reference bulk temperature of 50°C during the experiments.

## 3.4    Design of experiments

In this section, the role of experimental design is discussed, with an emphasis on the incorporation of randomization, replication, and blocking techniques to ensure experiment repeatability and the derivation of valid conclusions. The implementation of these methods was carried out using Design Expert (DX-13) software that facilitated a comprehensive statistical analysis.

### 3.4.1    Factorial design integration

The design of experiments, incorporating crucial elements such as randomization, replication, and blocking techniques, holds significant importance in ensuring experiment repeatability and drawing valid conclusions. This study employed two distinct experimental designs, with the foremost emphasis on the application of a factorial design. Factorial designs evaluate multiple factors, or independent variables, each with various discrete levels. This methodology facilitated the exploration of all potential combinations of factor levels, enabling the identification of main effects caused by changes in these factors and interactions between them. The primary aim was to determine the impact of main input factors and interactions among them. Main effects represent the changes resulting from altering the factor levels, while interactions indicate the differences in responses between levels of one factor that are not consistent across all levels of another factor.

The second design used was a factorial design with a split-plot subtype. Split-plot designs were employed in investigations that included the use of multiple electrolytes. Electrolytes were hard to change factors when conducting experiments, as changing the electrolyte required resetting the setup and involved cleaning procedures when

changing electrolytes, thus affecting the randomization in the experiments. The split-plot design basically divided the experiments into units of different sizes to accommodate hard-to-change factors. A whole-plot and split plot in split-plot designs divided the errors according to the following general mixed-model formulation, Equation (3.7). Therefore, accounting for errors in both the whole-plot and the split-plot.

$$Y_{ijk} = \mu + a_i + \eta_{k(i)} + \beta_j + (a\beta)_{ij} + \varepsilon_{k(ij)} \tag{3.7}$$

Where,

$Y_{ijk}$ = Response factor for a specific run with unique input factors.

$\mu$ = Overall response variable mean

$a_i$ = Fixed effect of the hard-to-change factor

$\eta_{k(i)}$ = Whole-plot error

$\beta_j$ = Fixed effect of the easy-to-change factor

$(a\beta)_{ij}$ = Interaction between the input factors

$_{k(ij)}$ = Split-plot error

## 3.4.2 Statistical Analysis using Design Expert (DX-13)

The Design Expert (DX-13) software was utilized to apply the mentioned models and implement proper randomization. The response variables of interest were categorized within the software and evaluated individually. To validate the design models, a statistical analysis was conducted for each experiment. Initially, the residuals vs. runs plot and the normal plot of residuals were examined. The normal plot of residuals compared observed residuals, representing the disparities between observed and predicted values, against expected residuals assuming a normal distribution. A close alignment of observed residuals with the diagonal reference line suggested adherence to a normal distribution. Additionally, the residuals vs. runs plot was used to assess the randomness and independence of residuals by contrasting residuals on the y-axis

with the sequence of observations or runs on the x-axis. If these plots exhibited a random distribution around the zero line, devoid of noticeable patterns or trends, it indicated compliance with the assumptions of randomness and independence. Contrarily, deviations suggested the impact of external factors or the presence of significant outliers requiring further adjustments. The plots and their corresponding findings are presented in Section 4.3.

The Box-Cox transformation, a diagnostic tool, was used to shape non-normal data distributions into a more normalized form. Subsequently, an analysis of variance (ANOVA) was performed in order to effectively evaluate the effect of the input parameters on the response variables. A high F-value indicated a low probability of results being attributable to random fluctuations. Model terms with p-values below 0.05 denoted significance regarding the impact of input variables on output variables. The coefficient of determination (r-square) and related metrics, such as adjusted r-squared, quantify the extent to which the independent variables account for the variance in the dependent variables. Additional valuable graphs for analysis included box-plot graphs, model contours, and numerical optimization ramps.

## 3.5    Signal design

As previously mentioned in Section 2.3.3, different signal shapes applied in SACE significantly influence gas film formation and breakage, ultimately impacting the stability and repeatability of the process. When a DC voltage higher than the critical voltage ($V_{cr}$) is used in SACE, continuous gas film formation occurs, leading to persistent sparking, overheating, and degradation of machining quality. In contrast, using pulse voltage with periodic interruptions allows flushing in the machining zone, prevents excessive heating and improves the machining efficiency and quality.

The proposed signals utilized in this study exhibit a behavior similar to pulse signals. They exceed the critical voltage at the peaks to facilitate discharging and fall slightly below the critical voltage at the valleys to enable tool cool-down. Unlike

pulse signals, which result in complete gas film breakage at low voltages, the designed signals maintain gas film formation without complete breakage by only marginally dropping below the critical voltage. The extent of the signal's deviation from the critical voltage is controlled by the applied low voltage, mimicking pulse signals' on-time and off-time characteristics. A comparison of the proposed signals and pulse signal's on-time and off-time characteristics is shown in Fig. 3.9. Additionally, the rising and falling edges of the signal can enable a gradual increase and decrease of the applied voltage.
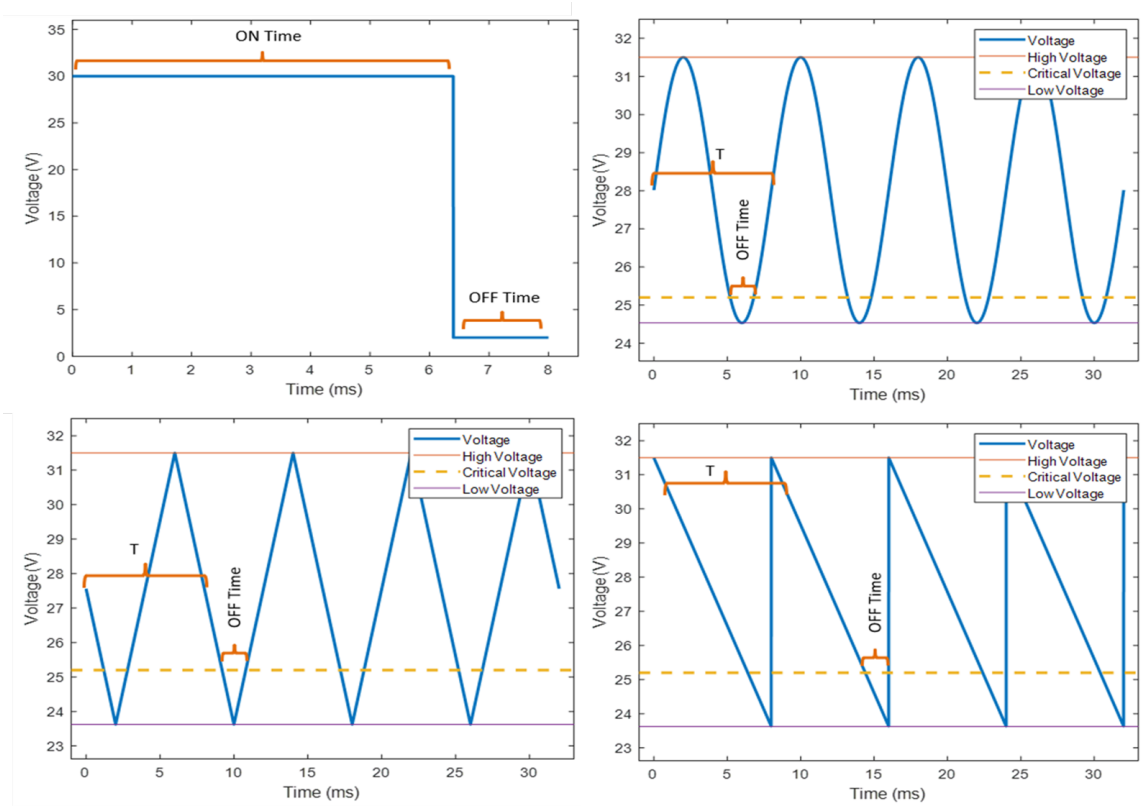


Figure 3.9: On-time and Off-time characteristics for pulsed, sinusoidal, triangle and ramp signal shapes.

To facilitate a comparative analysis between the proposed signals, shown in Fig. 3.9, and pulse signals in this study, similar behaving signals were generated. Pulse voltage exhibits specific characteristics such as high voltage ($V_{high}$), low voltage ($V_{low}$), period ($T$), and duty cycle ($dc$).

- $V_{high}$: The high voltage carries greater significance than the low voltage and affects the duration of the gas film formation time. The high voltage was determined as a function of the critical voltage for each respective electrolyte. The critical voltage varies depending on properties such as the conductivity and viscosity of the selected electrolyte. Therefore, adjusting the high voltage to match the specific electrolyte in use offers a fair basis for comparison than assigning fixed values. This emphasizes the importance of considering electrolyte effects alongside the effects of electrical inputs in this study, as electrolyte properties directly influence the electrical inputs.

- $T$ and $dc$: The period and duty cycle determine the duration when the voltage exceeds the critical voltage, creating favorable conditions for gas film formation, referred to as the on-time ($T_{on}$) in this study, and expressed as a percentage of the period. In pulse voltage, the on-time is equal to the duty cycle. For comparing the effect of different signal shapes on the gas film properties, variations incurred due to the properties of the signals like the period, duty and on-time shall be ruled out. Therefore, the signals were generated to have similar $V_{high}$, $T_{on}$, and $T$. $T_{on}$ was determined by aligning $V_{low}$ for each signal shape using Equations (3.8) and (3.9).

$$Sinusoidal\ Signals: \quad V_{low} = \frac{2V_{cr} - (1 + \sin(a))\,V_{high}}{1 - \sin(a)} \tag{3.8}$$

$$Triangle\ \&Ramp\ Signals: V_{low} = \frac{V_{cr} - (1 - dc)\,V_{high}}{dc} \tag{3.9}$$

Where,

$V_{low}$ = Low voltage

$V_{cr}$ = Critical voltage

$\alpha = (0.5 + T_{on}) \times \pi$

$V_{high}$ = High voltage

$dc$ = Duty cycle

$T_{on}$ = On-time equivalent to the duty cycle

For each electrolyte utilized in this study, the critical voltage was determined through experimental means. A ramp signal with a lengthy period (500 ms and above) was applied, and the critical voltage was subsequently identified by pinpointing the corresponding drop in current observed on the current-time plot. This approach aligns with the methods outlined in Section 2.3. An average of five analyzed signals was taken to determine the critical voltage. Table 3.3 presents a summary of the experimentally determined critical voltages.

Table 3.3 Critical voltages of the electrolytes used in the study.

| Electrolyte | Concentration ($wt\%$) | Critical voltage ($V$) |
|---|---|---|
| NaOH | 20 | 27.6 |
| NaOH | 30 | 26.1 |
| KOH | 45 | 22.2 |
| KOH | 50 | 22.4 |

## 3.6 Analysis methods

In this section, the analysis methods employed in this study are discussed. These methods include visual analysis and signal processing, with each offering unique insights into the intricate dynamics of SACE.

### 3.6.1 Visual analysis

*Signal characterization*

To analyze the gas film, corresponding SACE current signals ($I(t)$) were recorded alongside camera footage during the experiment and were synchronized using MAT-

LAB. The synchronization process involved three key steps. First, timing details were extracted from the video recording, including frame rate, start time, and end time. Second, timing details from the SACE current signal dataset, like sampling rate and start time, were extracted. Lastly, with the timing information in hand, the synchronization algorithm was executed by aligning the SACE current signal dataset's timestamps with those of the video recording. This was achieved through resampling the current signal dataset next to the video frame rate and adjusting timestamps using interpolation. A flowchart of the algorithm is shown in Fig. 3.10.
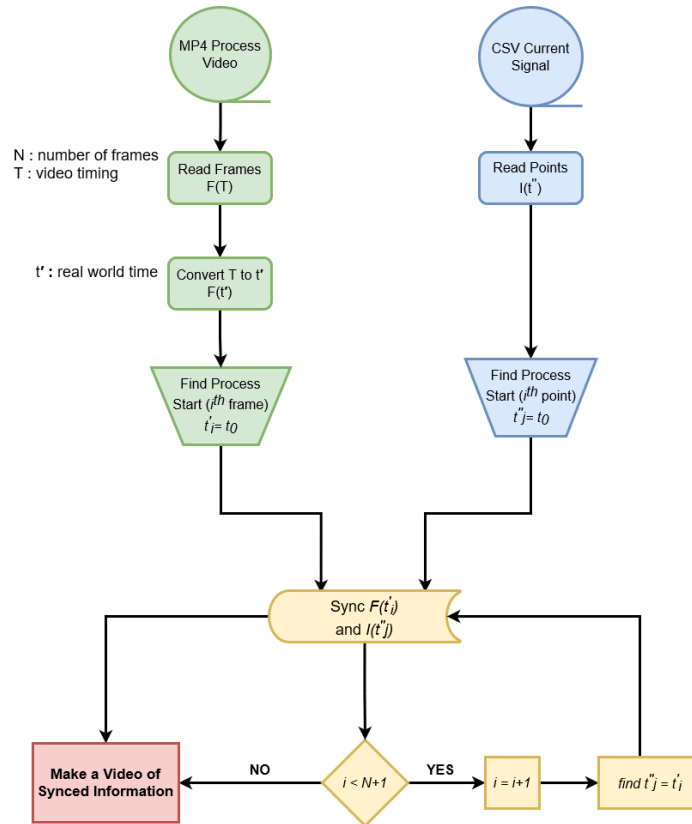


Figure 3.10: Flowchart of the synchronization code used in the visual analysis.

After successfully synchronizing the current data with the recorded footage, another MATLAB code was utilized to perform image segmentation on frames of interest. The image segmentation approach aimed to distinguish between discharges and bubbling observed in the images, establishing an accurate correlation between the

45

visual cues and the patterns of current observed in the current-time plots. The segmentation procedure started by converting the frames to grayscale, and a threshold was selected to differentiate white regions from other areas. The threshold was then applied on the grayscale image, resulting in the creation of binary images. Following this, two figures were generated: the segmented white regions, and an overlay of white regions on the original image in red. The overlay allowed for the visualization of spark locations within the original image. The current data was then classified into four distinct current regions: gas film formation, discharging, silence, and idle regions. Fig. 3.11 shows the categorized process current regions, and the corresponding frames.
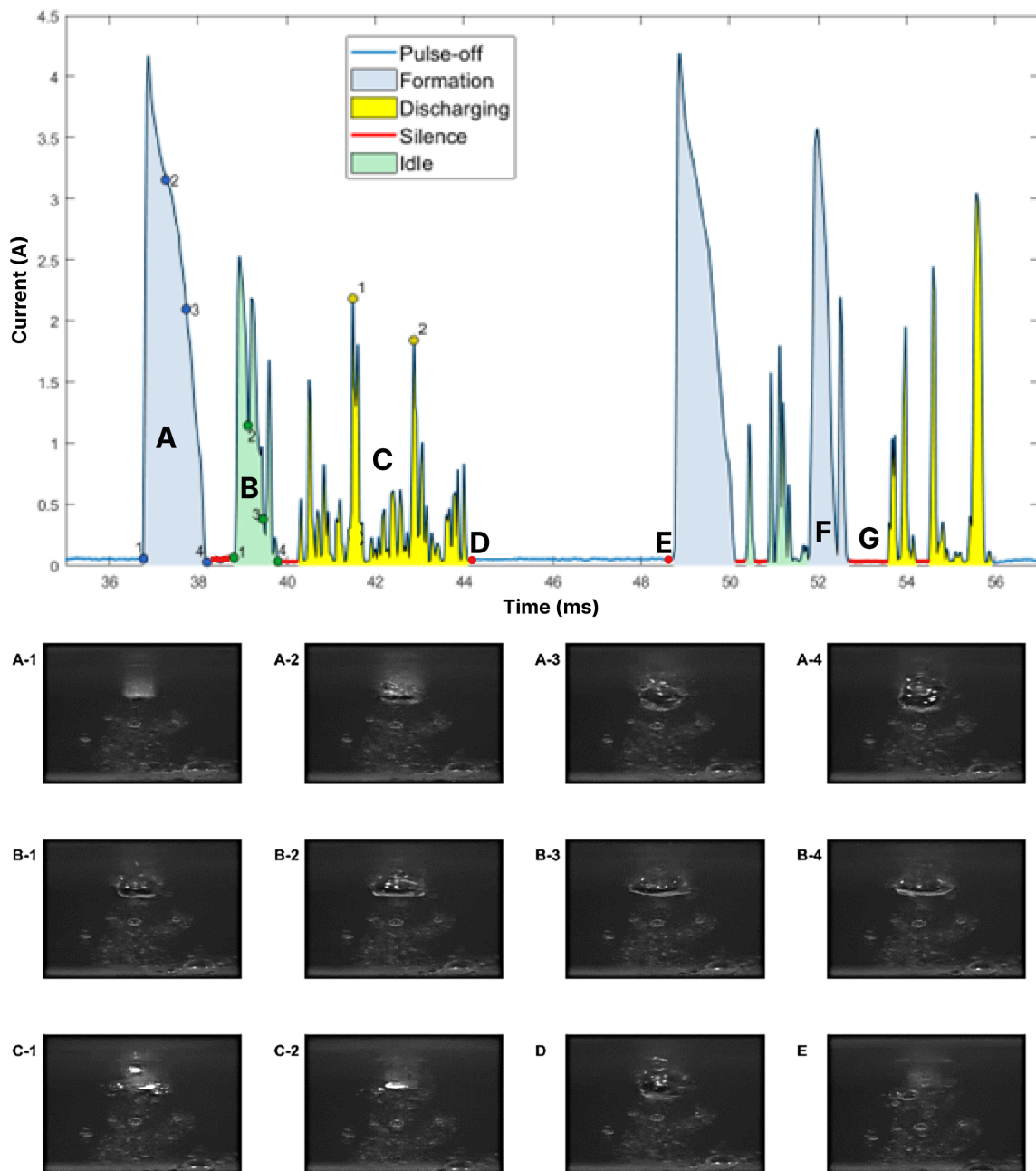
Figure 3.11: SACE current signal acquired at a sampling rate of 62.5 KS/s synchronized with corresponding video frames captured at 50,000 fps. (KOH 50 wt%, Pulse signal, High voltage 30 V and DC 60%)

*(i) Gas film formation:* As observed in Fig. 3.11 in regions A and F, a gas film is formed and this is accompanied by a rapid surge in current. During the pulse-off time (See Figure 3.11, region starting at point D and ending at point E), the gas film is intentionally broken. When the voltage is turned on again (pulse-on), this results in

the appearance of a formation signal, signifying a new phase in gas film formation.

*(ii) Discharging:* As observed in Fig. 3.11, region C, the current fluctuates with a rapid spike during the discharging phase. Sparks are generated through the gas film channels around the tool as seen in the corresponding images. The sparking phenomena were confirmed using the image segmentation technique as illustrated in Fig. 3.12.
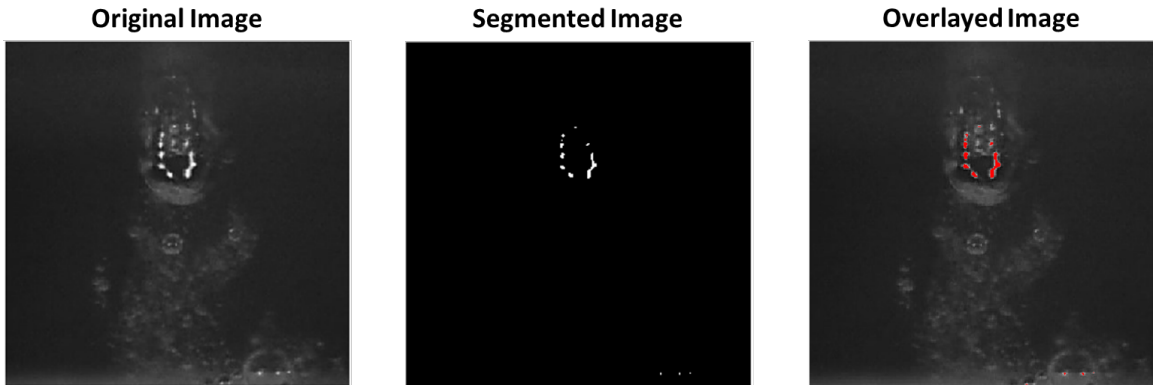


Figure 3.12: Application of image segmentation technique for spark detection in the SACE process.

*(iii) Silence:* As observed in Fig. 3.11 in region G the current is near-zero, and that represents the spans between discharging where the gas film remains intact

*(iv) Idle:* As observed in Fig. 3.11 in region B, fluctuations reminiscent of discharge spikes were noted on the plot. However, in these regions, no visible sparks were identified in the corresponding video frames. Rather, the gas film rebuilds itself accompanied with turbulence (bubble detachment from the film), as depicted in Fig. 3.13. Although the gas film resists breaking, it's not stable enough, leading to a bubble escape and leakage of current. This current leakage disrupts the balance of the electric field within the gas film.
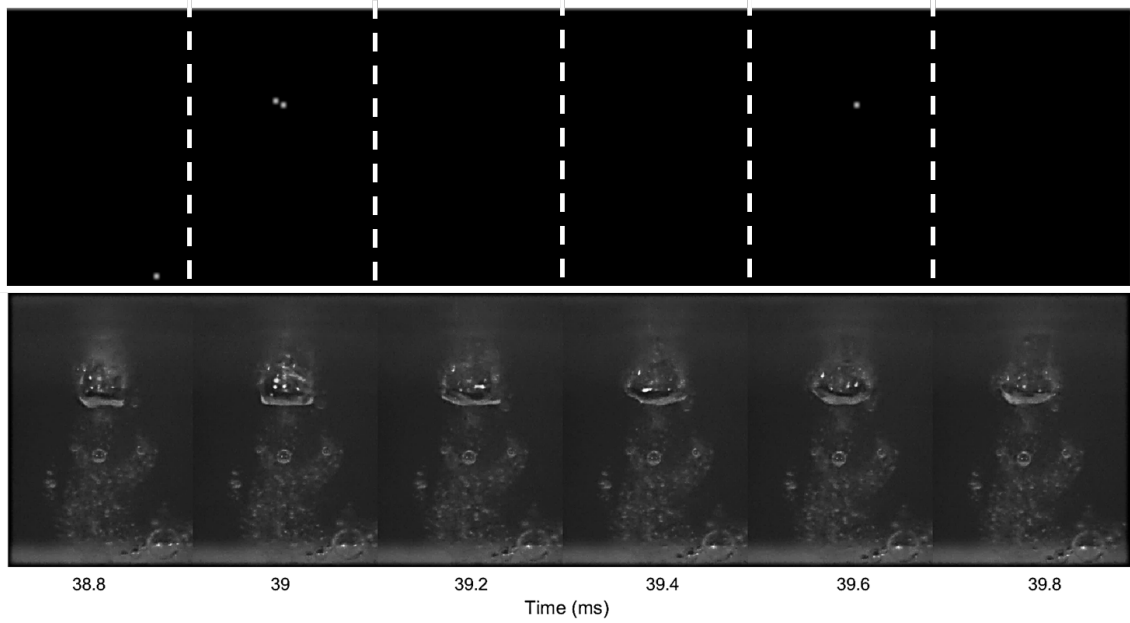
Figure 3.13: Idle region video frames. No sparks are detected as observed in the corresponding segmented images.

*Gas film thickness evaluation*

The gas film thickness was evaluated by utilizing a high-speed camera to capture the SACE process in action under predetermined conditions. Subsequently, the recorded footage underwent image processing through a MATLAB algorithm, which converted the images into grayscale and performed edge detection. These edge-detected images were then used to facilitate the visualization of gas film edges for measurement purposes. The measurements were assessed by counting the number of pixels between two specified points. Following this, the pixel measurements were converted into micrometers. This conversion was accomplished through calibrating the pixel-per-micrometer scale factor for each recorded footage, which was determined by measuring a known object (The tool-electrode diameter).

After finishing the calibration stage, three measurements were acquired for three separate occurrences of the gas film within the recorded footage. The average of these three measurements was regarded as the gas film thickness (Equation 3.10). In this

study, the thickness is defined as the edge-to-edge distance of the gas film's side profile. Following the measurements on the edge-detected image, these measurements are mirrored onto the original image with corresponding coordinates, which are displayed alongside lines and text annotations. Fig. 3.14 illustrates the application of edge detection and measurement methods on the original footage extracted from the high-speed camera.

$$t = \frac{1}{n} \sum_{k=1}^{n} \left( \frac{T_k - \emptyset_t}{2} \right) \tag{3.10}$$

Where,

$t$ = Gas film thickness

$T_k$ = n$^{th}$ measurement value

$\emptyset_t$ = Tool diameter (500 µm)
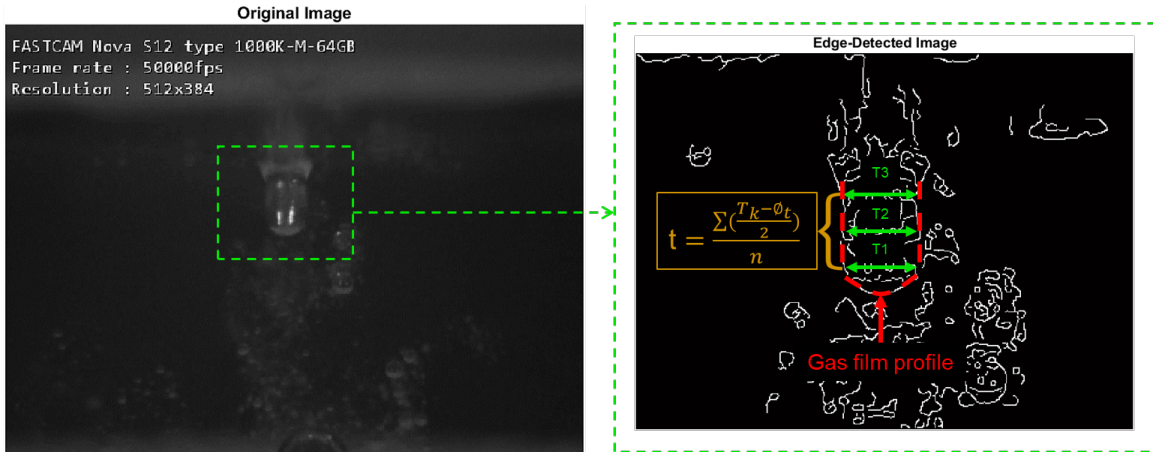


Figure 3.14: Application of MATLAB-based image processing method to captured high-speed camera footage.

## 3.6.2 Signal processing

Upon acquiring the signal data recorded on the oscilloscope, a neural network signal processing technique, developed by Seyedi Sahebari et al. [83], was employed to

analyze the signals and identify the parameters of interest. The data was categorized as mentioned in Section 3.6.1: In general sharp current spikes, lasting around 1-2 millisecond, indicate gas film formation. A current approaching zero indicates the presence of a fully formed gas film. Rapid current spikes suggest discharges. Other regions in such as the silent and idle regions were also incorporated. This categorization was subsequently validated using the high-speed camera, and the plots were continuously annotated to enhance the accuracy of the artificial neural network. Three response outputs were selected for comparing the recorded current plots, as shown in Fig. 3.15.
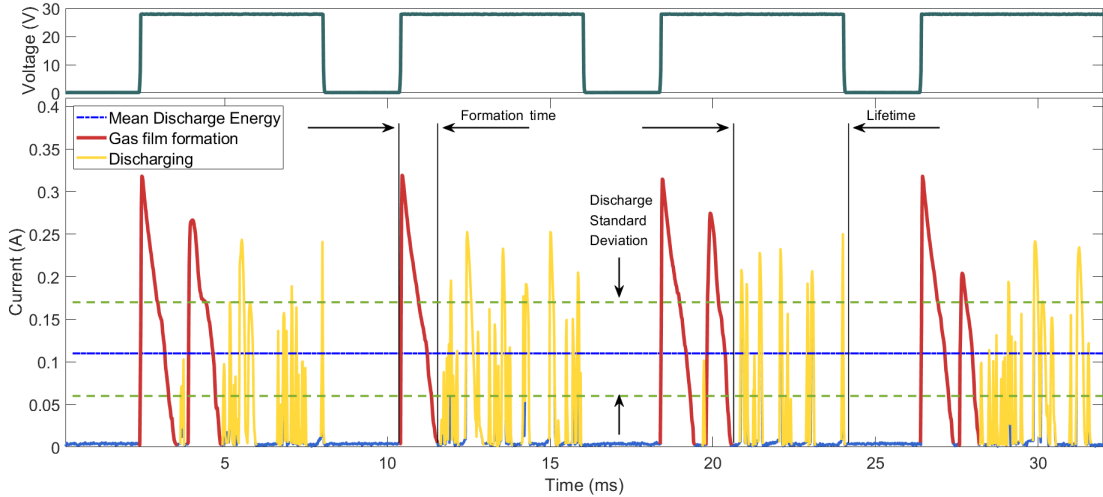


Figure 3.15: Current-time plot of the SACE process and its corresponding voltage-time plot; The three response variables employed in signal processing: Gas film lifetime, mean discharge energy, discharge current standard deviation.

The first output is the average gas film lifetime (ms), representing the duration when the gas film is fully formed without any interruptions such as gas film breakage. A signal with a longer gas film lifetime indicates the presence of a stable and robust gas film with minimal turbulence. The second response output used in this evaluation is the discharge mean energy, calculated using Equation 3.11:

$$E = V \times I_{dis} \times t \tag{3.11}$$

51

Where,

$E$ = Energy of discharge (J)

$V$ = Critical voltage (V)

$I_{dis}$ = Mean discharge current (A)

$t$ = Mean discharge interval (t)

Calculation of mean discharge current and mean discharge interval are given in Equations 3.12 and 3.13 respectively.

$$I_{dis} = \frac{\sum_1^k I_{disk}}{n} \tag{3.12}$$

$$t = \frac{\sum_1^k t_k}{n} \tag{3.13}$$

Where,

$I_{disk}$ = discharge current value for kth discharge peak

$t_k$ = discharge current time interval for kth discharge peak

$n$ = total number of peaks in the current data

In SACE, gas film stability is determined by its capacity to retain its shape during discharging activity, with variations in shape leading to changes in thickness [86]. Thin gas films demand less energy for breakage, making signals with low discharge mean energy preferable. The third evaluated output is the standard deviation of the discharge current. Gas film stability refers to the gas film's capacity to retain its form during the discharging process. As the shape of the gas film fluctuates, so does its thickness, consequently affecting the energy needed to break the film. A decreased standard deviation of the discharge current corresponds to enhanced gas film stability. The histogram plot of discharge current demonstrates the distribution

of discharge current values, thereby indicating the fluctuation in the gas film's shape, as demonstrated by Kolhekar et al. [84] and depicted in Fig. 3.16.
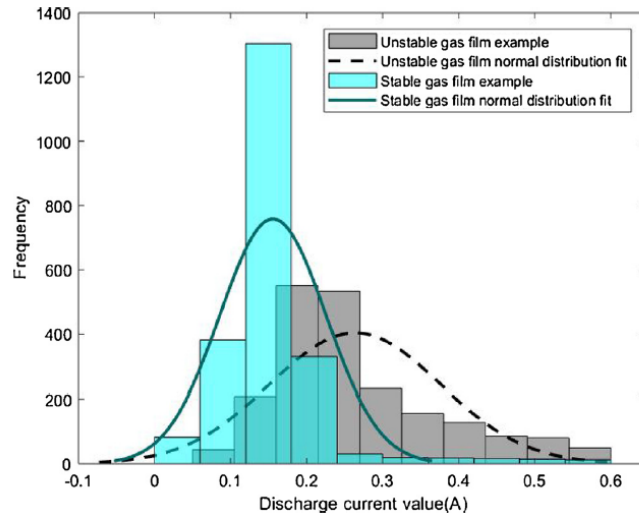


Figure 3.16: Standard deviation of discharge current data as an indicator of gas film stability. Referenced from [84].

# Chapter 4

# Characterization Experiments

To examine the effect of applying various signals on gas film stability under multiple conditions, a split-plot factorial design was employed to design the experimental plot. The process parameters and their corresponding levels used to formulate the experimental matrix layout, are presented in Table 4.1.

Table 4.1 Process parameters and their levels.

| Process Parameters | | Level & Units | | | |
|---|---|---|---|---|---|
| Variable process parameters | | Level 1 | Level 2 | Level 3 | Level 4 |
| 1 | Electrolyte type, A | NaOH 20 wt% | NaOH 30 wt% | KOH 45 wt% | KOH 50 wt% |
| 2 | Applied Signal, B | Sinusoidal | Triangle | Ramp | Pulse |
| 3 | Period, C | 6 | 8 | 10 | - |
| 4 | On-time, D | 70 | 80 | 90 | - |
| Constant process parameters | | | | | |
| 5 | Immersion Depth | 1 mm | | | |
| 6 | Applied voltage | $1.24 \times (U_{crit})$ | | | |
| 7 | Tool diameter | 500 $\mu$m | | | |
| 8 | Tool material | Stainless-steel | | | |
| 9 | Tool Geometry | Cylindrical | | | |
| 10 | Bulk temperature | 50° C | | | |

To assess the influence of electrolyte on the investigation, two levels of KOH and NaOH electrolytes were selected, falling within the range established in existing literature. Table 4.2 presents the electrolytes utilized in this study, along with their corresponding properties at 25 and 50 degrees Celsius.

Table 4.2 Electrolyte properties with respect to the concentration and temperature.

| Electrolyte | Conductivity (25°C) μS/cm | Viscosity (25°C) Cp | Conductivity (50°C) μS/cm | Viscosity (50°C) Cp |
|---|---|---|---|---|
| NaOH 20 wt% | 426 | 3.8 | 681 | 2 |
| NaOH 30 wt% | 323 | 13 | 578 | 4.3 |
| KOH 45 wt% | 474 | 3.6 | 778.2 | 2.1 |
| KOH 50 wt% | 373 | 4.5 | 657.5 | 2.8 |

In terms of the applied signals, shown in Fig. 4.1, pulse signal served as the baseline against the three novel signals. Sinusoidal and triangular signals were utilized to explore the difference between employing signals with smooth and flat edges. The selection of the ramp signal aimed to study the effect of applying an asymmetrical shape in contrast to the symmetrical shapes of the sinusoidal and triangular signals.
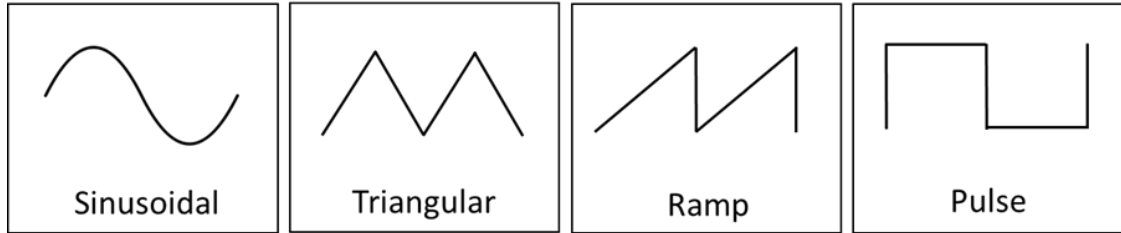


Figure 4.1: The four signals investigated in the characterization experiment.

Three varying levels of periods and on-time were selected within the literature-defined limits to identify the suitable levels in relation to the studied signals. In this study, the tool properties and immersion depth were blocked, as they were not within the scope of interest. The applied voltage was devised as a function of the critical voltage, which varies based on the employed electrolyte. Experimental runs were conducted at a bulk temperature of 50 degrees Celsius, a temperature favorable to discharge activity at an acceptable rate. Three response variables—Gas film lifetime, discharge current standard deviation, and mean discharge energy—were chosen to assess gas film stability. A summarized experimental design, along with corresponding quality characteristics, is provided in Table 4.4. Each run was performed five times,

and the average response variables obtained from these trials constituted the final quality characteristics.

The experimental results have been analyzed using analysis of variance (ANOVA). The outcomes of ANOVA for the response variables are presented in Table 4.3. The outcomes were then further analyzed using the statistical tools outlined in Section 3.4.2. The coefficient of determination (R-squared) values for the three responses exceed 50%, which is an acceptable rate for identifying trends and behavior patterns with respect to the stochastic nature of the SACE process. The input parameter, Period (C), was omitted from the ANOVA analysis because its effects on the three response variables were found to be insignificant (P-value $> 0.05$).

Table 4.3 Analysis of variance of the three response variables.

| Source | Term df | Error df | F-value | p-value | |
|---|---|---|---|---|---|
| **Response $Y_1$: Gas film lifetime** | | | | | |
| **Whole-plot** | 3 | 14.01 | 5.09 | 0.0168 | significant |
| a-Electrolyte | 3 | 14.01 | 5.09 | 0.0168 | |
| **Subplot** | 19 | 108.41 | 6.46 | < 0.0001 | significant |
| B-Applied Signal | 3 | 108.47 | 8.33 | < 0.0001 | |
| C-On-time | 1 | 123.83 | 0.8772 | 0.3511 | |
| Standard deviation = 1.22, mean = 1.73, coefficient of variation % = 70.44, $R^2$ = 0.516, Adjusted $R^2$ = 0.416 | | | | | |
| **Response $Y_2$: Discharge current standard deviation** | | | | | |
| **Whole-plot** | 3 | 14.90 | 11.79 | 0.0003 | significant |
| a-Electrolyte | 3 | 14.90 | 11.79 | 0.0003 | |
| **Subplot** | 19 | 112.95 | 6.92 | < 0.0001 | significant |
| B-Applied Signal | 3 | 112.98 | 23.64 | < 0.0001 | |
| C-On-time | 1 | 112.99 | 22.28 | < 0.0001 | |
| Standard deviation = 0.0351, mean = 0.2475, coefficient of variation % = 14.20, $R^2$ = 0.663, Adjusted $R^2$ = 0.596 | | | | | |
| **Response $Y_3$: Discharge mean energy** | | | | | |
| **Whole-plot** | 3 | 11.77 | 29.82 | < 0.0001 | significant |
| a-Electrolyte | 3 | 11.77 | 29.82 | < 0.0001 | |
| **Subplot** | 19 | 111.33 | 9.44 | < 0.0001 | significant |
| B-Applied Signal | 3 | 111.67 | 26.38 | < 0.0001 | |
| C-On-time | 1 | 111.17 | 3.72 | 0.0562 | |
| Standard deviation = 0.3199, mean = 1.43, coefficient of variation % = 22.42, $R^2$ = 0.771, Adjusted $R^2$ = 0.724 | | | | | |

Table 4.4 Design of experiments with the response variables.

| Input process parameters | | | | | Response Variables | | |
|---|---|---|---|---|---|---|---|
| Runs | A | B | C | D | Avg, $Y_1$ | Avg, $Y_2$ | Avg, $Y_3$ |
| | - | - | (ms) | (%) | (ms) | (A) | (J) |
| 1 | NaOH 20 wt% | Ramp | 8 | 70 | 1.506 | 0.237 | 1.926 |
| 2 | NaOH 20 wt% | Pulse | 8 | 70 | 0.958 | 0.311 | 2.806 |
| 3 | NaOH 20 wt% | Sinusoidal | 8 | 90 | 5.032 | 0.234 | 1.424 |
| 4 | NaOH 20 wt% | Ramp | 8 | 90 | 1.008 | 0.242 | 1.708 |
| 5 | NaOH 20 wt% | Pulse | 8 | 90 | 2.206 | 0.189 | 3.053 |
| 6 | NaOH 20 wt% | Triangle | 8 | 90 | 2.371 | 0.212 | 1.626 |
| 7 | NaOH 20 wt% | Triangle | 8 | 70 | 2.695 | 0.251 | 1.611 |
| 8 | NaOH 20 wt% | Sinusoidal | 8 | 70 | 4.297 | 0.189 | 2.061 |
| 9 | KOH 45 wt% | Pulse | 8 | 90 | 1.529 | 0.309 | 1.223 |
| 10 | KOH 45 wt% | Ramp | 8 | 70 | 1.223 | 0.296 | 1.132 |
| 11 | KOH 45 wt% | Sinusoidal | 8 | 90 | 1.554 | 0.256 | 1.077 |
| 12 | KOH 45 wt% | Triangle | 8 | 70 | 1.555 | 0.295 | 1.245 |
| 13 | KOH 45 wt% | Pulse | 8 | 70 | 1.166 | 0.362 | 1.416 |
| 14 | KOH 45 wt% | Ramp | 8 | 90 | 1.278 | 0.266 | 1.206 |
| 15 | KOH 45 wt% | Sinusoidal | 8 | 70 | 1.865 | 0.278 | 1.210 |
| 16 | KOH 45 wt% | Triangle | 8 | 90 | 1.345 | 0.274 | 1.104 |
| 17 | NaOH 30 wt% | Ramp | 8 | 70 | 0.931 | 0.274 | 1.972 |
| 18 | NaOH 30 wt% | Sinusoidal | 8 | 70 | 1.141 | 0.228 | 1.251 |
| 19 | NaOH 30 wt% | Pulse | 8 | 90 | 1.480 | 0.250 | 1.611 |
| 20 | NaOH 30 wt% | Triangle | 8 | 90 | 1.274 | 0.207 | 1.143 |
| 21 | NaOH 30 wt% | Sinusoidal | 8 | 90 | 1.258 | 0.205 | 1.146 |
| 22 | NaOH 30 wt% | Ramp | 8 | 90 | 1.163 | 0.206 | 1.274 |
| 23 | NaOH 30 wt% | Pulse | 8 | 70 | 0.931 | 0.274 | 1.971 |
| 24 | NaOH 30 wt% | Triangle | 8 | 70 | 1.206 | 0.214 | 1.149 |
| 25 | KOH 50 wt% | Ramp | 8 | 90 | 1.379 | 0.236 | 1.164 |
| 26 | KOH 50 wt% | Ramp | 8 | 70 | 1.256 | 0.247 | 0.900 |
| 27 | KOH 50 wt% | Sinusoidal | 8 | 90 | 1.587 | 0.194 | 0.990 |
| 28 | KOH 50 wt% | Triangle | 8 | 90 | 1.705 | 0.220 | 1.034 |
| 29 | KOH 50 wt% | Sinusoidal | 8 | 70 | 2.337 | 0.221 | 1.092 |
| 30 | KOH 50 wt% | Pulse | 8 | 90 | 1.520 | 0.249 | 0.874 |
| 31 | KOH 50 wt% | Pulse | 8 | 70 | 1.176 | 0.317 | 1.133 |
| 32 | KOH 50 wt% | Triangle | 8 | 70 | 1.703 | 0.212 | 1.019 |

A = Electrolyte type; B = Applied signal; C = Period (ms); D = On-time (%);

$Y_1$ = Gas film lifetime (ms); $Y_2$ = Discharge current standard deviation (A); $Y_3$ = Mean discharge energy (J)

## 4.1 Effects of Parameters on Response Variables

In this section, the presented graphs are used to show the impact of individual process parameters on the response variables. Within each plot, the parameter of interest is varied from its lowest to its highest level, while keeping the remaining factors at their mid-level values. The mentioned levels are specified in Table 4.1.

### 4.1.1 Effects of Electrolyte

In the SACE process, the electrolyte plays a crucial role as it establishes a conductive pathway connecting the electrodes within the electrochemical circuit. The electrical conductivity and viscosity are modified by the nature and concentration of the electrolyte, which in turn significantly influences the stability of the gas film. It's important to note that gas film stability isn't solely contingent upon electrical parameters; the surrounding environment of the tool-electrode plays a key role. The impact of the electrolyte on the response variables is visually depicted in Fig. 4.2.



Figure 4.2: The electrolyte effect on the gas film lifetime (ms), discharge mean energy (J) and discharge current standard deviation (A).

The gas film lifetime is influenced by the chemical used, with NaOH electrolytes having a greater effect on gas film lifetime compared to KOH electrolytes. Conversely, the use of KOH appears to have a more positive on the gas film thickness, as indicated by the reduction in the discharge mean energy. These observations could be attributed to differences in the electrolytes' natures, given that NaOH electrolytes exhibit higher viscosity than KOH electrolytes, without displaying significant increase in conductivity.

At concentrations below 30 wt% NaOH and a temperature of $50^{o}C$, the electrolyte's conductivity increases with concentration. However, after reaching this threshold, conductivity diminishes due to ionic recombination inside the solution. Consequently, concentrations at and above 30 wt% NaOH only increase solution viscosity, without enhancing the electrolyte's electrical properties. The corresponding value for KOH, is approximately 50 wt%. Thus, to achieve equivalent conductivity to NaOH, KOH requires higher concentrations due to its greater molecular weight. Additionally, since KOH-based electrolytes have significantly lower viscosity, their concentration could be raised without significant influence on the electrolyte flow.

The electrolyte with the highest conductivity, KOH 45wt%, resulted in accelerated discharge rates that are difficult to control, as evident from its high discharge standard deviation. Furthermore, gas film lifetime significantly decreases due to discharge instability, leading to frequent gas film breaks. In contrast, the electrolyte with the highest viscosity, NaOH 30wt%, struck a balance between gas film dynamics and discharge control. However, the high mean energy implied a thick gas film, which is unfavorable for machining accuracy. Similar observations were noted for NaOH 20wt%. In summary, increasing electrolyte viscosity prolongs gas film stability, yet an excessive increase negatively impacts electrolyte flow dynamics, consequently affecting discharge behavior. This observation aligns with mean discharge energy plots (See Fig. 4.2), illustrating thicker gas films in NaOH electrolytes compared to KOH. NaOH electrolytes can find use in applications requiring fine surface roughness, such

as polishing, due to tightly controlled sparks indicated by low standard deviation.

Considering KOH electrolytes, KOH 50% wt. displayed favorable trade-offs among the three response variables compared to KOH 45% wt. This could be attributed to the lower conductivity of KOH 50% wt., preventing excessive discharges, and extending the gas film lifetime. The aim was to strike a balance between OH- radical concentration, electrical conductivity, and electrolyte viscosity. Among the four studied electrolytes, KOH 50 wt% and NaOH 30 wt% exhibit the most favorable combination of responses. The preference between them, however, would be more contingent on the machining application of interest. For applications involving significant machining depths or high material removal rates, such as roughing routines, the preferred electrolyte would be KOH 50 wt%, as it facilitates higher electrolyte circulation along with sufficient discharge rates. Conversely, for applications requiring shallower machining depths and finer precision, such as polishing routines, NaOH 30 wt% would be a more viable option, provided that appropriate electrolyte circulation can be maintained through techniques like tool rotation or bulk flow via pump.

## 4.1.2   Effects of On-time and Period

Electrical inputs such as on-time and period play a key role in influencing the amount of heat energy transferred to the region around the tool. The duration of a full cycle of the signal, represented by the period, encompasses the combined on-time and off-time durations. It's important to note that during the off-time, the voltage did not equate to zero, as discussed in Section 3.5. Specifically, the low-level and high-level voltages were used to control the off-time and on-time intervals, respectively. In general, increasing the on-time duration increases the portion of the period where the voltage surpasses the critical voltage threshold, thus facilitating discharge activity. A direct correlation exists between the increase in on-time duration and rise in temperature. Elevated temperatures lead to improved gas film stability, a point discussed in Section 2.2.2 and evident from the on-time effects graph depicted in Fig.4.3.
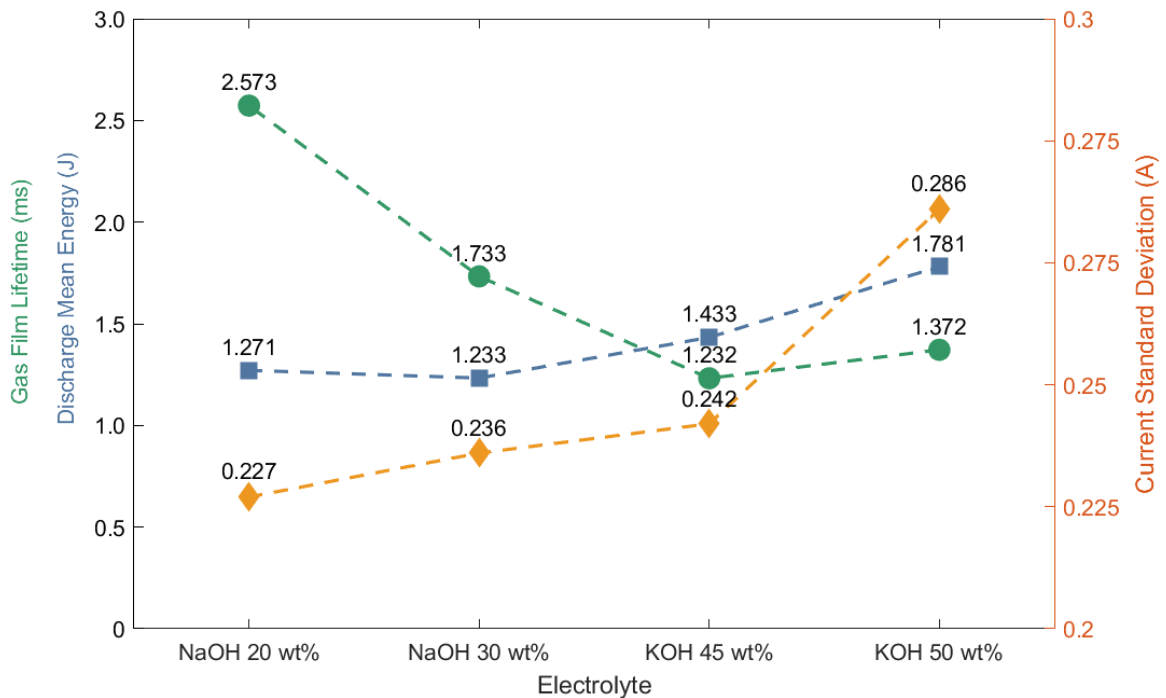
Figure 4.3: The On-time effect on the gas film lifetime (ms), discharge mean energy (J) and discharge current standard deviation (A).

The plots can be interpreted as follows: An increase in the on-time leads to a prolonged gas film lifetime, improved control over discharge activity, and the emergence of a thinner gas film, as indicated by the reduction in mean energy. The increase in period should theoretically yield similar trends to the those of the on-time; however, the period, as a parameter, was found to hold no significant influence on the response variables. This conclusion comes from its high p-value exceeding 0.05. Essentially, this implies that the effects illustrated in Fig. 4.4 lack the strength to establish robust correlations between the input and output. The observed variance is thus categorized as random and beyond the scope of the model's explanatory capacity. However, this outcome doesn't negate the potential impact of the period value on the process. It's possible that this result is a consequence of selecting levels that are near one another. Employing a broader range of levels could potentially yield a different interpretation.
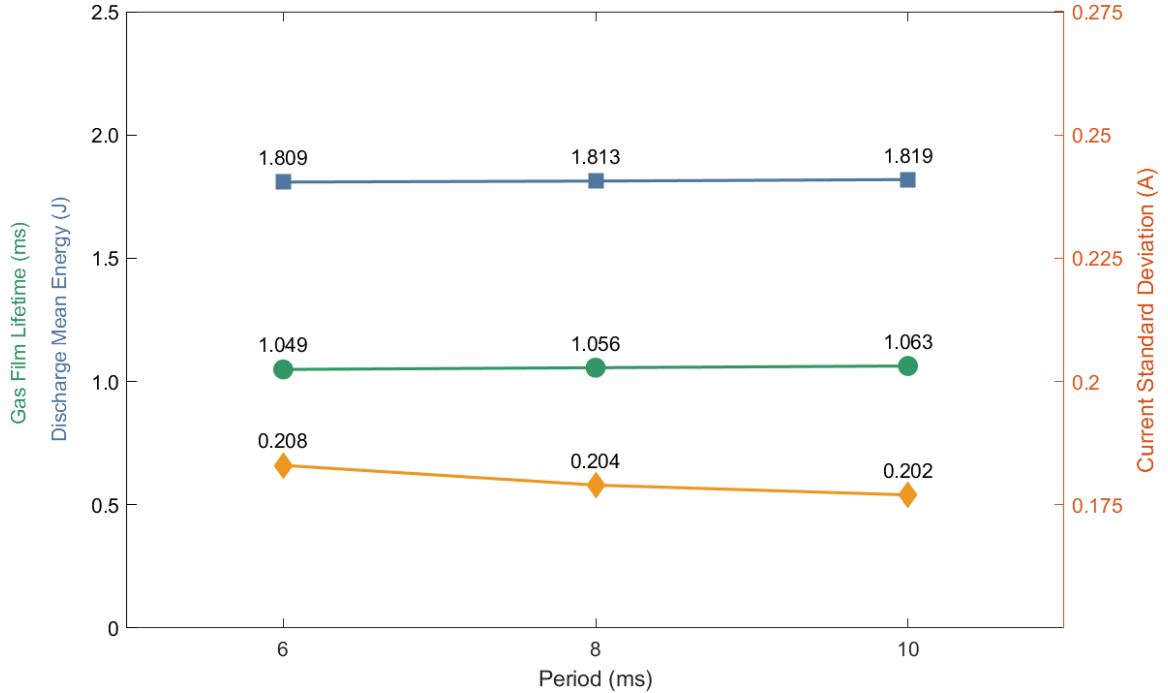
Figure 4.4: The period effect on the gas film lifetime (ms), discharge mean energy (J) and discharge current standard deviation (A).

### 4.1.3 Effects of Signal Shape

The applied signal primarily influences the forming and collapsing cycle of the gas film. This cycle affects the microscopic flow around the tool-electrode, as uncontrolled gas film dynamics result in randomized machining quality. The signal's shape exerts a hydrodynamic impact alongside its main influence on discharge quality. This rises from the fact that the heat energy transferred to the machining zone through discharges is governed by the electrical inputs, as evident by the effects of the on-time and period. In the context of SACE, the pulse signal has gained widespread usage over DC signals due to its implied ability to control the temperature around the tool. In this study, the exploration of alternative signals beyond the pulse signal was motivated by the aim of using the pulse's temperature-controlling effect while enhancing the control over gas film dynamics. This was intended to extend the gas film duration without compromising the discharge quality. The impact of the applied signals on the gas film lifetime and the other response variables is illustrated in Fig. 4.5.
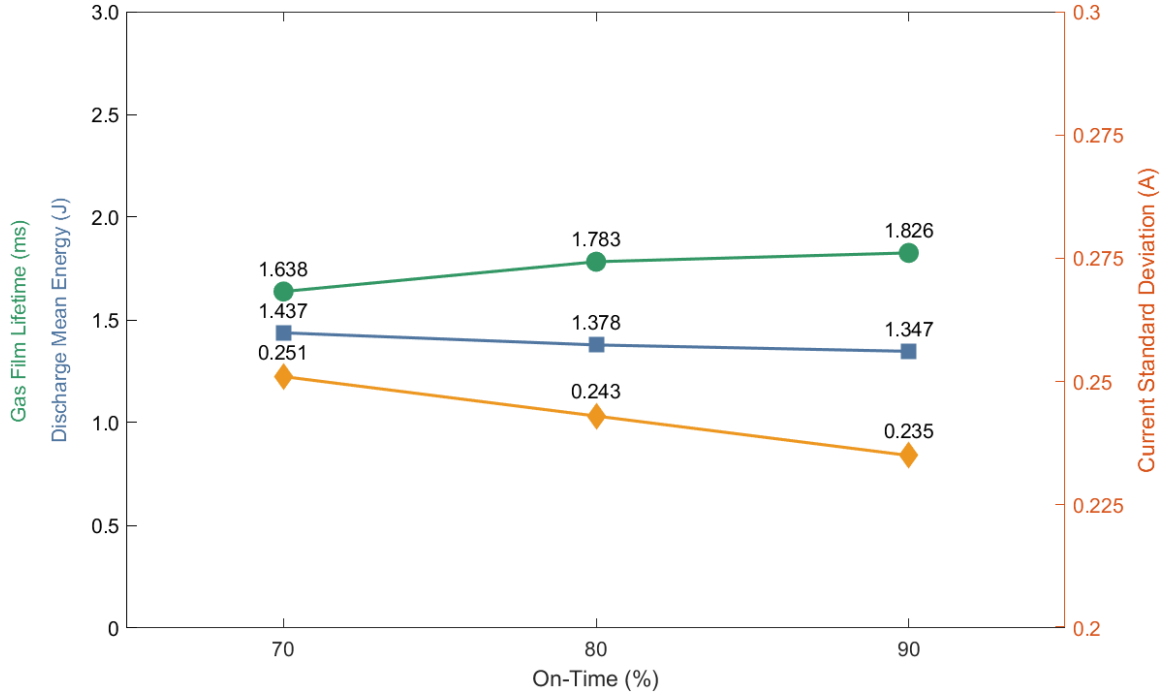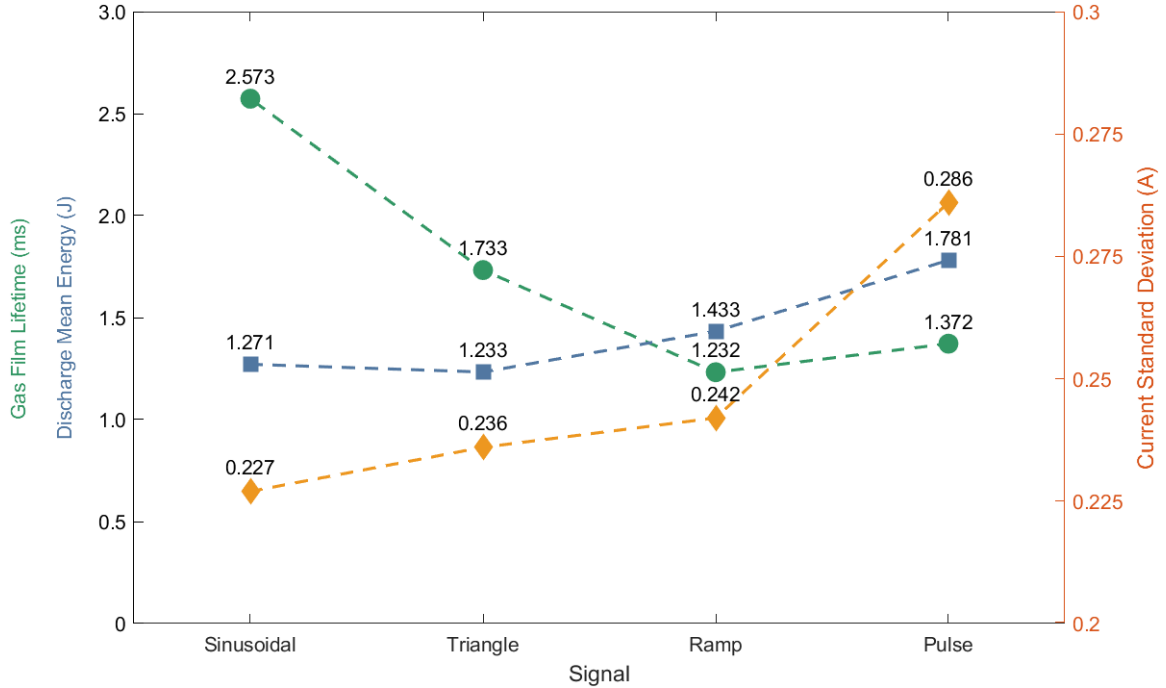
Figure 4.5: The signal shape effect on the gas film lifetime (ms), discharge mean energy (J) and discharge current standard deviation (A).

Upon analyzing the performance of each signal, it becomes apparent that introducing novel alternative signals to the process can open new avenues for enhancing SACE, especially the stability of the gas film. The alternative signals have shown significant impacts on the three response variables. For instance, when comparing the ramp signal to the pulse signal, it is evident that the former displays improvements in discharging behavior. This improvement can be attributed to the gradual voltage increase achieved through the angled ascending edge of the ramp signal, which differs from the square shape of the pulse signal. However, the positive impact of the ramp shape seems confined to this aspect, as its gas film lifetime doesn't exhibit a substantial difference compared to the pulse signal. This might be attributed to the flat falling edge observed in both signals, which doesn't provide a favorable environment for extending the gas film's duration.

This observation gains further support when comparing the effects of the ramp shape with the triangle shape. The symmetrical edges of the triangle signal enhance

the gas film lifetime, along with a slightly improved discharging behavior compared to the ramp shape. In conclusion, these results underline the significance of the latter portion of the signal shape, where the voltage dips below the critical voltage threshold, as a pivotal parameter in sustaining gas film lifetime. Furthermore, the triangle shape stands out for its ability to generate the thinnest gas films among all the signals, a characteristic attributed to its low mean discharge energy. This suggests a potential for achieving machining outcomes with improved accuracy. However, additional validation through machining experiments is imperative to validate this hypothesis.

Up to this point, the presented results have backed up the preference of applying signals with angled edges compared to flat edges. This notion is further extended by the outcomes derived from the sinusoidal signal, which employs curved edges. In SACE, gas film stability is determined by its capacity to retain its shape during discharging activity, with variations in shape leading to changes in thickness. Thin gas films demand less energy for breakage, making signals with low discharge mean energy preferable. The sinusoidal signals exhibited an average discharge energy of 1.27 J, while the pulse signals had 1.78 J, suggesting the presence of thinner gas films. Moreover this 28% reduction, is further supported by a 20% reduction in discharge standard deviation showing notable improvements in discharge characteristics. The most pronounced impact of employing curved edges becomes evident in the gas film lifetime output. The plots of sinusoidal signals demonstrated a significantly longer gas film lifetime when compared to the pulse signal plots. On average, the gas film lifetime for sinusoidal signals was 2.57 ms, whereas for pulse signals, it was 1.37 ms, resulting in an 87% elongation of the average gas film lifetime.

Notably, some instances were observed in sinusoidal signals where the lifetimes surpassed the assigned period without breakage, resulting in extended durations where the gas film remained stable. These instances were noted in the runs where the sinusoidal signal was employed in combination with KOH 50 wt%. Lifetimes exceeding

the period were excluded from the analysis to avoid data imbalance and measured separately, showing durations reaching up to 35 ms. Upon analyzing the corresponding camera footage of the signal plots, the elongated gas film observed in the sinusoidal signals was attributed to a self-repair phenomenon of the gas film. This phenomenon was not observed in the other signals employed in this study, suggesting that it is specifically associated with the sinusoidal signals. Further discussion on this self-repair phenomenon and the extended regions with stable gas film is presented in the Section 4.2.

## 4.2 Elongated Gas Film Lifetimes in Sinusoidal Signals

Two main phenomena were exclusively observed in the sinusoidal signals: elongated gas film lifetimes and gas film self-repair, contributing to the prolonged duration of stable gas film. During a 500 ms experimental run, involving multiple sinusoidal waveforms ($\approx$ 63 waveforms), where the gas film experienced multiple breaks, the longest observed gas film lifetime was 35 ms. The summation of gas film lifetimes, referred to as the total stable gas film duration, averaged 77 ms. Note that the pulse signal, within the same experimental run duration, displayed an average gas film lifetime of only 2.5 ms. The investigation of the gas film under sinusoidal-shaped voltage is depicted in Fig. 4.6, highlighting the stable gas film and the associated self-repair phenomena. The SACE process current illustrated in Figure 3b corresponds to recorded signals at 370 ms after the voltage was turned on. A total of 10 distinct timestamps and one time range were identified, and their corresponding images are presented below. In Image 0 of the Figure, the tool tip is shown before running the SACE machine, serving as a reference. At timestamp 1, the gas film formation was captured, which gradually stabilized at timestamp 2. Subsequently, a spike occurred at timestamp 3, but the recorded footage revealed that the gas film remained intact throughout this spike. Some bubbles were observed to be released from the gas film,

which rapidly filled. (Gas film repair). The gas film remained stable for approximately 36.5 ms as shown in timestamps 4, 6, 8, and 11.

This particular type of gas film exhibits robust shape as shown in the images corresponding to the mentioned timestamps. However, this robust gas film seems to be incapable of creating a constant discharging channel. This observation is quantitatively supported by the substantial difference in discharge frequency. Sinusoidal signals exhibited an average frequency of 168 discharges per run, in contrast to the pulse signals that displayed 3236 discharges per run. This might pose a challenge when sinusoidal signals are applied in machining applications, which necessitate further investigation.

The gas film exhibited self-repair in timestamps in some periods including the multiple timestamps in images 5-1 to 5-4 and timestamps 7 and 10. The four timestamps 5-1 to 5-4 are separated by a 0.06 ms interval, showcasing the process of gas film self-repair. Figure 5-a marks the initiation of the process, where the gas film begins releasing bubbles. In figure 5-b, the gas film has formed into a large bubble but has not merged. At this stage, the tool is not isolated, and current flows through the electrolyte for a brief period. In figure 5-c, the bubbles start to coalesce, forming the gas film once again. Figure 5-d depicts the self-repaired gas film. It is important to note that the gas film is not completely broken; it initiates the repair process but does not reach completion. Hence, it is referred to as gas film repair. The entire process takes approximately 0.2 ms. A spark was emitted during the process, observed in timestamp 9. Beyond timestamp 11, the gas film is disrupted, marking the formation of another gas film region. Similar gas film formations were recorded at other instances during this footage.
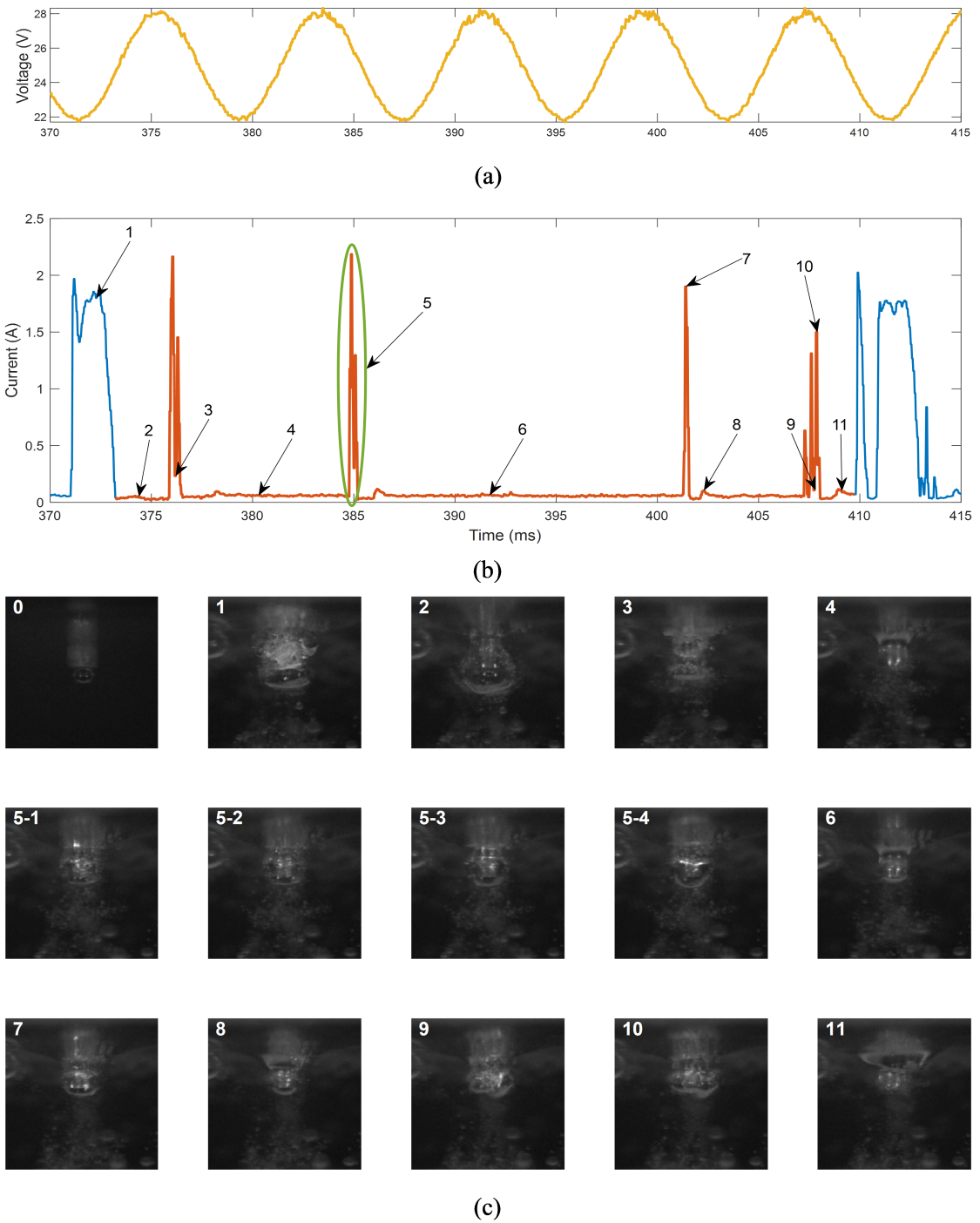
Figure 4.6: (a) Voltage-Time plot of the applied sinusoidal-shaped input signals (b) Current-Time plot of the SACE process. Gas film formation signals colored in blue. Stable gas film colored in orange. (c) High speed images corresponding to 11 distinct timestamps on the Current-Time plot of the SACE machine tool and the gas film around it.

## 4.3 Repeatability Study

To ensure the reproducibility of the extended lifetimes, or stable gas film regions discussed in Section 4.2, a separate study was conducted.The input factors considered in this study were the on-time (A) and period (B), each with three varying levels: 70%, 80%, and 90% for the duty cycle, and 6 ms, 8 ms, and 10 ms for the period, mirroring the parameter levels used in the main characterization study. Other variables such as electrolyte (KOH 50 wt%), tool geometry (Cylindrical $\Phi$500 µm), and immersion depth (1 mm) were controlled and blocked as they were not the focus of this study. A total of 135 runs were conducted, with the study consisting of 15 repetitions. The response variable of interest was the total stable gas film duration (R1) measured in milliseconds within a 500 ms duration.

To assess the validity of the design model, an analysis was conducted on the residuals versus runs plot and the normal plot of residuals, as shown in Fig. 4.7. The normal plot of residuals compares the observed residuals, which represent the discrepancies between the observed and predicted values, with the expected residuals assuming a normal distribution. It was observed that the residuals closely followed the diagonal reference line, indicating that they conform to a normal distribution. Furthermore, the residuals vs. runs plot was employed to evaluate the randomness and independence of the residuals. This plot illustrates the residuals on the y-axis and the order of the observations or runs on the x-axis. Upon examination, it was evident that the residuals exhibited a random distribution around the zero line, with no discernible patterns or trends. This observation suggests that the assumptions of randomness and independence were satisfied.
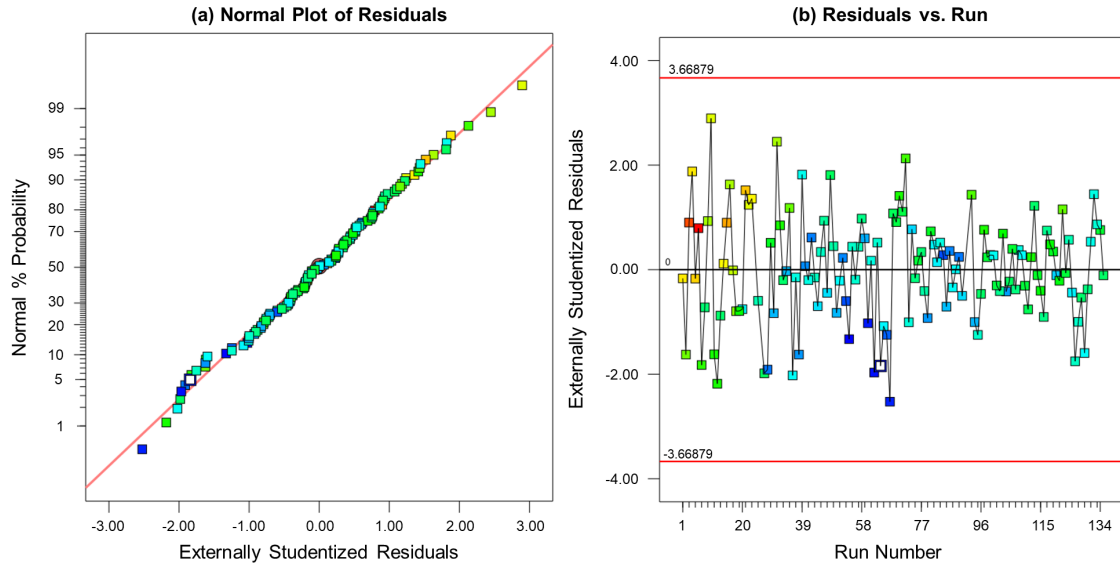
Figure 4.7: (a) Normal Residuals Plot: Residuals conform to a normal distribution. (b) Residuals vs. Run Plot: Residuals exhibit no discernible patterns or trends, as desired.

After making further adjustments, an analysis of variance (ANOVA) was performed to assess the gas film stable duration, as presented in Table 4.5. The significant Model F-value of 7.62 ($> 0.05$) indicates that the model holds importance. The likelihood of obtaining such a large F-value due to random variation is only 0.33%. The lack-of-fit F-value of 0.41 implies the lack-of-fit is not significant as desired. Model terms with p-values below 0.05 are deemed significant, and in this case, both the model and the on-time exhibit significance, affecting the lifetime of the gas film. The adequate precision metric assesses the signal-to-noise ratio, with a value exceeding 4 considered favorable. With a ratio of 7.959, the model demonstrates sufficient signal strength to navigate the design space, shown in Fig. 4.7. To establish the relationship between the input process parameters (On-time and period) and the response variable (R1), a regression analysis was conducted. The resulting model is presented in Equation 4.1.

Table 4.5 Fit statistics and Analysis of variance for total stable gas film duration.

| Source | SS | DOF | MS | F-value | p-value | |
|---|---|---|---|---|---|---|
| **Response (R1): Total duration of stable gas film** | | | | | | |
| Block | 8955.91 | 14 | 639.71 | | | |
| Model | 1964.35 | 3 | 654.78 | 5.09 | 0.0089 | significant |
| A-On-Time | 1906.31 | 1 | 1906.31 | 14.81 | 0.0010 | |
| B-Period | 1.73 | 1 | 1.73 | 0.0135 | 0.9088 | |
| AB | 56.31 | 1 | 56.31 | 0.4376 | 0.5129 | |
| Residual | 2573.87 | 20 | 128.69 | | | |
| Lack of Fit | 315.23 | 5 | 63.05 | 0.4187 | 0.8285 | not significant |
| Pure error | 2258.63 | 15 | 150.58 | | | |
| Cor total | 13494.13 | 37 | | | | |

Standard deviation = 11.34, mean = 74.38, coefficient of variation % = 15.25, $R^2$ = 0.516, Adjusted $R^2$ = 0.416, adequate precision = 7.959.

$$R1 \text{ (ms)} = -71.47166 + 1.84193 \times A + 7.3025 \times B - 0.0938 \times AB \qquad (4.1)$$

Where,

A = On-time (%)

B = Period (ms)

R1: Stable gas film duration

The graphs shown in Fig. 4.8 and 4.9 are used to explain the effect of individual process parameters on the response . These graphs were plotted by using the regression model given in Equation 4.1. Fig. 4.8 shows the design space which is the predicted response behavior that is bounded by the maximum and minimum response (R1) of this study based on the investigated set of parameters contour shown in Fig. 4.8B. Fig. 4.9 shows the trends in gas film lifetime in relation to the input parameters that can be used to identify parameters of interest for future investigations.
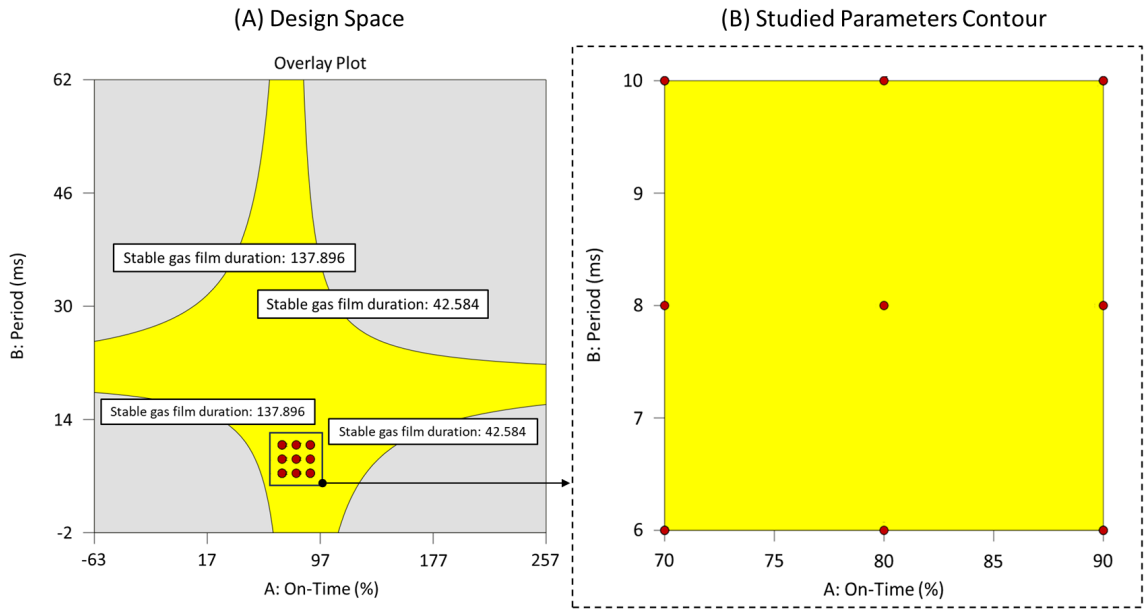
Figure 4.8: Repeatability Study Models: (A) Design space outlined by the regression model. (B) Parameters input into the regression model.
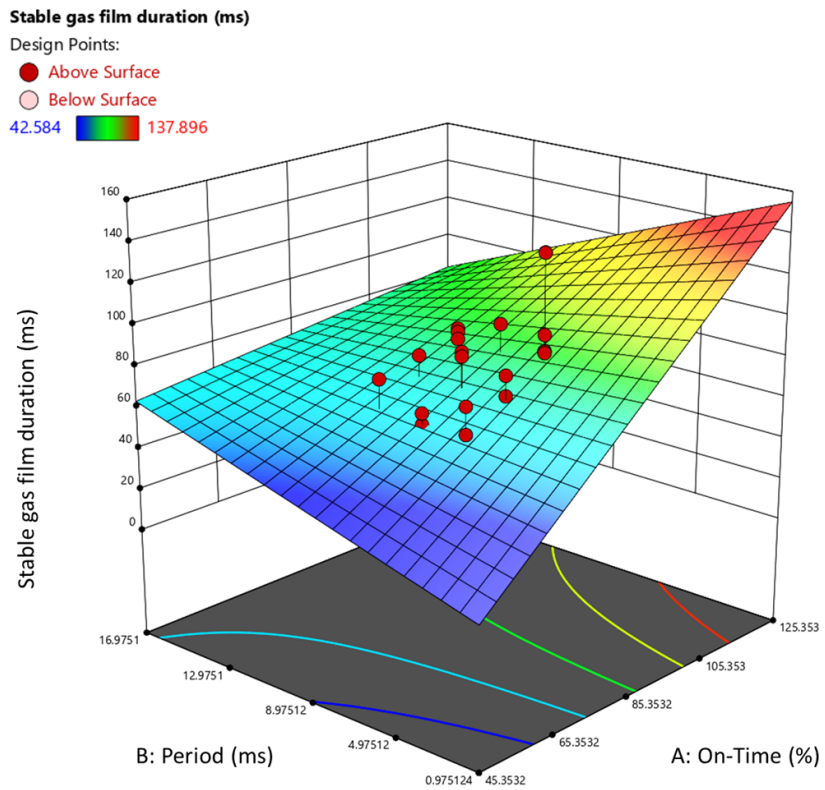


Figure 4.9: Optimality graph for analyzing stable gas film duration trends

71

## 4.4 Multi objective optimization

Towards applying the characterization experiments investigation to machining applications, it becomes possible to define a process range that aligns with the desired objectives. The literature reveals numerous studies that have employed optimization techniques based on the desirability approach to fine-tune process parameters for the achievement of specific goals [85–87]. Referring to Fig. 4.10, which illustrates all the experimental runs plotted against the corresponding response outputs, it becomes evident that a desired range of optimality can be reached by implementing multi-objective optimization strategies.
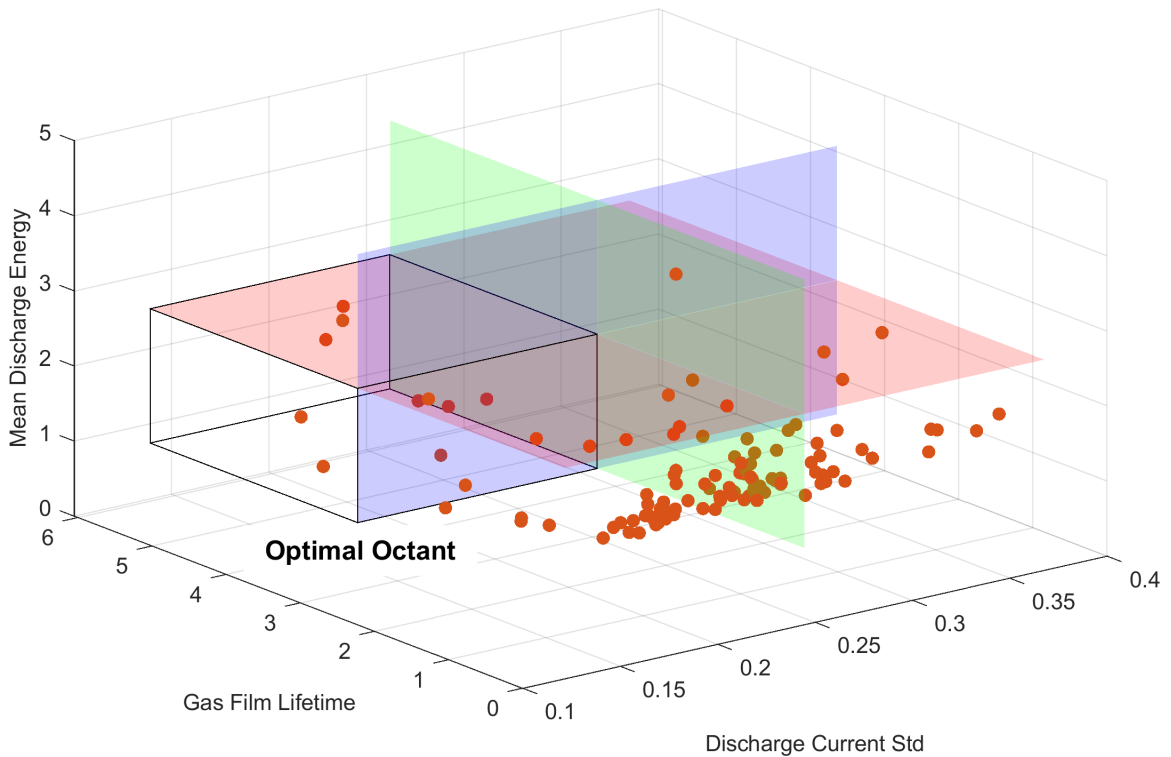


Figure 4.10: 3D scatter plot depicting the recorded experimental runs in relation to the three response outputs. The planes within the plot partition it into eight octants, dividing them according to any specified objectives.

In the following study, the desirability approach was employed to optimize parameter ranges for achieving the maximum gas film lifetime, minimum standard deviation of discharge current, and minimum mean discharge energy. The Design Expert soft-

ware's optimization toolbox was used to conduct this study, operating within the boundary upper and lower limits of the parameter ranges (Table 4.1). The optimal process parameters comprise of KOH 50 wt% electrolyte, sinusoidal signal, and 90% on-time, as tabulated in Table 4.6.

Table 4.6 Predicted results to optimize maximum $Y_1$, minimum $Y_2$ and $Y_3$.

| | Predicted optimum parameters | | | Predicted responses | | | Desirability |
|---|---|---|---|---|---|---|---|
| | A | B | C | $Y_1$ | $Y_2$ | $Y_3$ | $D_f$ |
| Limits | NaOH 20 wt% > KOH wt% | Sinusoidal > Pulse | 70 > 90 | | | | |
| Units | | | % | ms | A | J | |
| **1** | **KOH 50 wt%** | **Sinusoidal** | **90** | **2.056** | **0.206** | **0.999** | **0.627** |
| 2 | KOH 50 wt% | Triangle | 90 | 1.687 | 0.215 | 1.016 | 0.593 |
| 3 | NaOH 20 wt% | Sinusoidal | 90 | 4.905 | 0.201 | 1.564 | 0.592 |
| 4 | KOH 50 wt% | Triangle | 70 | 1.930 | 0.240 | 0.961 | 0.586 |
| 5 | KOH 50 wt% | Sinusoidal | 70 | 1.879 | 0.230 | 1.074 | 0.576 |
| 6 | NaOH 30 wt% | Sinusoidal | 90 | 1.403 | 0.192 | 1.134 | 0.575 |
| 7 | KOH 50 wt% | Ramp | 70 | 1.675 | 0.245 | 1.000 | 0.558 |
| 8 | KOH 50 wt% | Pulse | 90 | 1.811 | 0.261 | 0.939 | 0.554 |

## 4.5   Gas film thickness evaluation

To validate the findings discussed earlier, a high-speed camera was employed to assess the gas film thickness for the two most optimal signals—Sinusoidal and Triangle—identified through the results of the multi-objective study, as well as the baseline signal, Pulse, under the most optimal parameter combination (Electrolyte = 50% KOH, On-time = 90%, and Period = 8 ms). Fig. 4.11 shows the findings, where the thickness measurement was evaluated using the edge detection methods outlined in Section 3.6.1. The thickness outputs align with the results of the quantitative analysis. In this regard, runs employing the pulse signal exhibit thicker gas films compared to those using the sinusoidal and triangular signals.
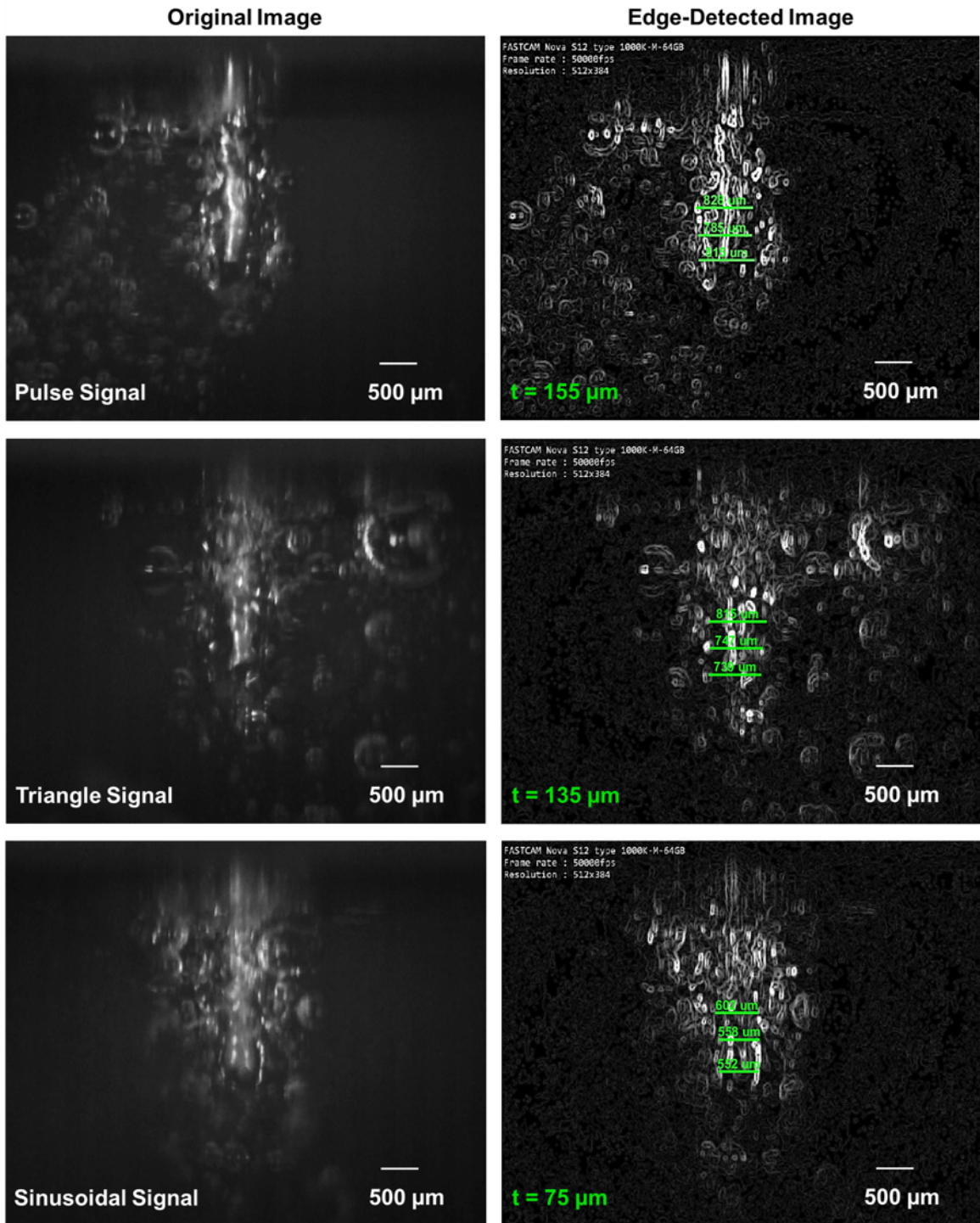
Figure 4.11: Gas film thickness assessment using the edge-detection method in MAT-LAB for the pulse, sinusoidal and triangle signals (Electrolyte = 50% KOH, On-time = 90%, and Period = 8 ms)

## 4.6    Chapter Summary

An experimental study in SACE was conducted to explore the behavior of gas film using previously unexplored signals (Sinusoidal, triangle and ramp). Previous studies in SACE have predominantly concentrated on DC and pulsed signals. SACE process current signal datapoints and corresponding high-speed footage frames were utilized to assess the gas film behavior. Gas film lifetime, current discharge standard deviation and mean discharge energy were the response outputs of interest. From the experimental results, the following conclusions are drawn:

- KOH 50 wt% and NaOH 30% are found to be the ideal electrolyte concentration for enhancing gas film stability.

- Electrical inputs such as period and on-time contribute to the amount of heat energy transferred to the machining zone.

- The use of an offset low voltage combined with the novel signal shapes used in this study contributes positively to the gas film stability in terms of thickness, lifetime, and discharge control.

- The use of sinusoidal-shaped signals results in gas films exhibiting significantly longer gas film lifetimes in comparison with DC and pulse signals with durations reaching up to 35 ms. A factorial investigation was conducted to verify the reproducibility of the observed extended stable gas film durations.

- When applying sinusoidal signals, the gas film attempts to self-repair and maintain stability elongating the gas film lifetime and exhibiting robust thickness as evidenced by a prompt spike observed in the current vs. time plot and high-speed images. Despite this advantageous characteristic, the gas film remains unable to facilitate consistent path discharge.

- A multi objective optimization study was conducted and it was found that the optimal process parameters comprise of KOH 50 wt% electrolyte, sinusoidal signal, and 90% on-time.

- A high-speed camera was employed alongside the edge detection methods in MATLAB to quantify the gas film thickness for optimal signals (Sinusoidal, Triangle) and baseline signal (Pulse). Findings align with the outputs of the multi-objective optimization study.

# Chapter 5

# Machining Experiments

In the characterization experiments, the significance of altering signal shapes to enhance gas film quality was observed through signal processing and visual evaluation of the gas film. Additionally, the ideal parameter values employed in the study have been identified, allowing for the transition from an exploratory study of the gas film to an investigation of the gas film in practical, real-world machining applications. Therefore, the focus of this chapter will be on evaluating the impact of signal shapes on machining outputs and exploring avenues for improving the machining quality. The chapter begins by outlining the machining experiments, including the setup and analysis. Afterwards, it discusses the machining outcomes and explores opportunities for improvement through signal design enhancements and the use of surfactants for electrolyte enhancement.

## 5.1 Machining Experiments Outline

The baseline for the machining experiments was established by initially assessing the outcomes of the characterization study. This assessment specifically concentrated on the top output distinguished of the multi-objective study in Section 4.4. This output was then compared to the highest-ranking pulse signal in the multi-objective study, which is the most common signal in literature. The rationale behind this methodology is to compare signals of high quality that hold relevance to machining applications, as

opposed to contrasting signals characterized by extreme conditions, which typically yield sub-optimal results. The attributes of the signals under study are presented in Fig. 5.1.



Figure 5.1: Signal shape attributes radar chart. Attributes normalized on a scale from 0 to 10. Center of the circle indicates zero, while the outer edge signifies 10.

In the following machining experiments, the pulse and sinusoidal signal shapes were used to drill holes at different depth, using two different electrolytes: 50% KOH and 30% NaOH. The same set of blocked parameters outlined in the characterization experiments was employed to draw correlations between the gas film analysis outcomes of Chapter 4 and the machining analysis outcomes in this chapter. The details of the process parameters and their corresponding levels are presented in Table 5.1. Each hole was machined three times, and the average response variables obtained from these trials constituted the final quality characteristics.

Table 5.1 Machining parameters and their levels.

| Process Parameters | Level & Units | |
|---|---|---|
| Variable process parameters | Level 1 | Level 2 |
| 1  Electrolyte type, A | KOH 50 wt% | NaOH 30 wt% |
| 2  Applied Signal, B | Pulse | Sinusoidal |
| 3  Machining Depth, C | 100 $\mu$m | 300 $\mu$m |
| Constant process parameters | | |
| 4  Feed Rate | 3 $\mu$m/sec | |
| 5  Electrolyte Flow Rate | 9.28 ml/min | |
| 6  Immersion Depth | 1 mm | |
| 7  Applied voltage | $1.24\times(\text{U}_{crit})$ | |
| 8  Period | 8 ms | |
| 9  On-time | 90% | |
| 10  Tool diameter | 500 $\mu$m | |
| 11  Tool material | Stainless-steel | |
| 12  Tool Geometry | Cylindrical | |

## 5.2  Machining Setup

The subsequent section details the setup and machining routine employed in the experiments. The acrylic processing cell includes the workpiece holder and essential components to facilitate consistent tool immersion depths and a continuous overflow of fresh electrolyte via a peristaltic pump. The processing cell is mounted on XY stages, allowing movement in both the x and y-axes. The machine head is mounted on a Z-stage of a cartesian robot. A cylindrical stainless-steel tool with a 500 $\mu$m diameter and a circular-shaped steel ring serves as the cathode and anode, respectively. These electrodes are connected to a Kepco BOP 4000 W DC power amplifier. The amplifier's input is supplied from the output of a Digital to Analog (DAC) converter channel from dSPACE. The electrical parameters (Voltage, period, duty cycle, and signal shape) are provided through ControlDesk using custom-designed blocks in Simulink.

Tool displacement is monitored using an optical sensor that tracks the tool shaft's movement held by a flexible structure in the machine head. This displacement is rep-

resented by voltage signals and transmitted through a data interface unit connected to dSPACE and XPS motion controller. Changes in forces on the tool are detected through a voice coil actuator in the machine head, and the resulting signals are sent to the XPS motion controller as feedback during machining. The primary code is written in TCL scripting language and executed in the XPS software interface, determining parameters such as feed rate, machining depth, hole coordinates, and other supplementary parameters. Additional support codes are created in Simulink blocks and are visually monitored through ControlDesk. To ensure safety for both the machine and the operator, protective bellows and acrylic panels are employed and a fume exhaust system is used to remove fumes from the machining area. A schematic of the setup is shown in Fig. 5.2.



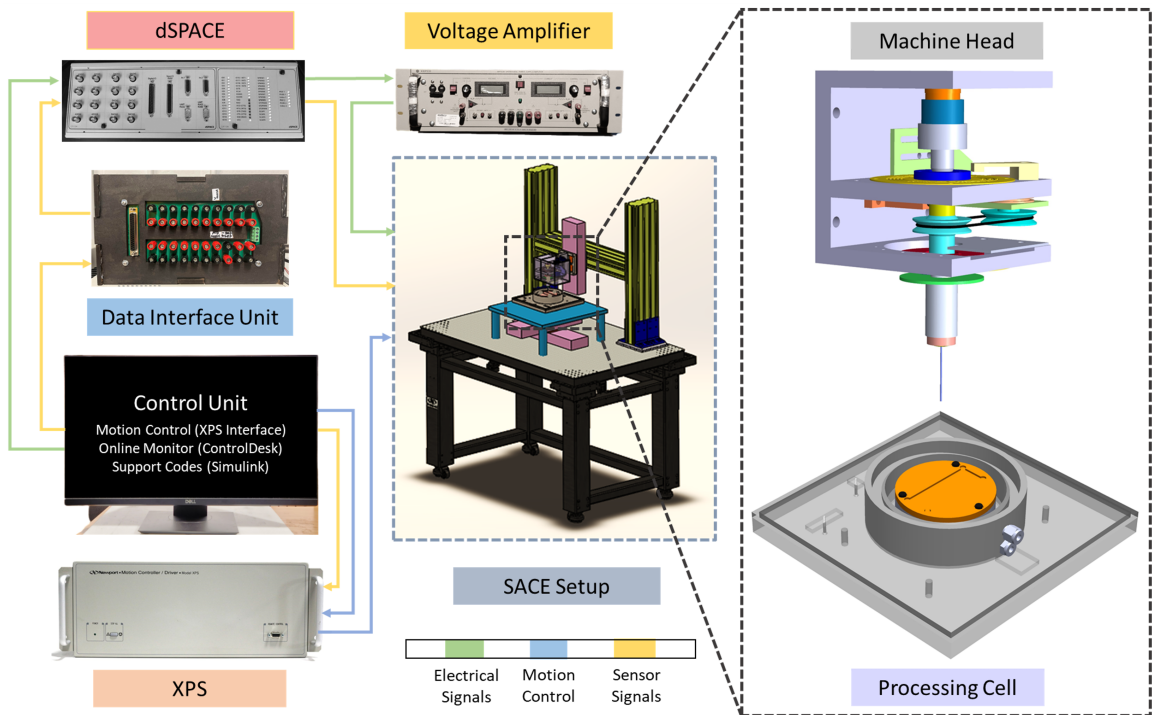Figure 5.2: Schematic of the SACE setup.

The drilling routine utilized in this study employs the force feedback method. In the event of forces detected from tool-workpiece contact, the tool ascends to sustain a machining gap. A flowchart outlining the machining routine logic is presented in Fig. 5.3.
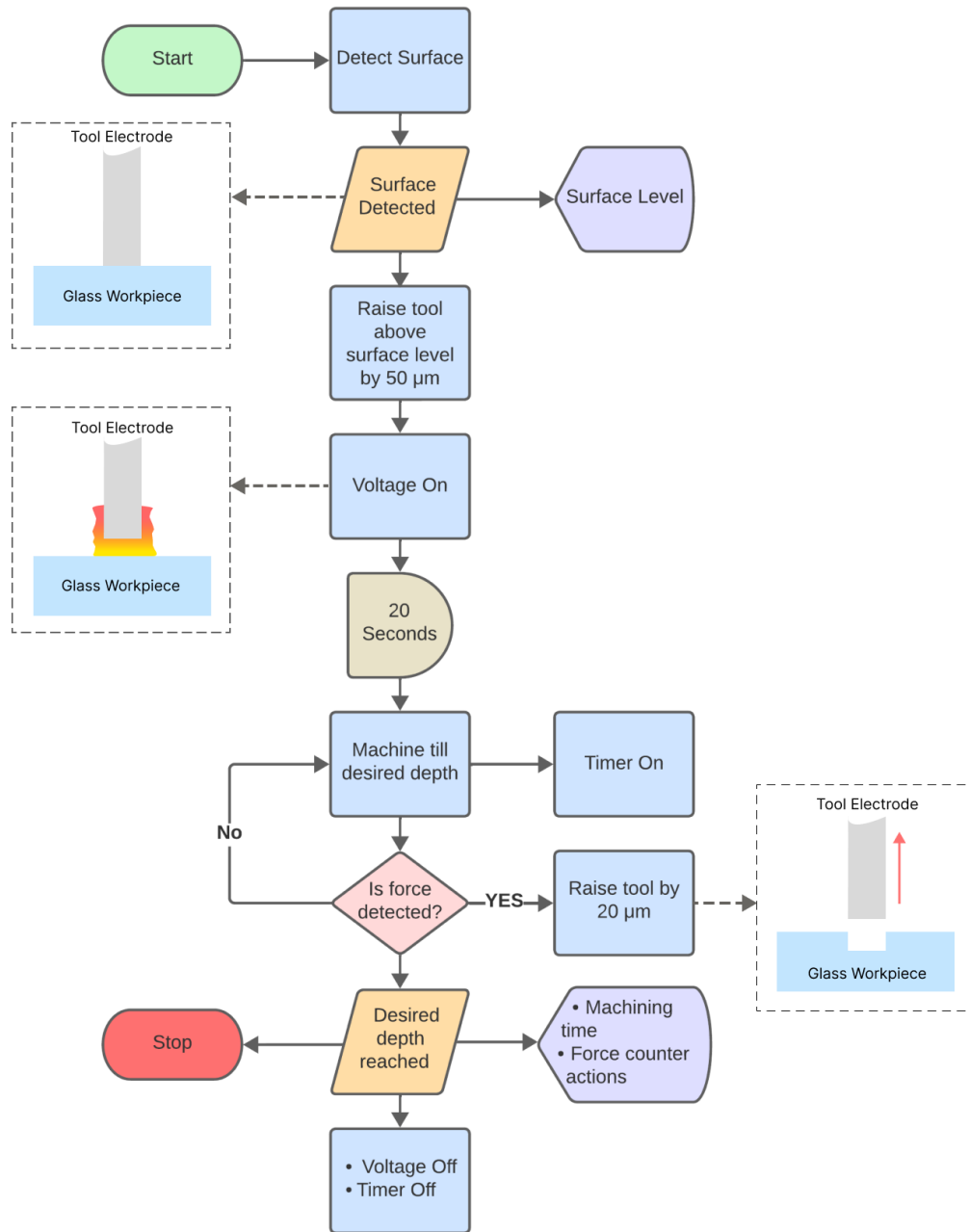


Figure 5.3: Flowchart diagram of machining routine logic employed in the machining experiments.

## 5.3 Machining Analysis

Four characteristics were chosen to assess machining quality. The first, machining time, monitored process efficiency and was measured using the routine outlined in Section 5.2. The second characteristic evaluated hole accuracy by measuring the hole overcut. The remaining characteristics, primarily addressing hole quality, involve measurements for hole taper and circularity. A KEYENCE VHX-1000 digital microscope was used to acquire the requisite values for calculating these response variables. Equations 5.1, 5.2, and 5.3 were used in the calculation process.

$$\text{Hole Overcut} = \frac{\text{Top Hole}\,\Phi + \text{Bottom Hole}\,\Phi}{2} - \text{Nominal Hole}\,\Phi\,(500\,\mu\text{m}) \qquad (5.1)$$

$$\text{Taper Angle} = \tan^{-1}\left(\frac{\text{Top hole}\,\Phi - \text{Bottom hole}\,\Phi}{\text{Hole depth}}\right) \qquad (5.2)$$

$$\text{Circularity} = \left(1 - \frac{\text{Circularity Error}}{\text{Top Hole}\,\Phi}\right) \times 100 \qquad (5.3)$$

Where,

*Circularity error = Maximum top hole $\Phi$ – Average Top hole $\Phi$*

*$\Phi$ = Diameter ($\mu m$)*

A summarized experimental design, along with corresponding quality characteristics, is provided in Table 5.2. Each run was machined three times, and the average response variables obtained from these trials constituted the final quality characteristics.

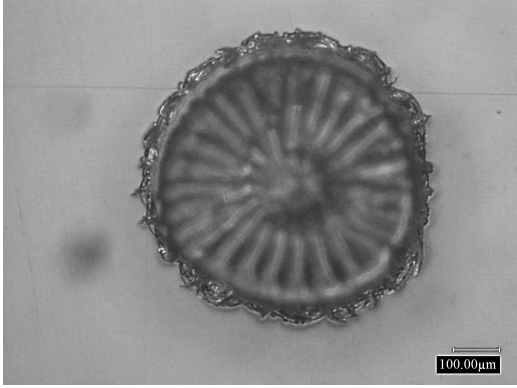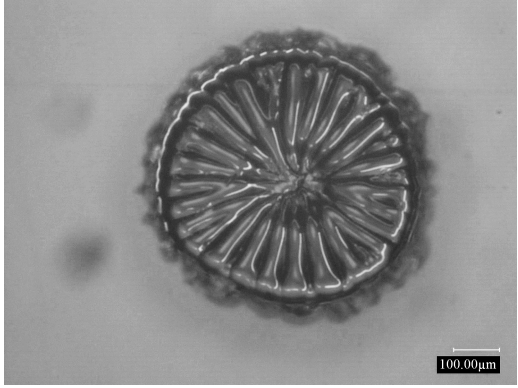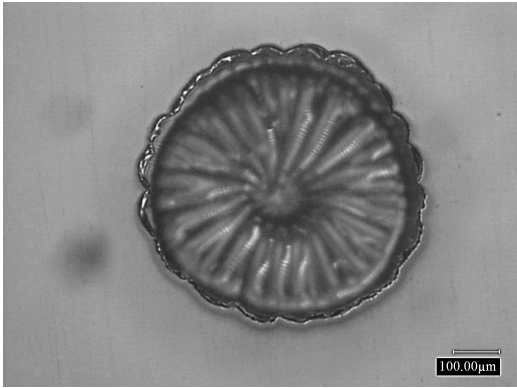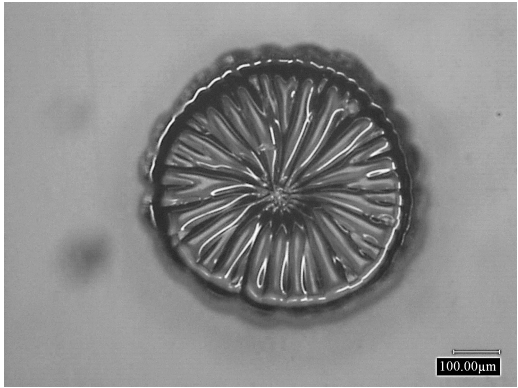Table 5.2 Design of experiments with the response variables.
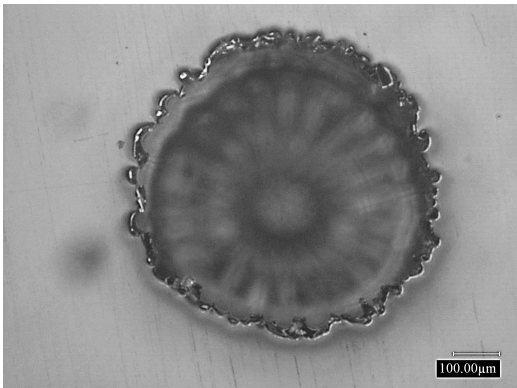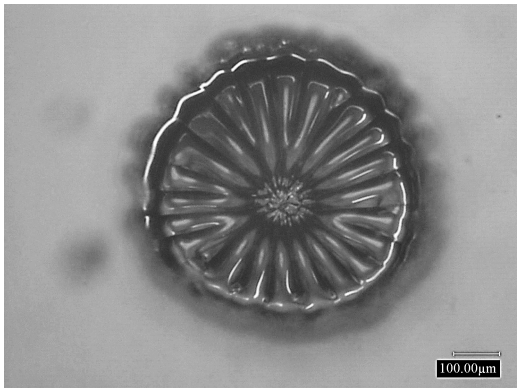
| Input process parameters | | | | Response Variables | | | |
|---|---|---|---|---|---|---|---|
| Runs | A | B | C | Avg, $Y_1$ | Avg, $Y_2$ | Avg, $Y_3$ | Avg, $Y_4$ |
| | - | - | (µm) | (s) | (°) | (µm) | (%) |
| 1 | KOH 50 wt% | Pulse | 100 | 65 | 38 | 65 | 77 |
| 2 | KOH 50 wt% | Sinusoidal | 100 | 136 | 26 | 57 | 89 |
| 3 | KOH 50 wt% | Pulse | 300 | 318 | 15 | 101 | 81 |
| 4 | KOH 50 wt% | Sinusoidal | 300 | 463 | 18 | 92 | 90 |
| 5 | NaOH 30 wt% | Pulse | 100 | 71 | 39 | 90 | 90 |
| 6 | NaOH 30 wt% | Sinusoidal | 100 | 103 | 39 | 103 | 97 |
| 7 | NaOH 30 wt% | Pulse | 300 | 142 | 20 | 141 | 86 |
| 8 | NaOH 30 wt% | Sinusoidal | 300 | 327 | 14 | 148 | 92 |

A = Electrolyte type ; B = Applied signal ; C = Period (µm) ; $Y_1$ = Machining time (s) ; $Y_2$ = Hole taper angle (°) ; $Y_3$ = Hole overcut (µm) ; $Y_4$ = Circularity (%).

## 5.3.1   Effect of electrolyte on hole quality

After analyzing the quality characteristics, it is evident that employing the KOH 50 wt% electrolyte results in higher accuracy and lower hole taper values due to its low viscosity, aligning with the findings in Chapter 4. However, this choice results in a feathery surface texture because of Potassium Hydroxide's chemical nature. Conversely, using NaOH 30 wt% results in smoother surfaces, which can be advantageous for applications requiring a polished finish. However, this comes at the expense of higher hole overcut due to its higher viscosity resulting in thicker gas films. The incorporation of effective methods that utilize hydrodynamic fluxes, such as higher electrolyte flow rate or tool rotation, could make the use of NaOH 30 wt% advantageous without compromising hole accuracy. While the overall machining rates tended to favor NaOH 30 wt%, it is crucial to note that these rates are influenced by various SACE parameters in addition to the type of electrolyte. Table 5.3 shows the top and bottom hole features of the machined holes.

Table 5.3 Top and bottom hole features.

| Top hole Feature | Bottom Hole Feature |
| --- | --- |
| 1.   KOH 50 wt% ; 100 µm depth ; Pulse | |



Φ604 µm
Φ525 µm

2.   KOH 50 wt% ; 100 µm depth ; Sinusoidal



Φ578 µm
Φ532 µm

3.   KOH 50 wt% ; 300 µm depth ; Pulse



Φ641 µm
Φ555 µm

| Top hole Feature | Bottom Hole Feature |
| --- | --- |

4. KOH 50 wt% ; 300 µm depth ; Sinusoidal



Φ634 µm



Φ538 µm

5. NaOH 30 wt% ; 100 µm depth ; Pulse



Φ631 µm



Φ549 µm
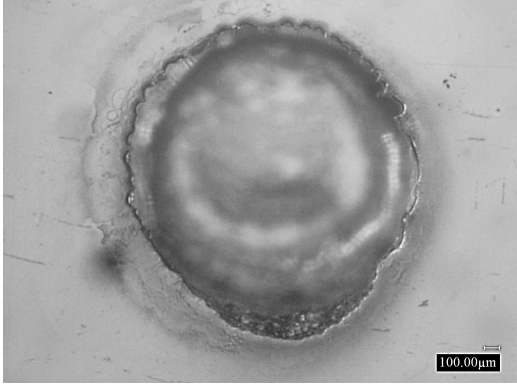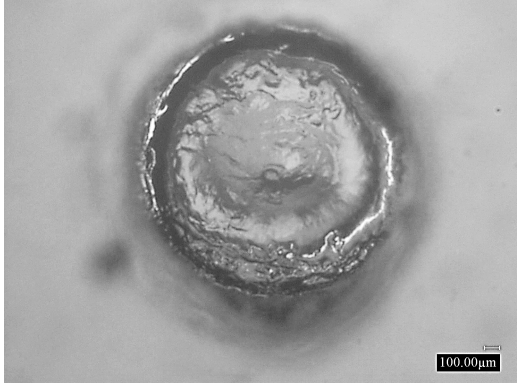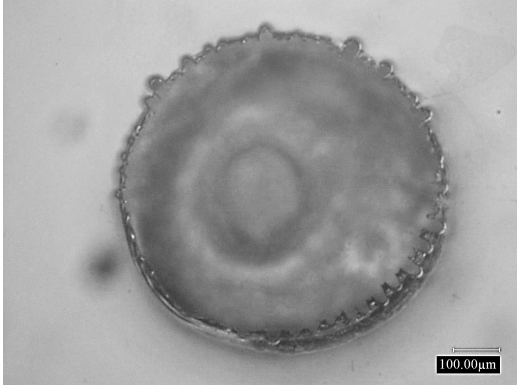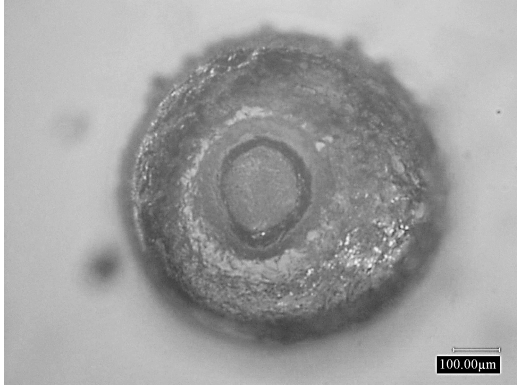
6. NaOH 30 wt% ; 100 µm depth ; Sinusoidal



Φ654 µm



Φ552 µm

| Top hole Feature | Bottom Hole Feature |
|:---:|:---:|

7.     NaOH 30 wt% ; 300 µm depth ; Pulse



| Φ699 µm | Φ609 µm |
|:---:|:---:|

8.     NaOH 30 wt% ; 300 µm depth ; Sinusoidal



| Φ686 µm | Φ617 µm |
|:---:|:---:|

## 5.3.2    Effect of signal shapes on hole quality

The choice of signal shape significantly affects the quality characteristics of the machined holes. For KOH 50 wt% electrolyte, holes drilled at a shallow depth (100 µm) using sinusoidal signals demonstrate a 32% reduction in hole taper, a 12% decrease in hole overcut, and a 16% enhancement in circularity compared to the pulse signals. For holes drilled at a greater depth (300 µm) using the same electrolyte, both signal shapes display an overall reduction in accuracy namely the hole overcut with an enhancement in hole quality namely the hole taper and circularity. Compared to the pulse signal, the sinusoidal signal shows a 9% improvement in hole overcut, similar hole circularity, and a 20% increase in hole taper. In general, the pulse signals

exhibit faster machining times, with the sinusoidal signals displaying an average 77% increase in machine time. The improvement in hole quality when using sinusoidal signals indicates a thinner and better-controlled gas film compared to the gas films formed by pulse signals, supporting the outcomes of the characterization experiments in Chapter 4. However, this comes with increased machining time due to the lower discharge energy of the sinusoidal signals.

When considering holes drilled using NaOH 30 wt%, similar trends are observed compared to those seen in the analysis of holes drilled using the KOH 50 wt% electrolyte. For the sinusoidal signal, the most notable improvement is in hole circularity, which increased by 9% compared to the pulse signal. Other quality characteristics displayed comparable outcomes, while the machining time of the sinusoidal signal exhibited a significant average increase of 88% for both depths. Therefore, any recommendation to apply sinusoidal signals in the SACE process should strike a balance between time and quality characteristics. As machining time increases (Beyond 400 seconds), the advantageous hole qualities of sinusoidal signals tend to diminish, as shown by the outcomes of holes drilled at deep depth (300 µm). In conclusion, the utilization of sinusoidal signals as opposed to pulse signals demonstrates significant enhancement in hole circularity and minor improvements in other qualities, at the expense of increased machining times. Fig. 5.4 presents a comparative summary of all the signal attributes evaluated in this study.
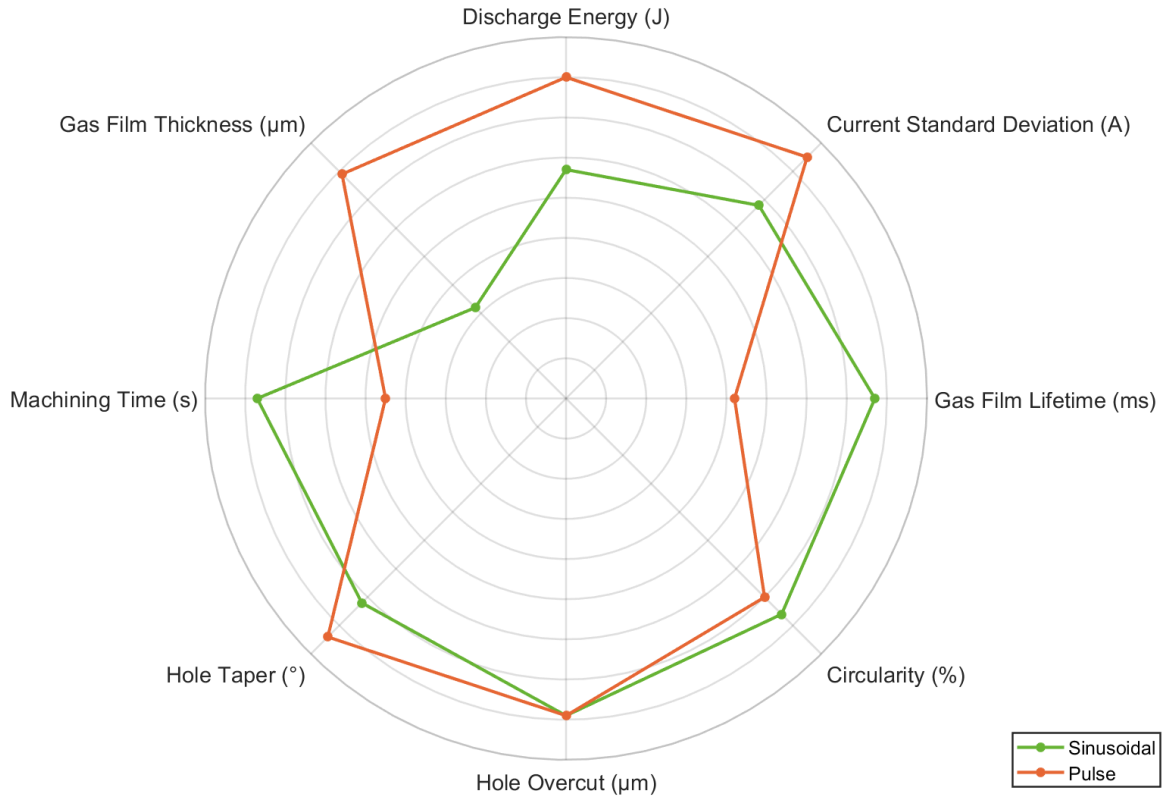
Figure 5.4: Evaluation of Pulse and Sinusoidal shape attributes in the study. Attributes normalized on a scale from 0 to 10. Center of the circle indicates zero, while the outer edge signifies 10.

## 5.4 Signal Enhancement

The analysis of the machining experiment outcomes confirms that altering the signal shape has an impact on the SACE process, an aspect that hasn't been thoroughly explored compared to other SACE parameters in literature. Upon reviewing the experiment results, it's evident that employing sinusoidal signals demonstrated enhancements in certain hole quality characteristics, particularly in hole taper, and circularity, thus improving machining accuracy. However, these enhancements are accompanied by longer machining times.

To overcome this drawback, the proposed signals require further enhancement in their shape design to provide a better trade-off between machining accuracy and time. The required signals would need to emulate the fundamental shapes of the proposed

signals that impart them with their unique attributes, while also creating a more favorable environment that allows for increased discharging activity. The proposed modification of the signal involves utilizing hybrid forms of the Sinusoidal signal in addition to the Triangle signal, that displayed similar qualities to the sinusoidal signal with an increase in mean discharge energy (See Fig. 5.5).
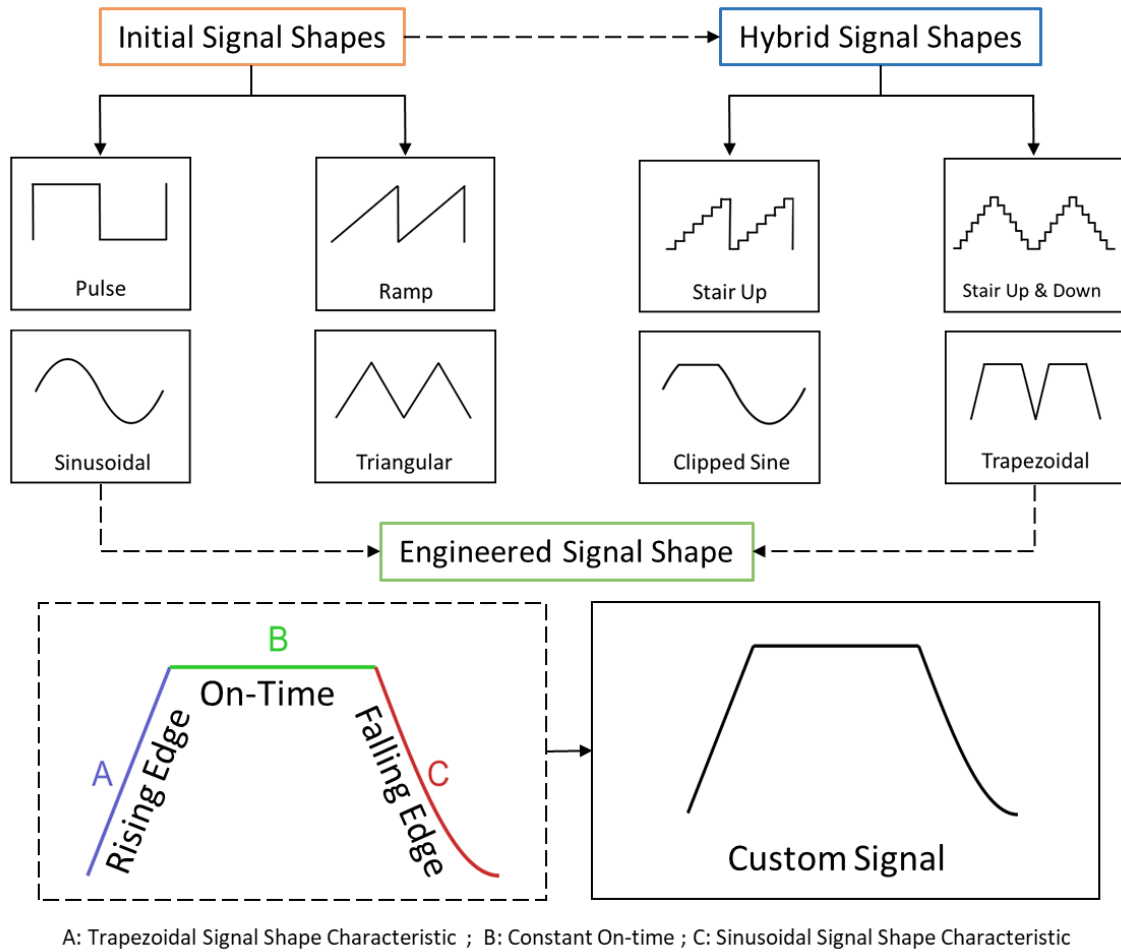


Figure 5.5: Visualization of the hybrid signal shapes and proposed engineered custom signal with a triangle rising edge, pulse on-time and sinusoidal falling edge.

The proposal also includes the design of a custom signal based on the outcomes of the analyses conducted throughout this study. The custom signal combines the advantageous rising edge of the triangle signal, allowing for a gradual voltage increase, with the pulse signal's on-time edge, which maintains a constant high voltage above the critical voltage, hence resulting in more discharges. Additionally, it incorporates

the favorable falling edge of the sinusoidal signal that enhances the gas film lifetime. The engineered signal's characteristics are illustrated in Fig 5.5.

Since the characterization and machining studies were completed successfully with established correlations, a three-step filtering process was employed to assess the proposed signals deserving further investigation. The initial step involved evaluating the signal processing parameters—Discharge mean energy, discharge current standard deviation, mean energy—using the gas film study outlined in Chapter 4. Only the clipped sine, trapezoidal, and custom signal shapes demonstrated comparable or improved outcomes. On the contrary, the step shapes of the stair up and stair up & down signals proved unsuitable and were subsequently excluded. Following this, the qualified signal shapes were analyzed for gas film thickness using the methods outlined in Section 3.6.1. The analysis of gas film thickness revealed that the custom signal shape displayed the lowest gas film thickness, depicted in Fig. 5.6.

## Clipped sin signal



617 um
693 um
618 um

t = 71 µm

500 µm

## Trapezoidal signal



598 um
673 um
701 um

t = 79 µm

500 µm

## Custom signal



683 um
578 um
628 um

t = 65 µm

500 µm
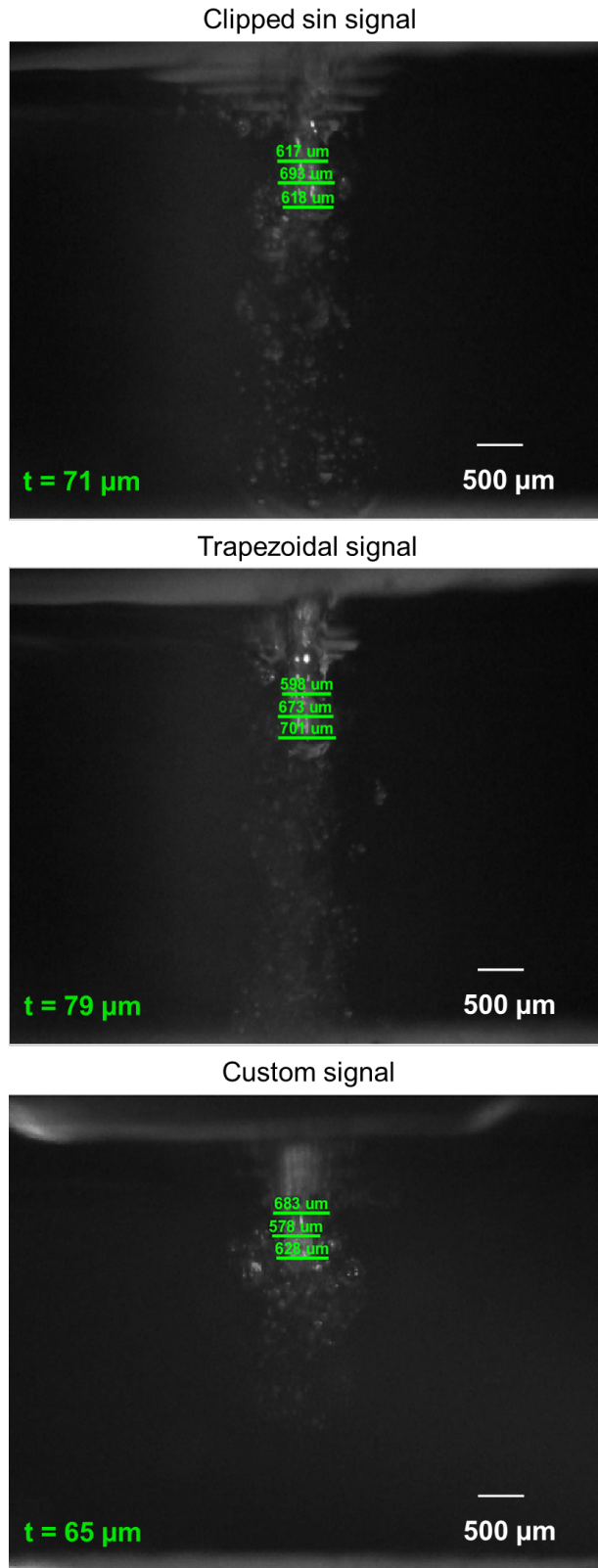
Figure 5.6: Gas film thickness for Clipped Sine, Trapezoidal, and Custom signal.

The custom signal was subsequently utilized in the SACE setup for machining applications. The resulting machining outcomes of the custom signal, compared to the pulse and sinusoidal signals, are illustrated in Fig. 5.7.
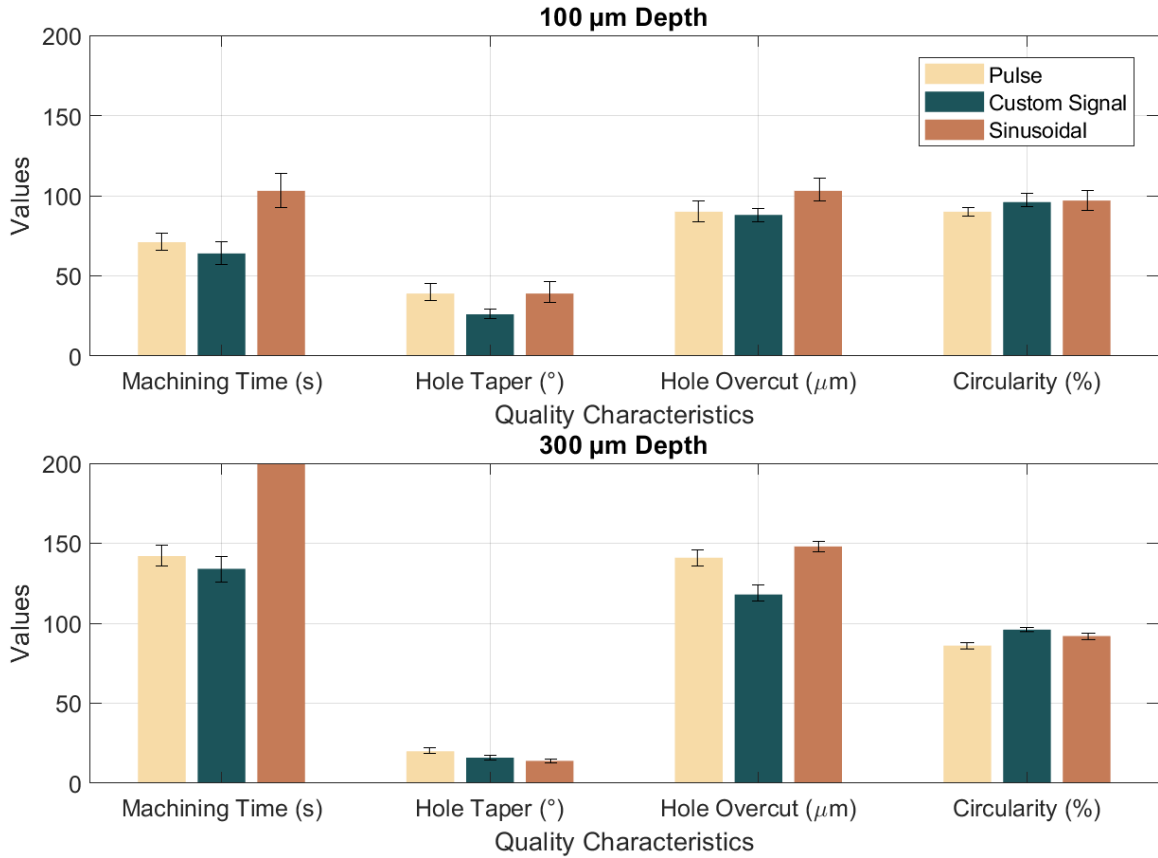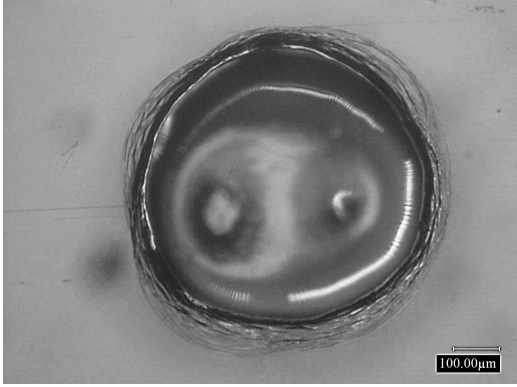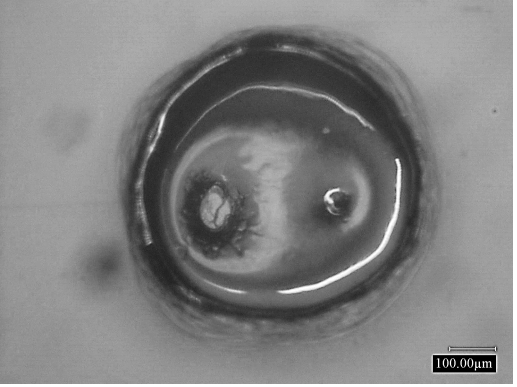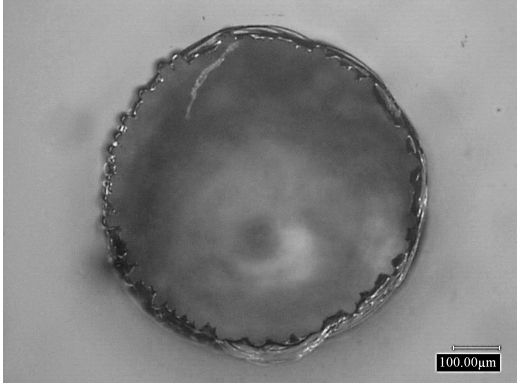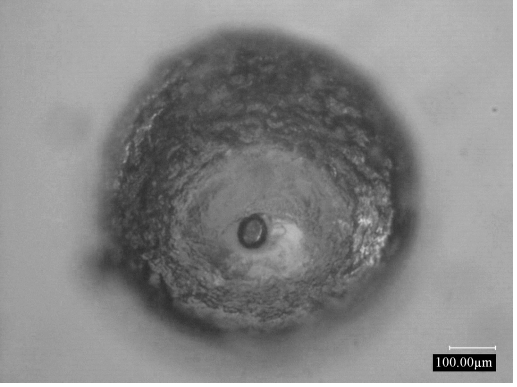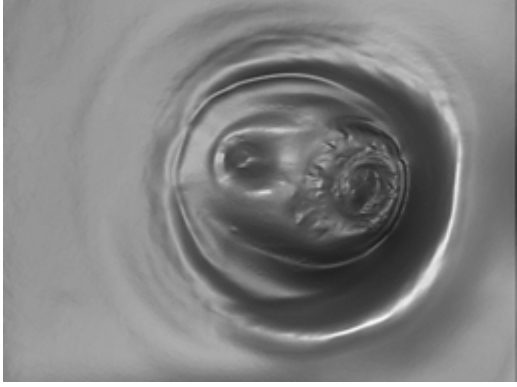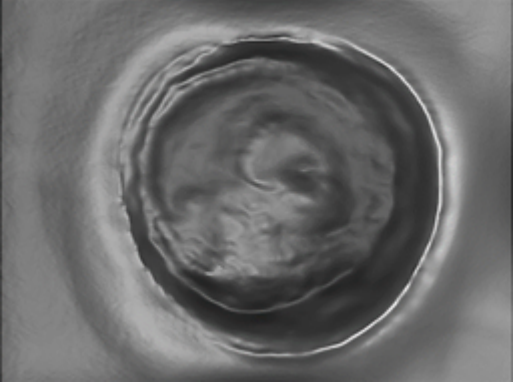


Figure 5.7: Quality Characteristics of Pulse, Custom Signal, and Sinusoidal Signal using 30% NaOH Electrolyte.

The machining outputs of the custom signal at a depth of 100 µm indicated significant improvements in machining time, showing a 10% reduction compared to the pulse signal and a remarkable 60% reduction compared to the sinusoidal signal. Regarding hole quality, the custom signal displayed a 33% reduction in hole taper compared to other signal shapes. Additionally, it exhibited similar hole overcut as the pulse signal and a 17% enhancement over the sinusoidal signal. In terms of hole circularity, the custom signal presented a 7% improvement over the pulse signal and a similar outcome as the sinusoidal signal, which displayed the highest circularity. Similar trends

were observed for holes drilled at a depth of 300 µm, with only the custom signal slightly lagging behind the sinusoidal signal in hole taper by 13%. Given this analysis, recommending the custom signal for machining applications seems suitable due to its balanced machining time outcome and improved hole quality.

To conclude this analysis, the custom signal demonstrates enhanced control over the gas film, close to the outputs of the sinusoidal signal. Furthermore, the adjustments to its shape promote its application in machining compared to the pulse signal, the widely used signal in SACE. Table 5.4 presents the top and bottom features of the holes machined with the custom signal. Additionally, a PhaseView 3D optical profiler was utilized to obtain a comprehensive 3D image of the holes, providing a detailed view of the holes drilled using the custom signal.

Table 5.4 Hole features machined using the custom signal.

| Top Hole Feature | Bottom Hole Feature |
|---|---|

1. NaOH 30 wt% ; 100 µm depth ; Custom Signal



Φ600 µm                                    Φ552 µm

2. NaOH 30 wt% ; 300 µm depth ; Custom Signal



Φ670 µm                                    Φ555 µm

3. 3D Images of the holes drilled using the Custom Signal



100 µm depth                              300 µm depth

## 5.5 Electrolyte Enhancement

In line with the previous discussion in Section 2.3.3, the inclusion of wetting agents, or surfactants further enhance the quality of SACE machining, particularly in terms of surface quality and machining time. This improvement in surface quality can be attributed to surfactants' influence on the electrolyte composition, leading to a reduction in the critical voltage and consequently affecting electrical parameters as well [88]. Conversely, the decrease in machining time can be linked to the rise in current density resulting from the inclusion of surfactants in the electrolyte. The following section provides an overview of the nature of surfactants and explores their influence on the machining output with respect to the proposed signals.

### 5.5.1 Surfactant theory

Surface active agents, commonly referred to as surfactants, find applications in various chemical industries, including the production of detergents and the separation of DNA. Their unique ability to alter the properties of chemical solutions, especially their capacity to reduce surface tensions, makes them valuable in these contexts. Surfactants consist of two main components: a polar part and an apolar part. The polar portion includes a hydrophilic head, while the apolar portion comprises a hydrophobic tail, typically constructed from a string of carbon atoms. The hydrophilic head exhibits a strong affinity for polar solvents like water.

In dilute solutions, surfactant molecules exist as monomers. At specific surfactant concentrations, monomers accumulate and form micelles, which are aggregates of molecules. The critical micelle concentration (CMC) is the concentration at which micelles start forming. Beyond the CMC, the only active surfactant monomers are those existing at the interface. The micelles serve as an inactive reservoir of monomers, and this results in abrupt variations in the physicochemical properties of the solution, including electrical and thermal conductivity, surface tension, viscosity, and more [89].

Fig. 5.8 illustrates the impact of surfactant concentration on system properties and includes a schematic depiction of micelle formation.
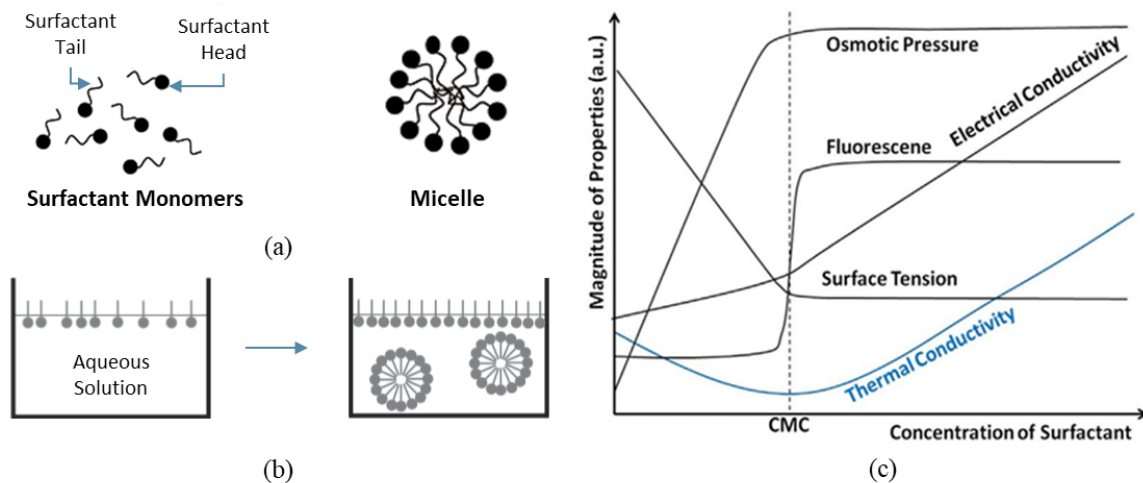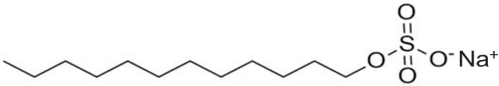


Figure 5.8: (a) Surfactant characteristics. (b) Micelle formation. (c) Effect of surfactant concentration on properties.

## 5.5.2 Surfactant Methodology

In the presented study, the chosen surfactant is sodium dodecyl sulfate (SDS), one of the most commonly used surfactants in SACE. Table 5.5 provides an overview of SDS's properties. A 50% KOH solution was prepared using the same procedure outlined in Section 3.3.1. Past research has indicated that the addition of surfactants at the critical micelle concentration (CMC) of 0.236 wt% yields the most significant property enhancements [43]. However, due to the high electrolyte concentration, the CMC point tends to decrease because of the high base salt concentration (50 wt%) in the electrolyte.

Table 5.5 The properties of SDS.

| | SDS |
|---|---|
| Chemical formula | $CH_3(CH_2)_{11}OSO_3Na$ |
| Molar Mass | 288.38 $g/mol$ |
| PH | 6-7.5 |
| Structure |  |
| Appearance | White solid |
| Solubility in 25°C | 0.0082 M |
| CMC | 0.236 wt% |

To determine the optimum surfactant concentration, a range of SDS concentrations was explored, beginning at the CMC point of SDS, as shown in Fig. 5.9. Concentrations gradually decreased until there was a minimal excess of SDS present in the electrolyte, indicated by the absence of a white precipitate. To ensure proper mixing of SDS with the electrolyte, the mixture was heated to 50 °C and stirred at 800 rpm for 45 minutes. The benchmark for the ideal SDS concentration was established based on the concentration that produced the most significant reduction in critical voltage with minimal to no precipitates in the electrolyte. The critical voltage was determined using the methods detailed in Section 3.5.

The addition of SDS in SACE leads to a decrease in the electrolyte's surface tension by mitigating the bonding forces between its molecules. Furthermore, SDS ionizes in the electrolyte, enhancing the number of anions and cations in the solution, consequently increasing the current flow between the cathode and anode and, consequently, the electrical conductivity of the electrolyte [42]. This, however, results in a decrease in the thermal conductivity of the electrolyte, which affects the cooling rate of glass workpieces during the SACE process [90].

| Electrolyte | Critical Current (A) | Critical Voltage (V) |
|---|---|---|
| 50 wt% KOH + 0.236 wt% SDS | 2.37 | 17.46 |
| 50 wt% KOH + 0.1 wt% SDS | 2.01 | 16.6 |
| 50 wt% KOH + 0.05 wt% SDS | 2.04 | 16.8 |
| 50 wt% KOH + 0.02 wt% SDS | 1.23 | 15.1 |
| 50 wt% KOH | 2.73 | 22.4 |
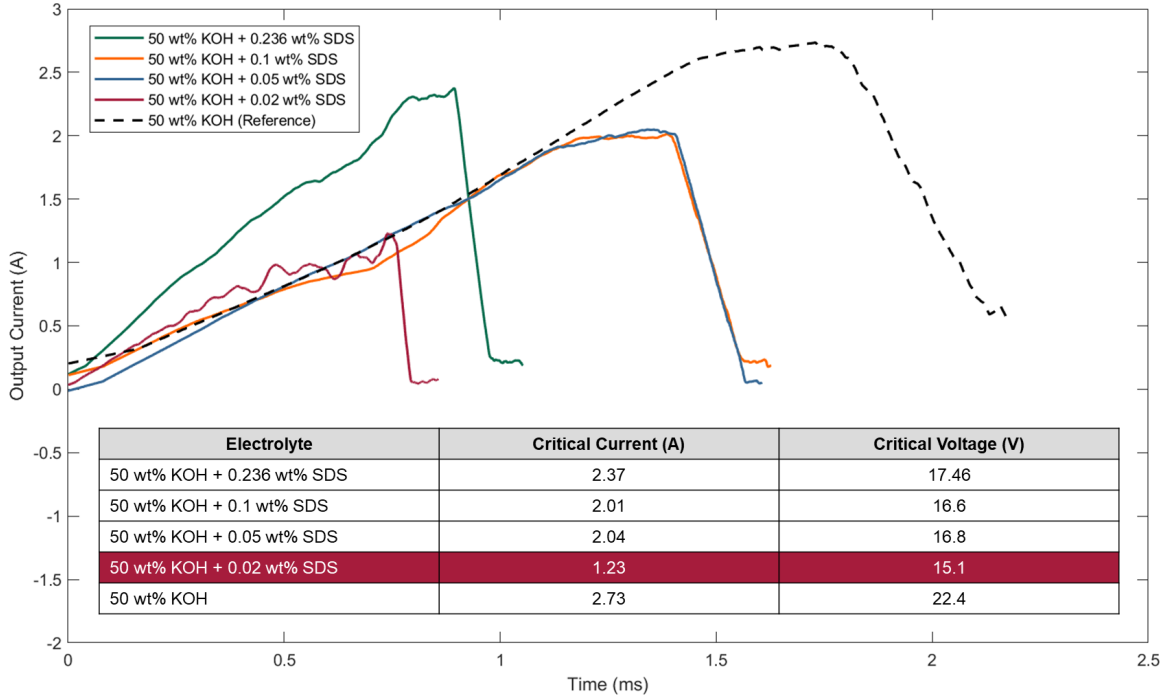
Figure 5.9: Analysis of SDS concentrations in 50 wt% KOH electrolytes. A 0.2% SDS concentration yielded the greatest reduction in critical voltage.

### 5.5.3 Surfactant Machining Output

To explore the combined effect of signal shapes and surfactants on machining outcomes, holes were machined at a depth of 100 µm using a solution of 50 wt% KOH + 0.2 wt% SDS, employing sinusoidal, pulse, and custom signals. Unexpectedly, the results revealed a sharp decline in hole quality when compared to holes machined using 50% KOH with the sole enhancement seen in hole circularity (See Fig. 5.10). Although literature has shown that surfactant use can enhance the quality of machined holes, yet leveraging this advantage necessitates adjustments in various SACE parameters. In order to do so, further investigations are needed as changing the initially determined parameters would impede a comparative analysis between this study and other machining studies conducted. For this reason, investigations on the combined effect signal shapes and surfactants were halted.
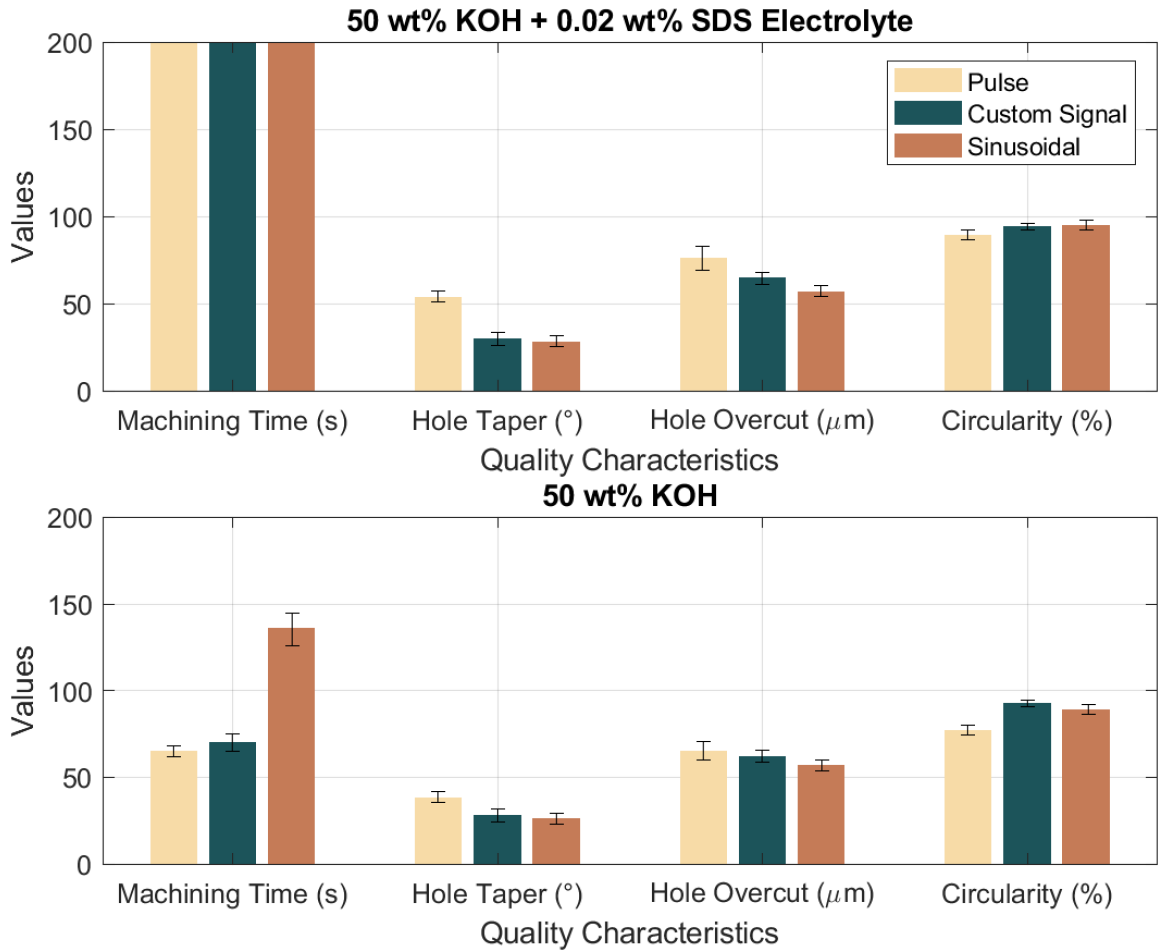
Figure 5.10: Hole quality characteristics machined using 50 wt% KOH + 0.02 wt% SDS and 50 wt% KOH Electrolyte.

## 5.6   Chapter Summary

In Chapter 4, the impact of modifying signal shapes to enhance gas film quality was evaluated through signal processing and visual assessment of the gas film. The subsequent study in this chapter aimed to corroborate these findings and establish correlations between the response outputs identified in the characterization experiments and the actual machining results. This study mainly concentrated on assessing the performance of the sinusoidal signal in contrast to the pulse signal, the widely employed signal in SACE literature. The study utilized a SACE setup to drill holes at depths of 100 µm and 300 µm, evaluating efficiency and quality characteristics. In addition, avenues for improving the machining characteristics were explored through

enhancing the signal shape and electrolyte of use. From the experimental results, the following conclusions are drawn:

- KOH 50 wt% resulted in a feather-like texture with improvements in hole overcut and taper, while NaOH 30 wt% produced a smooth surface with enhanced machining time.

- The improvements in hole quality when using sinusoidal signals indicate a thinner and better-controlled gas film compared to the gas films formed by pulse signals, validating the outcomes of Chapter 4.

- The use of sinusoidal signals compared to pulse signals demonstrates improvements in hole taper, and circularity at the expense of increased machining times.

- To overcome this drawback, a study involving hybrid signal shapes of the pulse, sinusoidal and triangle signals was conducted to find a better trade-off between machining quality and efficiency however, the hybrid signals didn't show any significant improvement.

- A custom signal was designed, based on the characterization and machining experiments analyses, combining the advantageous rising edge of the triangle signal with the pulse signal's on-time edge and the favorable falling edge of the sinusoidal signal that enhances the gas film lifetime.

- The custom signal showed enhanced control over the gas film, close to the quality outputs of the sinusoidal signal. In addition, the efficiency outputs of the custom signal promote its application in SACE.

- An attempt to further enhance the machining outcomes was done through adding sodium dodecyl sulfate (SDS) to 50 wt% KOH and adjusting the electrical parameters according to the critical voltage of the electrolyte. The results

revealed a sharp decline in hole quality when compared to holes machined using 50% KOH with the sole enhancement seen in hole circularity.

# Chapter 6

# Conclusion and Outlook

SACE has shown potential as a method for machining glass micro-parts and devices. However, the intricate control requirements related to the gas film surrounding the tool electrode pose a significant challenge in SACE applications. While several studies have explored the influence of SACE parameters on the gas film, there exists a literature gap regarding the impact of signal shapes on this film. The stability of the gas film is critical for ensuring consistent machining outcomes. The instability of the gas film has, in many ways, limited the industrial applications of SACE. This thesis aimed to examine various voltage signal shapes, designed to maintain the gas film's presence around the tool.

Due to the lack of a clear correlation between gas film properties and machining performance, the study initially focused on quantifying the physical and dynamic properties of the gas film. After establishing a robust methodology for correlating these properties, the research investigated how different signal shapes influenced gas film behavior and interacted with other crucial SACE parameters. The subsequent phase involved applying these findings to a machining application to establish connections between signal shapes and machining outcomes. Finally, the thesis assessed the proposed signal shapes and explored potential avenues for further enhancement. The main contributions of the thesis are as follows:

■ **A robust methodology for evaluating the gas film:** A method was developed to classify SACE process feedback current signals through recordings of corresponding gas film dynamics using a high-speed camera, allowing for correlation analysis. The experimental outcomes were subjected to statistical techniques to assess the gas film properties of interest.

■ **Signal shapes to maintain the gas film's presence:** This study resulted in enhancements in gas film thickness and discharge control. The combined effect of the signal shape design and sinusoidal signal shape notably increased gas film lifetime, reaching durations of up to 35 ms.

■ **The combination of signal shapes and SACE parameters:** A multi-objective optimization study established the most ideal process parameters, compromising KOH 50 wt% electrolyte, sinusoidal signal, and 90% on-time. The gas film thickness was evaluated using a high-speed camera and the findings confirmed the outputs of the multi objective study.

■ **Application of the gas film study findings to machining applications:** The use of sinusoidal signals demonstrated improvements in hole taper, and circularity at the expense of increased machining times. These enhancements indicated the presence of a thinner gas film accompanied by controlled discharges.

■ **Potential avenues for further enhancing the machining output:** A custom signal was designed based on the analyses of the characterization and machining experiments. The efficiency outputs of the custom signal coupled with its enhancements in hole quality promote its further application in SACE.

This study advances the understanding of SACE, providing valuable insights into gas film control and its impact on machining quality and efficiency. While addressing these aims, the findings also pinpoint areas for further exploration:

- Investigating the collective impact of signal shapes with various tool parameters—such as tool shape, rotation, and feed rate—may lead to much improved outcomes.

- A comprehensive study involving the custom signal across a wider range of machining applications could further fortify the findings of this study and establish a solid benchmark for this signal shape.

- Exploring the combined effects of surfactants and signal shapes could potentially yield further improvements. Parameters used in this study were not optimal for this purpose.

- Establishing an efficient method to evaluate temperature fluctuations during the SACE process would deepen the understanding of this process.

- Electrolyte circulation significantly impacts machining quality. An exploration into enhanced circulation methods could bolster SACE competitiveness in micro-glass industries.

- Expanding on the methodology and findings of this thesis, further exploration of gas film fluid dynamics in SACE using methods such as computational fluid dynamics (CFD) could potentially discover novel insights into gas film behavior.

# Bibliography

[1] Z. Jiang, J. Zhao, and H. Xie, *Microforming technology: theory, simulation and practice*. Academic Press, 2017.

[2] V. Tielen and Y. Bellouard, "Three-dimensional glass monolithic micro-flexure fabricated by femtosecond laser exposure and chemical etching," *Micromachines*, vol. 5, no. 3, pp. 697–710, 2014.

[3] Y. Aishan, Y. Yalikun, and Y. Tanaka, "Pneumatically actuated thin glass microlens for on-chip multi-magnification observations," in *Actuators*, MDPI, vol. 9, 2020, p. 73.

[4] A. Shorey and et al., "IMAPS 2019 - 52nd international symposium on microelectronics," in *IMAPS 2019 - 52nd International Symposium on Microelectronics - Boston, MA USA - Sep. 30-Oct. 3, 2019*, 2019.

[5] G. C. Righini and N. Righini, *Editorial for the special issue on glassy materials based microdevices*, 2019.

[6] A.-G. Niculescu, C. Chircov, A. C. Bîrcă, and A. M. Grumezescu, "Fabrication and applications of microfluidic devices: A review," *International Journal of Molecular Sciences*, vol. 22, no. 4, p. 2011, 2021.

[7] B. Guo, M. Wu, Q. Zhao, H. Liu, and J. Zhang, "Improvement of precision grinding performance of cvd diamond wheels by micro-structured surfaces," *Ceramics International*, vol. 44, no. 14, pp. 17 333–17 339, 2018.

[8] L. A. Hof, "High-precision micro-machining of glass for mass-personalization," Ph.D. dissertation, Concordia University, 2018.

[9] S. Z. Chavoshi and X. Luo, "Hybrid micro-machining processes: A review," *Precision Engineering*, vol. 41, pp. 1–23, 2015.

[10] Z. Bassyouni and J. D. Abou Ziki, "The capabilities of spark-assisted chemical engraving: A review," *Journal of Manufacturing and Materials Processing*, vol. 4, no. 4, p. 99, 2020.

[11] R. Wüthrich and J. D. Abou Ziki, *Micromachining using Electrochemical Discharge Phenomenon: Fundamentals and Application of Spark Assisted Chemical Engraving*. William Andrew, 2014.

[12] H. Karafuji and K. Suds, "Annals of CIRP," vol. 16, p. 415, 1968.

[13] N. Cook and et al., "Experimental studies in electro-machining," pp. 945–950, 1973.

[14] M. Kubota, "On the technological potentialities of ECDM," 1975.

[15] K. Allesu, A. Ghosh, and M. Muju, "A preliminary qualitative approach of a proposed mechanism of material removal in electrical machining of glass," *European Journal of Mechanical Engineering*, vol. 36, pp. 202–207, 1992.

[16] V. Fascio and et al., "3d microstructuring of glass using electrochemical discharge machining (ecdm)," in *MHS'99. Proceedings of 1999 International Symposium on Micromechatronics and Human Science (Cat. No. 99TH8478)*, IEEE, 1999.

[17] V. Jain, P. Dixit, and P. Pandey, "On the analysis of the electrochemical spark machining process," *International Journal of Machine Tools and Manufacture*, vol. 39, no. 1, pp. 165–186, 1999.

[18] H. Langen and et al., "Three-dimensional structuring of pyrex glass devices—trajectory control," in *Proceedings of the International Conference of the European Society for Precision Engineering and Nanotechnology (EUSPEN) 2, Eindhoven, The Netherlands, 26–30 May 2002*, 2002.

[19] S. Huang and et al., "Electrochemical discharge machining micro-hole in stainless steel with tool electrode high-speed rotating," *Materials and Manufacturing Processes*, vol. 29, no. 5, pp. 634–637, 2014.

[20] L. A. Hof and R. Wuthrich, "Glass precision micro-cutting using spark assisted chemical engraving," *Advances in Industrial and Manufacturing Engineering*, vol. 3, p. 100 056, 2021.

[21] Y. Pu and et al., "Micro-sace scanning process with different tool-surface roughness," *Materials and Manufacturing Processes*, vol. 35, no. 11, pp. 1181–1187, 2020.

[22] V. Rajput, M. Goud, and N. M. Suri, "Machinability study of spark assisted chemical engraving (sace): A state of art,"

[23] H. Hamed, M. Eldiasty, S.-M. Seyedi-Sahebari, and J. D. Abou-Ziki, "Applications, materials, and fabrication of micro glass parts and devices: An overview," *Materials Today*, 2023.

[24] L. A. Hof and R. Wüthrich, "Rapid prototyping of packaged glass devices: Eliminating a process step in the manufacturing workflow from micromachining to die singularizing," *Manufacturing Letters*, vol. 17, pp. 9–13, 2018.

[25] L. A. Hof and J. Abou Ziki, "Micro-hole drilling on glass substrates—a review," *Micromachines*, vol. 8, no. 2, p. 53, 2017.

[26] B. Bhattacharyya, B. N. Doloi, and S. K. Sorkhel, "Experimental investigations into electrochemical discharge machining (ecdm) of non-conductive ceramic materials," *Journal of Materials Processing Technology*, vol. 95, no. 1-3, pp. 145–154, 1999.

[27] R. Wüthrich and et al., "Spark assisted chemical engraving (sace) in microfactory," *Journal of Micromechanics and Microengineering*, vol. 15, no. 10, S276, 2005.

[28] R. Wüthrich, C. Comninellis, and H. Bleuler, "Bubble evolution on vertical electrodes under extreme current densities," *Electrochimica Acta*, vol. 50, no. 25-26, pp. 5242–5246, 2005.

[29] A. Kulkarni, R. Sharan, and G. K. Lal, "An experimental study of discharge mechanism in electrochemical discharge machining," *International Journal of Machine Tools and Manufacture*, vol. 42, no. 10, pp. 1121–1127, 2002.

[30] T. Singh and A. Dvivedi, "Developments in electrochemical discharge machining: A review on electrochemical discharge machining, process variants and their hybrid methods," *International Journal of Machine Tools and Manufacture*, vol. 105, pp. 1–13, 2016.

[31] V. Rajput, M. Goud, and N. M. Suri, "Performance analysis of ecdm process using surfactant mixed electrolyte," *Manufacturing Engineering: Select Proceedings of CPIE 2019*, 2020.

[32] R. Wüthrich and V. Fascio, "Machining of non-conducting materials using electrochemical discharge phenomenon—an overview," *International Journal of Machine Tools and Manufacture*, vol. 45, no. 9, pp. 1095–1108, 2005.

[33] M. L. Harugade, M. V. Kavade, and N. V. Hargude, "Effect of electrolyte solution on material removal rate in electrochemical discharge machining," *IOSR J. Mech. Civ. Eng*, vol. 5, pp. 1–8, 2013.

[34] P. Kumar Gupta, A. Dvivedi, and P. Kumar, "Effect of electrolytes on quality characteristics of glass during ecdm," *Key Engineering Materials*, vol. 658, pp. 141–145, 2015.

[35] V. Rajput, M. Goud, and N. M. Suri, "Finite element modeling for comparing the machining performance of different electrolytes in ecdm," *Arabian Journal for Science and Engineering*, vol. 46, pp. 2097–2119, 2021.

[36] K. R. Kolhekar and M. Sundaram, "A study on the effect of electrolyte concentration on surface integrity in micro electrochemical discharge machining," *Procedia CIRP*, vol. 45, pp. 355–358, 2016.

[37] B. Mallick and et al., "Experimental investigation for improvement of micro-machining performances of µ-ecdm process," *Materials Today: Proceedings*, vol. 27, pp. 620–626, 2020.

[38] J. B. Madhavi and S. S. Hiremath, "Investigation on machining of holes and channels on borosilicate and sodalime glass using -ecdm setup," *Procedia Technology*, vol. 25, pp. 1257–1264, 2016.

[39] S. Bellubbi, P. Gani, S. Nandikol, R. Patil, and M. BPatil, "Machining of conductive/non-conductive materials by hybrid machining,"

[40] N. K. Jain and V. K. Jain, "Optimization of electro-chemical machining process parameters using genetic algorithms," *Machining Science and Technology*, vol. 11, no. 2, pp. 235–258, 2007.

[41] Y. S. Laio, L. C. Wu, and W. Y. Peng, "A study to improve drilling quality of electrochemical discharge machining (ecdm) process," *Procedia Cirp*, vol. 6, pp. 609–614, 2013.

[42] R. Wüthrich and L. A. Hof, "The gas film in spark assisted chemical engraving (sace)—a key element for micro-machining applications," *International Journal of Machine Tools and Manufacture*, vol. 46, no. 7-8, pp. 828–835, 2006.

[43] N. Sabahi, M. R. Razfar, and M. Hajian, "Experimental investigation of surfactant-mixed electrolyte into electrochemical discharge machining (ecdm) process," *Journal of Materials Processing Technology*, vol. 250, pp. 190–202, 2017.

[44] C.-K. Yang and et al., "Effect of surface roughness of tool electrode materials in ecdm performance," *International Journal of Machine Tools and Manufacture*, vol. 50, no. 12, pp. 1088–1096, 2010.

[45] J. D. Abou Ziki and R. Wüthrich, "Tool wear and tool thermal expansion during micro-machining by spark assisted chemical engraving," *The International Journal of Advanced Manufacturing Technology*, vol. 61, pp. 481–486, 2012.

[46] S. Zhan and Y. Zhao, "Suppression of cathode tool wear by a forward-bias voltage in pulsed spark-assisted chemical engraving," *Electrochemistry Communications*, vol. 111, p. 106 643, 2020.

[47] C. S. Jawalkar, A. K. Sharma, and P. Kumar, "Experimental investigations on performance of ecdm using design of experiment approach," *i-manager's Journal on Mechanical Engineering*, vol. 1, no. 3, p. 24, 2011.

[48] T. Singh and A. Dvivedi, "On performance evaluation of textured tools during micro-channeling with ecdm," *Journal of Manufacturing Processes*, vol. 32, pp. 699–713, 2018.

[49] M. Goud, A. K. Sharma, and C. Jawalkar, "A review on material removal mechanism in electrochemical discharge machining (ecdm) and possibilities to enhance the material removal rate," *Precision Engineering*, vol. 45, pp. 1–17, 2016.

[50] C.-K. Yang and et al., "Enhancement of ecdm efficiency and accuracy by spherical tool electrode," *International Journal of Machine Tools and Manufacture*, vol. 51, no. 6, pp. 528–535, 2011.

[51] S. F. Huang and et al., "Electrochemical discharge machining micro-hole in stainless steel with tool electrode high-speed rotating," *Materials and Manufacturing Processes*, vol. 29, no. 5, pp. 634–637, 2014.

[52] C.-P. Cheng and et al., "Magnetic field-assisted electrochemical discharge machining," *Journal of Micromechanics and Microengineering*, vol. 20, no. 7, p. 075 019, 2010.

[53] S. K. Jui, A. B. Kamaraj, and M. M. Sundaram, "High aspect ratio micro-machining of glass by electrochemical discharge machining (ecdm)," *Journal of Manufacturing Processes*, vol. 15, no. 4, pp. 460–466, 2013.

[54] Z.-P. Zheng and et al., "The tool geometrical shape and pulse-off time of pulse voltage effects in a pyrex glass electrochemical discharge microdrilling process," *Journal of Micromechanics and Microengineering*, vol. 17, no. 2, p. 265, 2007.

[55] M.-S. Han, B.-K. Min, and S. J. Lee, "Modeling gas film formation in electrochemical discharge machining processes using a side-insulated electrode," *Journal of Micromechanics and Microengineering*, vol. 18, no. 4, p. 045 019, 2008.

[56] R. Wüthrich and et al., "A systematic characterization method for gravity-feed micro-hole drilling in glass with spark assisted chemical engraving (sace)," *Journal of Micromechanics and Microengineering*, vol. 16, no. 9, p. 1891, 2006.

[57] B. R. Sarkar, B. Doloi, and B. Bhattacharyya, "Parametric analysis on electrochemical discharge machining of silicon nitride ceramics," *The International Journal of Advanced Manufacturing Technology*, vol. 28, pp. 873–881, 2006.

[58] K. L. Bhondwe, V. Yadava, and G. Kathiresan, "Finite element prediction of material removal rate due to electro-chemical spark machining," *International Journal of Machine Tools and Manufacture*, vol. 46, no. 14, pp. 1699–1706, 2006.

[59] C. Wei and et al., "A finite element based model for electrochemical discharge machining in discharge regime," *The International Journal of Advanced Manufacturing Technology*, vol. 54, pp. 987–995, 2011.

[60] L. Paul and S. S. Hiremath, "Characterisation of micro channels in electrochemical discharge machining process," *Applied Mechanics and Materials*, vol. 490, pp. 238–242, 2014.

[61] H. Tokura, I. Kondoh, and M. Yoshikswa, "Ceramic material processing by electrical discharge in electrolyte," *Journal of Materials Science*, vol. 24, pp. 991–998, 1989.

[62] R. Wüthrich, U. Spaelter, and H. Bleuler, "The current signal in spark-assisted chemical engraving (sace): What does it tell us?" *Journal of Micromechanics and Microengineering*, vol. 16, no. 4, p. 779, 2006.

[63] L. Paul and S. S. Hiremath, "Characterisation of micro channels in electrochemical discharge machining process," *Applied Mechanics and Materials*, vol. 490, pp. 238–242, 2014.

[64] X. D. Cao, B. H. Kim, and C. N. Chu, "Micro-structuring of glass with features less than 100 $\mu$m by electrochemical discharge machining," *Precision Engineering*, vol. 33, no. 4, pp. 459–465, 2009.

[65] C. S. Jawalkar, "Experimental analysis on material removal modes and mechanisms in electrochemical discharge machining process for optical glass," pp. 19–36, 2022.

[66] Z.-P. Zheng and et al., "3d microstructuring of pyrex glass using the electrochemical discharge machining process," *Journal of Micromechanics and Microengineering*, vol. 17, no. 5, p. 960, 2007.

[67] D.-J. Kim and et al., "Voltage pulse frequency and duty ratio effects in an electrochemical discharge microdrilling process of pyrex glass," *International Journal of Machine Tools and Manufacture*, vol. 46, no. 10, pp. 1064–1067, 2006.

[68] Z.-P. Zheng and et al., "Improving the machining efficiency in electrochemical discharge machining (ecdm) microhole drilling by offset pulse voltage," *Journal of Micromechanics and Microengineering*, vol. 18, no. 2, p. 025 014, 2008.

[69] Z. Zhang and et al., "A study to explore the properties of electrochemical discharge effect based on pulse power supply," *The International Journal of Advanced Manufacturing Technology*, vol. 85, pp. 2107–2114, 2016.

[70] P. Boissonneau and P. Byrne, "An experimental investigation of bubble-induced free convection in a small electrochemical cell," *Journal of Applied Electrochemistry*, vol. 30, pp. 767–775, 2000.

[71] V. Fascio and et al., "Investigations of the spark assisted chemical engraving," *Electrochemistry Communications*, vol. 5, no. 3, pp. 203–207, 2003.

[72] Z. Ghorbani, "A study on gas evolving electrodes under extreme current densities," Ph.D. dissertation, Concordia University, 2012.

[73] A. Allagui and R. Wüthrich, "Gas film formation time and gas film life time during electrochemical discharge phenomenon," *Electrochimica Acta*, vol. 54, no. 23, pp. 5336–5343, 2009.

[74] N. Gautam and V. K. Jain, "Experimental investigations into ecsd process using various tool kinematics," *International Journal of Machine Tools and Manufacture*, vol. 38, no. 1-2, pp. 15–27, 1998.

[75] B. Jiang and et al., "Modeling and experimental investigation of gas film in micro-electrochemical discharge machining process," *International Journal of Machine Tools and Manufacture*, vol. 90, pp. 8–15, 2015.

[76] C.-P. Cheng and et al., "Study of gas film quality in electrochemical discharge machining," *International Journal of Machine Tools and Manufacture*, vol. 50, no. 8, pp. 689–697, 2010.

[77] D.-J. Kim and et al., "Voltage pulse frequency and duty ratio effects in an electrochemical discharge microdrilling process of pyrex glass," *International Journal of Machine Tools and Manufacture*, vol. 46, no. 10, pp. 1064–1067, 2006.

[78] H. H. Kellogg, "Anode effect in aqueous electrolysis," *Journal of the Electrochemical Society*, vol. 97, no. 4, p. 133, 1950.

[79] R. Wüthrich and et al., "Physical principles and miniaturization of spark assisted chemical engraving (sace)," *Journal of Micromechanics and Microengineering*, vol. 15, no. 10, S268, 2005.

[80] W. M. Haynes, Ed., *CRC Handbook of Chemistry and Physics*. CRC Press, 2014.

[81] J. Brauns and T. Turek, "Alkaline water electrolysis powered by renewable energy: A review," *Processes*, vol. 8, no. 2, p. 248, 2020.

[82] F. Gambou and et al., "A comprehensive survey of alkaline electrolyzer modeling: Electrical domain and specific electrolyte conductivity," *Energies*, vol. 15, no. 9, p. 3452, 2022.

[83] S. M. Seyedi Sahebari and et al., "Intelligent characterization of spark-assisted chemical engraving (sace) process using time series classification," 2023.

[84] K. R. Kolhekar and M. Sundaram, "Study of gas film characterization and its effect in electrochemical discharge machining," *Precision Engineering*, vol. 53, pp. 203–211, 2018.

[85] T. Singh, A. K. Sharma, and A. Dvivedi, "Influence of process parameters during fabrication of si microchannels using microultrasonic machining," *i-Manager's Journal on Mechanical Engineering*, vol. 3, no. 3, p. 1, 2013.

[86] S. Kumar and A. Dvivedi, "Fabrication of microchannels using rotary tool micro-usm: An experimental investigation on tool wear reduction and form accuracy improvement," *Journal of Manufacturing Processes*, vol. 32, pp. 802–815, 2018.

[87] T. Singh, A. Dvivedi, and R. K. Arya, "Fabrication of micro-slits using w-ecdm process with textured wire surface: An experimental investigation on kerf overcut reduction and straightness improvement," *Precision Engineering*, vol. 59, pp. 211–223, 2019.

[88] F. Charbonneau, "Improving the sparks assisted chemical engraving (sace) for industrial application," Ph.D. dissertation, Concordia University, 2016.

[89] J.-L. Salager, "Surfactants types and uses," *FIRP Booklet*, no. 300, 2002.

[90] J. D. Abou Ziki, T. Fatanat Didar, and R. Wüthrich, "Micro-texturing channel surfaces on glass with spark assisted chemical engraving," *International Journal of Machine Tools and Manufacture*, vol. 57, pp. 66–72, 2012.